University of Memphis

University of Memphis Digital Commons

2019

Effect of fault roughness on aftershock distribution

Khurram Aslam

EFFECT OF FAULT ROUGHNESS ON AFTERSHOCKS DISTRIBUTION AND
DAMAGE EVOLUTION IN THE NEAR-FAULT REGION

by

Khurram S. Aslam

A Dissertation

Submitted in Partial Fulfillment of the

Requirements for the Degree of

Doctor of Philosophy

Major: Earth Sciences

The University of Memphis

August 2019

Dedication

-To my beloved parents without whom I was not able to achieve all my educational career milestones.

ACKNOWLEDGEMENTS

Ahmad and Asam Farid was always encouraging. The time I spent outside CERI with Tauheed Ishrat, Junaid Ahmed, Ahmad Muzammil, Nadeem Iqbal, Zafar Iqbal, Javed Iqbal, Zahid Iqbal, Asifa Qasim, Rooh-ul-Amin, Iqtidar, and Baghwami Rathore was always refreshing.

Finally, I would like to acknowledge my family: my parents, my wife and my kids. My kids were always a source of relaxation and motivation for me during the course of my PhD. My wife was nice enough to give me free hand when I had to work at home. I would say that this dissertation could not have happened if my family was not there to support me.

PREFACE

Chapter 2 of this dissertation is based on the manuscript published in Journal of Geophysical Research. Reference of the published paper is:

Aslam, K. S., and E. G. Daub (2018), effect of fault roughness on aftershock distribution: Elastic off-fault material properties, Journal of Geophysical Research: Solid Earth, 123(11), 9689-9711.

Chapter 3 of this dissertation is based on the manuscript submitted to Journal of Geophysical Research. Reference of the submitted paper is:

Aslam, K. S., and E. G. Daub (In press, 2019), Effect of fault roughness on aftershock distribution: Plastic off-fault material properties, Journal of Geophysical Research: Solid Earth, 10.1029/2019JB017392.

Chapter 4 of this dissertation is under preparation for submission to Journal of Geophysical Research: Solid Earth.

Aslam, K. S., E. G. Daub and E. Choi (In preparation, 2019), Modeling damage evolution in the near-fault region as a result of rupture on complex fault, Journal of Geophysical Research: Solid Earth.

Chapter 5 of this dissertation is under preparation for submission to Journal of Geophysical Research: Solid Earth.

Aslam, K. S., E. G. Daub and Ricardo Taborda (In preparation, 2019), Examining stress and ground motion patterns in numerical simulations of earthquake slip.

ABSTRACT

A large earthquake triggers earthquakes on many nearby faults. Most of the triggered earthquakes (i.e. aftershocks) can be explained by the static stress increase in the region where they occur. Some aftershocks also occur in the regions of static stress decrease or stress shadows. The current physical models of aftershock occurrence are not able to explain aftershocks that are observed in stress shadows. The static stress changes, following an earthquake are calculated using slip that occurs on the main fault. The source inversions, which calculate these slips, are not able to resolve finer scale details of slip due to their coarser spatial resolution. The finer scale details of slip influence finer static stress changes, which plays an important role in the production of smaller aftershocks. These finer details of stresses may be able to better explain the occurrence of aftershocks in stress shadows.

In this study, we perform dynamic earthquake rupture simulations of large earthquakes. This modeling resolves the finer scale details of slip based on elasticity and friction and hence has the ability to predict the spatial distribution of slip and stress changes. We perform numerous two dimensional (2D) earthquake rupture simulations on rough strike slip faults assuming elastic and plastic off-fault material properties. We consider many different realizations of a self-affine rough fault profile. We output the static stress changes in the off-fault medium from our simulations and use these to calculate the Coulomb failure function (CFF) in the region surrounding the fault. We use similar and variable orientations for receiver faults planes to calculate CFF values. The similar receiver fault plane orientations are chosen to be parallel to overall trace of the main fault, while the variable receiver fault orientations are determined using the angle at which plastic shear strain is maximum.

Our results show that the stresses are highly complex in the region close to the fault. This complexity reduces as the distance from the fault increases. We conclude that the stress complexity observed in the near-fault region is due to roughness of the fault

profile. The complexity of stresses in the near-fault region causes the CFF to be highly heterogeneous in the near-fault region. We observe many positive CFF zones within negative CFF zones in the near-fault region. We believe that these are the potential locations of aftershocks observed in stress shadows. The areas where they appear would be seen as stress shadows in typical static stress change calculations due to insufficient resolution of the fault slip. Furthermore, we observe that the overall trend of the CFF with distance remains similar either assuming elastic or plastic off-fault material properties. In the near-fault region, we observe many more positive CFF zones when we calculate CFF values using variable receiver fault orientations. Our results suggest that the spatial aftershock distribution surrounding a fault is controlled by both stress heterogeneity as well as the co-seismic damage zone complexity. Comparing our model rupture areas of positive CFF zones with rupture areas of aftershocks and preshocks from relocated earthquake catalogs of Northern and Southern California, we conclude that the stresses in the near-fault region are dominated by the fault roughness effects throughout the seismic cycle.

We model the inter-seismic period of a complex rupture by running a quasi-static model (LTM) initialized with stresses from dynamic earthquake rupture model. Our results show that the geometrical bends of the fault profile causes the plastic deformation to be localized in the co-seismic phase, which acts as a seed for the development of new shear features in the inter-seismic phase.

We perform 3D deterministic earthquake ground motion simulations for the northern Canterbury plains, Christchurch and the Banks Peninsula region of New Zealand, which explicitly incorporate the effects of the surface topography. Our comparison of the ground motions between the topographic model and the flat model shows differences in ground motions for stations placed at higher elevations. These higher elevation stations have higher peak accelerations and longer duration of the signals when topography is considered, suggesting that the topography leads to stronger ground motions and additional resonance of seismic waves.

TABLE OF CONTENTS

Contents	Pages

LIST OF TABLES

Tables   **Pages**

LIST OF FIGURES

Chapter 1

Introduction

Earthquakes produce other earthquakes through aftershock sequences. Most of these aftershocks occur in the traditional aftershock zone. The traditional aftershock zone occupies an area of 1-2 fault lengths surrounding the mainshock's (or main) fault. The stress on the main fault drops during the mainshock, which changes the stresses on many nearby (receiver) faults. The stress changes on some of these faults result in aftershock triggering. The aftershocks pose significant hazards to humans due to their tendency to produce strong ground motions and tsunamis, e.g. the 2010-2011 earthquake sequence of Canterbury region killed 115 people, and damaged 150,000 homes (Potter et al., 2015). Similarly, an aftershock of 1999 Izmit earthquake (7.4 magnitude) in Turkey killed 7 and injured 420 people (Wiemer, 2000). Although aftershocks are hazardous, scientists currently lack a complete understanding of aftershock triggering mechanisms. A better understanding of aftershock triggering may help reduce seismic hazard and risk associated with aftershocks in seismically active regions.

A decrease in the clamping stress or an increase in the shear stress on a receiver fault brings it closer to failure. An area near a main fault where the clamping stress decreases and/or the shear stress increases on the receiver faults is called zone of static stress increase while an area where the clamping stress increases and/or the shear stress decreases on receiver faults is called a zone of static stress decrease (or stress shadow) (Freed, 2005). The occurrence of aftershocks in the traditional aftershock zone is broadly explained by the mechanism of static stress change. Although this mechanism has explained a number of features of aftershocks, there are few aspects of aftershock distributions which do not agree with the prediction of the model based on static stress change (Segou & Parsons, 2014). The occurrence of aftershocks in the stress shadow is one of those aspects of aftershocks which is not fully understood. We conduct our study to investigate the occurrence of

aftershocks in the stress shadows. Additionally, we aim to better understand the spatial distribution of aftershock occurrence following a large earthquake with this study.

The static stress changes are calculated using slips that occur on the main fault. These slips are estimated from source inversion studies. The spatial resolution of these inversions are usually fairly coarse, and they are unable to resolve the fine scale details of slip and hence finer details of stress changes. These details are necessary to explain the spatial distribution of aftershocks, and may be necessary to understand the occurrence of aftershocks in stress shadows. In our study, we use numerical modeling to better understand the spatial distribution of aftershocks. We perform numerous dynamic earthquake rupture simulations of an earthquake on strike slip faults. These simulations calculate the fault slip by combining elastic wave propagation with fault constitutive laws to generate a spontaneous physics-based model of faulting (Harris et al., 2018). This modeling thus resolves the finer scale details of slip based on elasticity and friction and hence has the ability to predict the spatial distribution of slip and stress changes, features that are not resolved by stress changes estimated using observational data. These simulations have been widely used to infer information related to physical processes occurring during rupture propagation (Bizzarri & Cocco, 2005; Aochi et al., 2000). We aim to improve our ability to understand the spatial distribution of aftershocks using dynamic rupture simulations. Doing this will allow us to better constrain models of seismic hazard and risk, as well as improve our overall understanding of the physics governing earthquake occurrence.

We perform our dynamic earthquake rupture simulations on geometrically heterogeneous (i.e. rough) strike slip faults. The geometrical heterogeneity of a fault is important to consider during rupture process since it can significantly affect the earthquake rupture process. Some studies (Chester & Chester, 2000; Dieterich & Smith, 2009) have shown that these geometrical heterogeneities can introduce stress heterogeneities having amplitudes equivalent to the prevailing stresses when the fault slips. We carry out a suite

of two dimensional (2D) simulations of earthquakes on strike slip faults exhibiting complex geometry to fully quantify the stress change resulting from dynamic slip on the fault and present our results in chapter 2. The off-fault material property is considered elastic during these simulations. Since real faults are represented by self-affine fractals (Candela et al., 2012), we consider a range of fault roughness parameters representing major faults and run simulations with numerous realizations of each set of fault roughness parameter values. We calculate the Coulomb failure function (CFF) for each of these realizations using parallel receiver fault orientations and quantify the CFF by computing its probability density function (PDF). We compare our model predictions with observations of aftershock distributions in space using relocated earthquake catalogs of Northern and Southern California (Shearer et al., 2005; Waldhauser & Schaff, 2008). Since the main emphasis of this work is to observe how the heterogeneous stress distribution associated with the fault roughness can be related to the aftershock distribution, we analyze the seismicity both before and after major earthquakes. Doing this helps us distinguish the effects of heterogeneous stress distribution caused by fault roughness on stresses present in the off-fault region during the pre-seismic phase and new stresses imposed in the same region during the post-seismic phase.

In the third chapter, we carry out a suite of 2D simulations of earthquakes on strike slip faults exhibiting complex geometry but describe the off-fault material using plasticity instead of elasticity. Considering plasticity to represent the off-fault material is critical for extreme stress conditions, since results presented in chapter 2 (i.e. simulations performed using elastic properties) may not be relevant when extreme stress conditions are encountered that cause the material to deform inelastically (Noda et al., 2009). An advantage of using plastic properties for off-fault material is to approximate the receiver fault orientations in the off-fault region by calculating the angle at which the plastic shear strain is maximum. These orientations can then be used to calculate the CFF values in the off-fault region. Hainzl et al. (2010) showed that incorporating realistic multiple receiver

fault orientations changes the spatial pattern of predicted aftershocks, and the new pattern shows better agreement with observed data (i.e. aftershocks of the 1992 M_w 7.3 Landers earthquake). Furthermore another advantage of using plastic off-fault properties is that the extent of plastic deformation in the off-fault region gives us a proxy of damage observed in fault zones during earthquake rupture. This damage zone extent can then be used to investigate how the damage zone controls the off-fault seismic activity. To run our simulations for chapter 3, we consider self-similar fault fractal profiles (Hurst exponent $= 1$), with fault roughness amplitude values of 0.01. These fault roughness values are taken from major strike slip fault observational studies (Candela et al., 2012). Similar to chapter 2, we run our simulations for numerous realizations of the fault profile and then calculate the amplitudes of the CFF for each of these realizations. We calculate the probability density function (PDF) of the CFF from all fault realizations in order to quantify and compare it with the aftershock distributions in space using observational data. We use relocated earthquake catalogs from Northern and Southern California (Shearer et al., 2005; Waldhauser & Schaff, 2008) for the comparison of our model results with naturally occurring seismicity.

In fourth chapter, we investigate how the heterogeneous stresses resulting from rupture simulations on a rough fault, influence the tectonic loading and damage process in the near-fault region over the inter-seismic time period. We do this by coupling our dynamic rupture code (that models the co-seismic phase) with a long term tectonic modeling code (that models the inter-seismic phase), and running a complete simulation of the inter-seismic loading phase. To explain the coupling in detail, we first carry out a few dynamic rupture simulations on rough strike-slip faults in 2D, where the off-fault material properties are described using plasticity. Similar to rupture simulations of chapter 3, we use self-similar fault fractal profiles with fault roughness amplitude values of 0.01. Due to the varying fault roughness, ruptures exhibit a wide range of slip characteristics, including sub-shear rupture speeds, super-shear rupture speeds, and ruptures that arrest prior to

4

propagating along the entire fault. We save the stress and plastic strain fields at the end of these simulations and use these fields to initialize simulations of the inter-seismic phase. The long-term tectonic modeling (LTM) code subjects the fault to slow, quasi-static tectonic loading. The off-fault deformation in the LTM is based on continuum plasticity, so that additional plastic deformation can occur due to the stressing imparted by tectonic loading. This setup allows us to capture the damage process over time (during the inter-seismic phase) for many different ruptures that had different slip characteristics.

Our dynamic earthquake rupture simulations using plasticity (chapter 3) show that earth structure can plan an important role in understanding the dynamics of faulting, and this also applies to ground motions. This study provides an example of how topography, combined with complex velocity structures, might influence ground motions from an earthquake. In chapter 5, we present our results from 3D kinematic rupture modeling of an earthquake that occurred in the Christchurch area, New Zealand. The kinematic rupture models are more focused on ground motions since they use prescribed evolution of fault slip. The earthquake we modeled is a part of 2010-2011 Christchurch earthquake sequence of New Zealand with a magnitude of Mw 5.4. The simulations are performed in an area of 120 km x 120 km, with the model reaching a depth of about 60 km. Our simulation parameters are set to minimum shear wave velocity of 500 m/sec, and a maximum frequency of 2.0 Hz. We incorporated the 3D velocity structure as well as the topography of the region into our kinematic modeling. Our main objective of the study is to observe how the 3D topography and velocity structure of the region affect the surface ground motions, which in turn change the seismic hazard of the region.

Chapter 2

Effect of fault roughness on aftershock distribution: Elastic off-fault material properties

Aslam, K. S., and E. G. Daub (2018), Effect of fault roughness on aftershock distribution: Elastic off-fault material properties, Journal of Geophysical Research: Solid Earth, 123(11), 9689-9711.

Abstract

We perform physics-based simulations of earthquake rupture propagation on geometrically complex strike-slip faults to examine the off-fault stress changes resulting from dynamic fault slip. We consider many different realizations of the fault profile and use the output of our simulations to calculate the Coulomb failure function (CFF) for each realization. We analyze the effects of fault maturity as well as the self-affine character of the fault surface on the stress field. To quantify our results, we calculate the probability density function (PDF) for the CFF as a function of distance and observe that the CFF values show a greater variability in the near-fault region (distance < 3 km away from fault) and this spread squeezes into a narrow negative range in the far-field region. In the near-fault region, we see many zones of positive CFF change which are not observed in the far-fault region. We consider these zones of CFF increase as locations of potential aftershocks and compare their size with rupture areas of aftershocks from relocated earthquake catalogs of Northern and Southern California. Our model results and observational data show a relatively high probability of occurrence of smaller potential aftershock areas compared to larger ones in the near-fault region. Additionally, based on our comparison with aftershock and preshock data, we conclude that the stresses in the near-fault region are dominated by fault roughness effects. Our results suggest that tectonic stresses are highly spatially heterogeneous, and this complexity persists throughout seismic cycle.

7

Introduction

The triggering mechanism of aftershocks is an aspect of earthquake occurrence which is not fully understood. Many authors have proposed different effects such as static stress changes (King et al., 1994), passing seismic wave induced dynamic stresses (Hill et al., 1993; Gomberg et al., 2003), afterslip (Perfettini & Avouac, 2004), fluid flow (Nur & Booker, 1972), static stress triggering of rate-and-state nucleation sites (Dieterich, 1994), and the evolution of viscoelastic damage rheology (Ben-Zion & Lyakhovsky, 2006). All of these effects are believed to play a role in aftershock triggering, but the exact contribution of each mechanism is not known. Another factor complicating the identification of causative effect of aftershock triggering is the delay in time of the aftershock events relative to the main shock. Because of these observational challenges, it is not always possible to identify the specific physics at work. While static stress changes explain many features of aftershocks, one shortcoming of this model is that it cannot explain aftershock occurrence in stress shadows. As an example, the $M_w = 6.9$ 1989 Loma Prieta Earthquake has many aftershocks occurring in regions of stress increase but there are additional aftershocks which occurred in the regions of stress shadows (Segou & Parsons, 2014). Furthermore, focal mechanisms following the Loma Prieta event are diverse, and are not aligned with the directions expected for static stress triggering (Kilb et al., 1997; Beroza & Zoback, 1993).

In order to better understand aftershock triggering by static stresses, we perform earthquake rupture simulations on rough faults and use physical models of slip and stress to estimate the expected aftershock locations following a large earthquake. Dynamic rupture simulations calculate fault slip by combining elastic wave propagation with fault constitutive laws to generate a spontaneous physics-based model of faulting. This modeling resolves the finer scale details of slip based on elasticity and friction and hence has the ability to predict the spatial distribution of slip and stress changes, features that are not resolved by stress changes estimated using observational data (Freed, 2005). Dynamic rupture simulations have been widely used to infer information related to physical

processes occurring during rupture propagation (Bizzarri & Cocco, 2005; Aochi et al., 2000; Harris, 2004; Dunham & Archuleta, 2005; Dalguer et al., 2003; Shi & Ben-Zion, 2006; Harris & Day, 1997; Tinti, Bizzarri & Cocco, 2005; Shi & Day, 2013; Daub & Carlson, 2008; Daub et al., 2010).

Real faults exhibit complex geometries and these geometrical complexities introduce heterogeneities in the stress distribution when the fault slips (Candela et al., 2012; Brown & Scholz, 1985; Power et al., 1987; Power & Tullis, 1995; Renard et al., 2006). Studies have shown that during fault slip, non-planar fault geometry can introduce normal and shear stress perturbations that are in many cases comparable to the prevailing stresses (Chester & Chester, 2000; Dieterich & Smith, 2009). Many simulation studies (dynamic rupture propagation as well as earthquake ground motions) have been performed considering faults as rough surfaces to examine how rupture propagates on rough faults in comparison to flat faults and how the surface ground motions at high or low frequency vary as a result of earthquake nucleation and propagation on complex faults. Dieterich & Smith (2009) studied the interactions among slip and off-fault stressing during slip on rough faults by assuming quasi-static slip on the fault with a constant frictional coefficient. They observed that linear scaling of fault slip with fault length is no longer observed for faults showing realistic roughness values observed for natural faults. A study by Dunham et al. (2011c) showed that dynamic ruptures on rough faults produce accelerograms exhibiting similar characteristics at high frequencies to those observed in strong motion records from real earthquakes. Fang & Dunham (2013) studied the effect of fault roughness to observe the influence of supplementary tractions introduced on the fault due to its roughness. They related differences in the observed background stress level required to generate moderate to large earthquakes for mature and immature faults to an effective aditional shear resistance termed "roughness drag" due solely to fault roughness. Bruhat et al. (2016) also explored the behavior of rupture propagation on rough faults and observed that supershear rupture transitions are more likely to be seen on rougher faults as compared to flat faults. Based on

9

investigation of some special cases, they related those that favored transition to rupture propagation into a segment which is unfavorably oriented, or to rupture deceleration due to an unfavorable bend. They further observed that sustained propagation of these supershear ruptures occur mostly on fault sections which are smoother than average. Shi & Day (2013) performed dynamic rupture and ground motion simulations in three dimensions (3D) on rough faults and observed that local stress perturbations due to non-planarity cause incoherence in the rupture process, and found that the ground-motion intensities estimated from their simulations are statistically similar to those of Ground Motion Prediction Equations.

In this study, we build upon these previous studies and carry out a suite of two dimensional (2D) simulations of earthquakes on strike slip faults exhibiting complex geometry to fully quantify the stress change resulting from dynamic slip on the fault. Since real faults are represented by self affine fractals (Candela et al., 2012), we consider a range of fault roughness parameters representing major faults and run simulations with numerous realizations of each set of fault roughness parameter values. We calculate the Coulomb failure function (CFF) for each of these realizations and quantify the CFF by computing its probability density function (PDF). We compare our model predictions with observations of aftershock distributions in space using relocated earthquake catalogs of Northern and Southern California (Shearer et al., 2005; Waldhauser & Schaff, 2008). Since the main emphasis of this work is to observe how the heterogeneous stress distribution associated with the fault roughness can be related to the aftershock distribution, we analyze the seismicity both before and after major earthquakes. Doing this helps us distinguish the effects of heterogeneous stress distribution caused by fault roughness on stresses present in the off-fault region during the pre-seimsic phase and new stresses imposed in the same region during the post-seismic phase.

Model Setup

Fault roughness

A fault appears as linear feature on the surface of earth with wavy irregularities (Candela et al., 2012; Brown & Scholz, 1985). These irregularities are observed at all scales that have been measured (Brown & Scholz, 1985; Power et al., 1987; Power & Tullis, 1995; Renard et al., 2006). A newly fractured rock shows a fractal profile, and then subsequent slip decreases the amplitude of the roughness while still maintaining its fractal characteristics (Sagy et al., 2007). Figure 1(a) shows the roughness of a fault profile in the direction parallel to the slip of the fault. Self-similar and self-affine fractal fault profiles are commonly used to describe observed fault roughness.

Self-similar profiles are curves that show identical characteristics regardless of the scale of view (i.e. zooming in or out is equivalent to rescaling the length and height by the same factor), while self-affine fractals require re-scaling the length and height by different factors to obtain similar statistical profiles (Russ, 1994). Self-similar is thus a specific case of self-affine where the root-mean-square (RMS) height fluctuation of the profile is proportional to the length of the profile. Earlier studies (Brown & Scholz, 1985; Power & Tullis, 1995; Lee & Bruhn, 1996) suggest that natural fault surfaces are self-similar fractals. More recent studies (Sagy et al., 2007; Renard et al., 2006; Brodsky et al., 2011; Candela et al., 2012, 2009, 2011) are able to provide very high resolution fault roughness measurements. Some of these measurements suggest that fault surfaces in both the slip-parallel and slip-perpendicular direction are self-affine fractals, though other authors suggest that self-similar profiles provide a better overall description of the fault geometry (Shi & Day, 2013).

We use two parameters to describe fault roughness. The first parameter is the Hurst exponent, denoted by H, which quantifies the self-affine scaling of the fault profile. For a self-affine fractal, if we rescale the horizontal scale by a factor x, then the vertical scale is rescaled by factor x^H (for the self-similarity case $H = 1$). The second parameter specifies
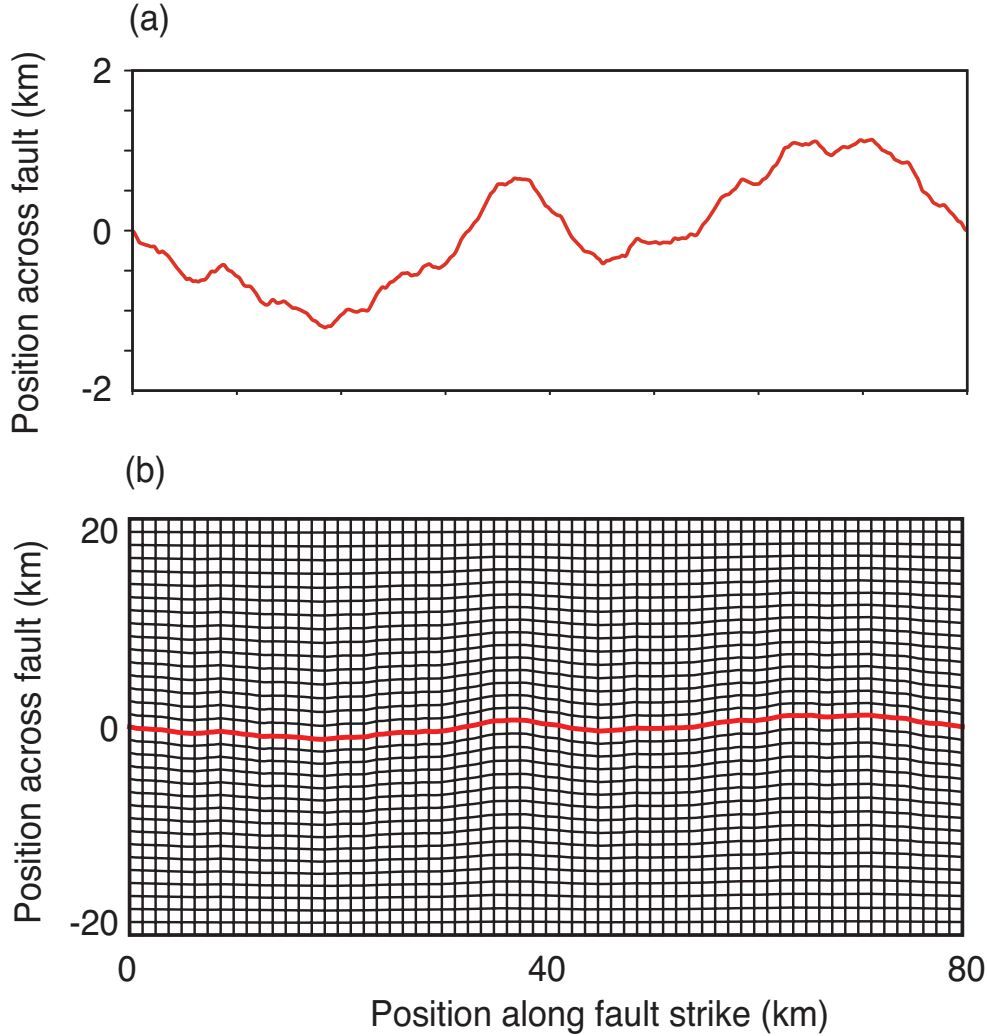
Fig. 1: Modeling setup of our simulations of slip on a rough strike-slip fault. (a) Fault roughness profile is shown with RMS height to wavelength ratio of 0.01 and Hurst exponent of 1.0. The minimum wavelength of the profile is 500 m. The fault profile is vertically exaggerated. (b) Domain setup of the fault trace shown in (a), shown to scale. The fault profile is shown in the red color. The grid is constructed using transfinite interpolation. We perform 100 simulations of each combination of roughness parameter but in each case the domain dimensions remain the same, 80 km long and 40 km wide. In each simulation, the fault profile is different which in turn changes the grid to be used for solving the rupture propagation problem using finite differences.

the actual height of fault curve relative to a planar fault. One such parameter that quantifies the amplitude is the RMS deviation of a fault profile from planarity. The RMS height (h_{rms}) for a 1D self-affine fault profile ($y = f(x)$) with length L can be defined as

$$h_{rms} = \sqrt{\frac{1}{L} \int_{-L/2}^{L/2} f^2(x) dx}. \tag{2.1}$$

Equation 2.1 considers all the wavelengths of roughness that are smaller than L. The RMS height is related to the maturity of the fault as the roughness amplitude of the fault varies when the fault progresses from immature to mature. The value of H varies from 0.6 to 1 for observed fault surfaces while the RMS height to wavelength ratio has values between 10^{-2} to 10^{-3} depending upon the maturity of the fault (Brodsky et al., 2011). A smaller value of H indicates that the faults appears rougher when viewed at decreasing scales and a smaller value of RMS height indicates a smoother fault profile. It is also important to note that the RMS height is the same at all scales for self-similar fractals, but it is scale dependent for self-affine fractals (Brown & Scholz, 1985; Aviles et al., 1987; Okubo & Aki, 1987; Power et al., 1988). In this study, we use the RMS height at the largest scale to quantify roughness for self-affine profiles. The Hurst exponent is related to power spectral density for self-affine fractals:

$$p(k) \propto k^{-1-2H}. \tag{2.2}$$

Here $p(k)$ is the spectral density, k is the wave number given by $k = \frac{2\pi}{\lambda}$. In the case of a self-similar profile,

$$p(k) = ck^{-3}. \tag{2.3}$$

Here c is given by $2\pi^3\gamma^2$. The parameter γ is the RMS height to wavelength ratio. Figure S1 shows spectral density plot for one dimensional (1D), self-similar fault and self-affine fault profiles.

We simulate earthquake rupture propagation on self-affine faults with 100 different

realizations of the fault profile for each choice of H and RMS height. For each realization of fault roughness, the parameters are taken from observational values of real faults i.e. H ranging from 0.6 - 1 and RMS height to wavelength ratio of 10^{-2} and 10^{-3}. A Fourier method is used to generate the fault surface with the desired spectrum and random phase (Andrews & Barall, 2011) with zero mean. Due to the finite numerical resolution of our simulations, we cut off the fractal at a minimum wavelength corresponding to 20 times the grid spacing to ensure that our modeling is well resolved.

Dynamic rupture model

We consider a 2D plane strain model for simulation of dynamic rupture propagation as seen in Fig. 1 (b). The domain is 80 km long and 40 km wide. The fault surface is given by the curve $f(x)$ which deviates from $y = 0$ based on the values of Hurst exponent and RMS height to wavelength ratio. For each combination of fault roughness parameters, we run simulations of rupture propagation for 100 different realizations of the fault surface. We run all our simulations with a grid spacing $\Delta x = 25$ m. We have also run a few additional simulations with a smaller grid spacing ($\Delta x = 10$ and 5 m) to confirm that our simulations are well resolved at $\Delta x = 25$ m. The selected Δx gives a resolvable (minimum) fault roughness wavelength $\lambda_{min} = 20\Delta x = 500$ m $= 0.5$ km for all of our simulations. We use rupture dynamics code `fdfault`, which solves the elastodynamic wave equation using finite differences and has been verified against multiple benchmark problems of the SCEC/USGS rupture code verification group (Harris et al., 2009, 2018). We run our simulations to 4th order accuracy in both space and time. Fault and external boundary conditions are imposed weakly (Kozdon et al., 2012), resulting in a method that is globally 4th order accurate (Kozdon et al., 2013). The code handles the irregular geometry of the fault surface through algebraic coordinate transformations on a structured grid (Liseikin, 2009).

We assume a uniform initial background stress field (negative in compression) in all of our simulations. Because of the varied fault profile, the uniform stress tensor leads to heterogeneous initial shear and normal tractions along the fault. Figure 2 shows the
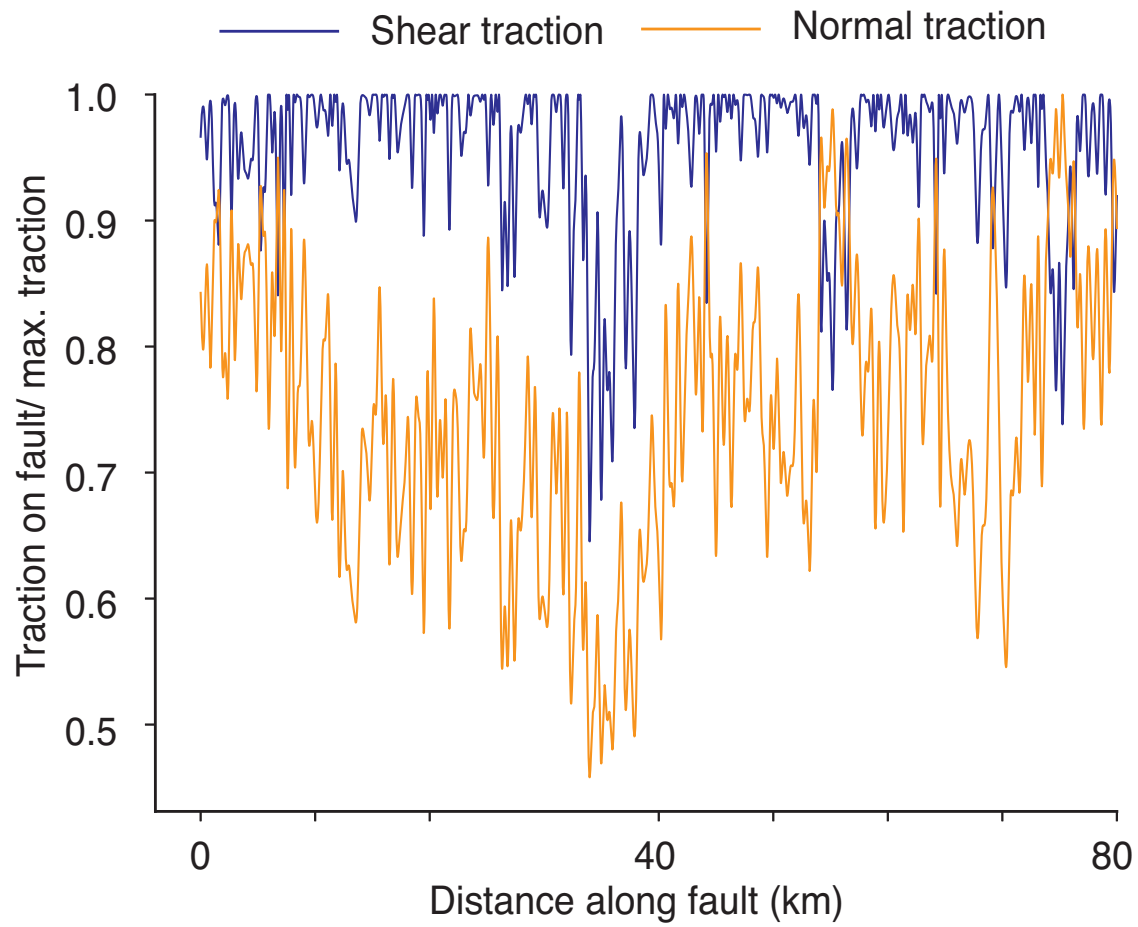
Fig. 2: Normal and shear tractions resolved on the fault plane. The fault roughness causes the tractions to be highly heterogeneous along the fault even if the regional stresses are uniform across the whole domain.

normalized values of shear and normal traction resolved on each point on the fault plane from the uniform regional stress tensor. As can be seen in Fig. 2, the traction values are highly heterogeneous, with values as low as half of the maximum value of traction. Depending on the realization of the fault surface, some ruptures may arrest at a geometrically unfavorable bend and die out early, so to avoid this, we choose initial background stress field values (given in table 1) that ensure at least 90% of ruptures propagate 50 km from the nucleation point before dying out.

We model the friction on the fault using the linear slip weakening (SW) friction law (Ida, 1972; Andrews, 1976, 1985; Day, 1982). This friction law has been widely adopted in dynamic rupture simulations (Harris et al., 2009) and is conceptually simpler in implementation (Bizzarri, 2010) when compared to other friction laws such as rate and state friction (Dieterich, 1979; Ruina, 1983) or the Shear Transformation Zone friction law (Daub & Carlson, 2010). For the SW law, the friction on the fault μ is a function of the slip U on the fault. The initial friction on the fault μ_s drops to a dynamic friction value μ_d over a critical slip distance D_c as a function of slip:

$$\mu(U) = \begin{cases} (\mu_s - \mu_d)(1 - \frac{D}{D_c}) + \mu_d & \text{for } U < D_c \\ \mu_d & \text{for } U \geq D_c. \end{cases} \tag{2.4}$$

Figure 3 illustrates the slip-dependent friction coefficient, where the friction linearly drops from static friction to dynamic friction over a critical distance given by D_c. We choose $D_c = 0.4$ m, $\mu_s = 0.7$ and $\mu_d = 0.2$ in all of our simulations. The low dynamic friction is chosen based on lab experiments that show strong dynamic weakening at co-seismic slip speeds (Goldsby & Tullis, 2011, 2002; Hirose & Bystricky, 2007; Di Toro et al., 2011, 2004; Hirose & Shimamoto, 2005; Tsutsumi & Shimamoto, 1997; Beeler et al., 2008). A complete list of parameter values used in this study is given in Table 1.

It is important to note that the friction on the fault is also spatially variable due to the heterogeneous distribution of slip, and each point on the fault fails individually based
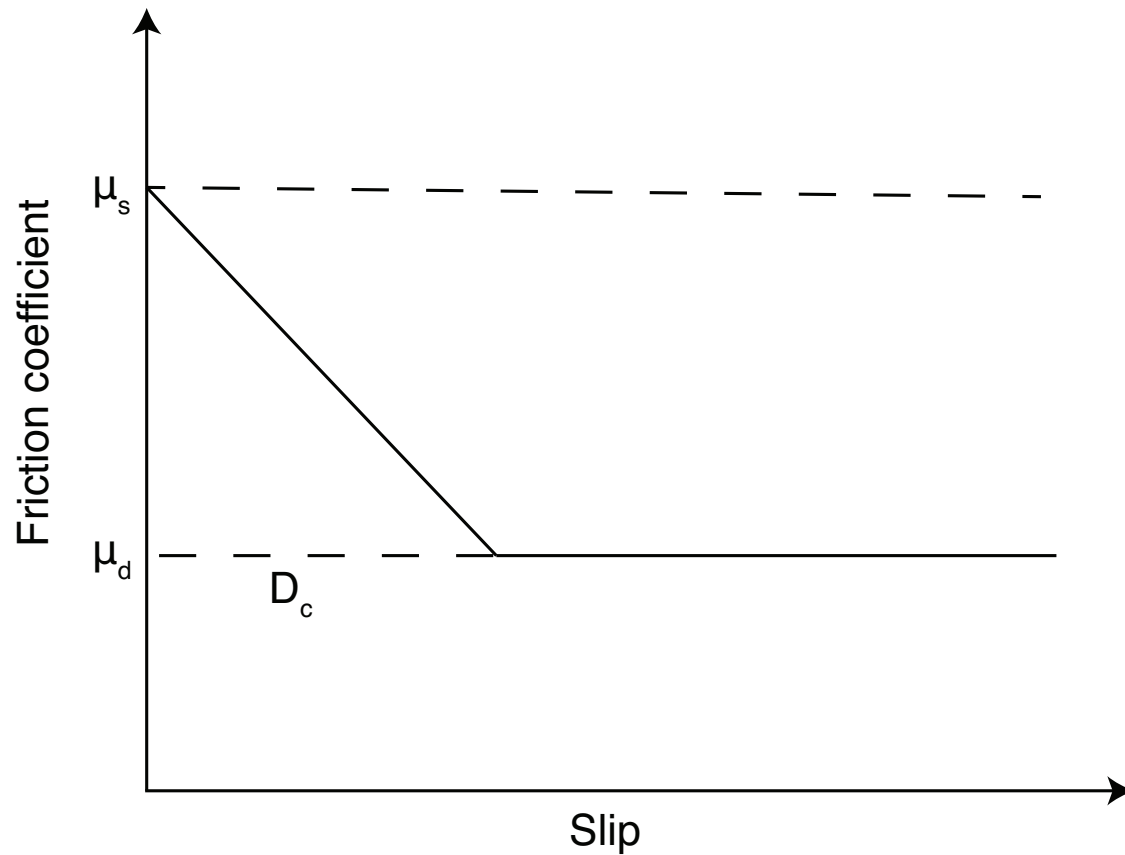
Fig. 3: Friction on the fault is governed by the linear slip weakening law. No slip occurs until the ratio of shear to normal stress reaches the static friction μ_s. Once slip initiates, the friction decreases linearly with slip to the dynamic coefficient μ_d over a critical slip distance D_c.

on the stress changes from wave propagation and fault slip. In some of our simulations, we also encounter tensile normal traction at some points on the fault during fault slip. We do not allow fault opening in these simulations, and set the fault to have zero shear strength when tensile normal tractions occur.

In all of our simulations, we start rupture near the center of the fault. We also vary our rupture nucleation strategy for a single realization of each fault profile to ensure that our results do not depend on the nucleation method. After examining the results from each nucleation method, we default to the simplest strategy of a statically overstressed nucleation patch for our full set of simulations. We nucleate ruptures in the areas where the ratio of shear to normal stress is highest after filtering out the high frequency variations associated with the small scale roughness (Fang & Dunham, 2013). We expect such locations to be representative of the regions on natural faults where ruptures are likely to initiate. In all of our simulations, we start rupture near the center of the fault. We do this by generating many fault profiles and then calculating the ratio of shear to normal stress at each point on the fault. If the ratio is highest between 35 to 45 km along fault distance, then we consider the fault profile for further rupture simulation, otherwise we discard the profile and generate a new one.

The SW friction law has been used with a variety of different nucleation strategies to initiate ruptures (Day, 1982; Bizzarri & Cocco, 2005; Dunham & Archuleta, 2005; Ionescu & Campillo, 1999; Andrews, 1985). These different nucleation strategies could potentially affect the rupture propagation process and therefore the final stress field. Studies such as Bizzarri (2010) have quantified this effect by comparing the process of rupture propagation and resultant surface ground motions for ruptures with different nucleation strategies. We vary our rupture nucleation strategy for a single realization of each fault profile to ensure that our results do not depend on the nucleation method. We use three different techniques to initiate rupture, 1) time independent over-stressing of the fault (a method used in early SCEC rupture code problems (Harris et al., 2009)), 2)

18

time-dependent over-stressing of the fault, and 3) over-stressing a single grid point within a critically stressed nucleation patch (a method similar to (Schmedes et al., 2010)). In the first technique, we select a 3 km fault patch and raise the shear traction on each point of the fault patch to $1.01T_f^{(i)}$. Here $T_f^{(i)}$ is the failure traction on ith point on the fault, and is given by $\mu_s T_n^{(i)}$, where $T_n^{(i)}$ is the normal traction on ith point on the fault. In the second technique, we again select a 3 km fault patch and linearly raise the shear traction with time on each point within it to $1.01T_f^{(i)}$ over an onset time of 0.87 sec. In the last technique, we select a 3 km fault patch and raise the shear traction on each point of this patch just below the failure traction $(0.999T_f^{(i)})$ while the shear traction on the central grid point of the fault patch is raised to a traction value of $1.01T_f^{(i)}$.

Once we run simulations with each of these nucleation strategies, we compare the ground motions resulting from these strategies at six synthetic station locations on each side of the fault. Three of these station locations reside in the near-fault region while three reside in far-fault region. In our modeling setup, the region having distance < 3 km from fault can be considered as the near-fault region while region having distance > 5 km as the far-fault region. Our reason for considering these regions separately is due to the differences we find in the static stress changes, as discussed in the results section. We compare two properties of the seismic signal: the amplitude of the first arriving compressional (P) wave, and the peak ground velocity (PGV) of the signal at those stations. In addition, we also compare the final slip distribution from ruptures initiated using the nucleation strategies mentioned above. Based on our comparison at the selected grid resolution ($\Delta x = 25$ m), we find the amplitude of the P wave as well as the PGV value to be in a similar range for all of our nucleation strategies at each station. The average difference between the amplitude of the P wave and the PGV is less than 10% for both near-fault and far-fault regions. We also do not find any significant difference in the slip history to prefer any particular strategy. Therefore, we default to the simplest strategy of a statically overstressed nucleation patch for our full set of simulations.

CFF and synthetic aftershock calculations

The Coulomb failure function (King et al., 1994) can be calculated using the following equation

$$\Delta CFF = \Delta\tau_\beta - \mu_\beta \Delta\sigma_\beta. \tag{2.5}$$

Here ΔCFF is the change in Coulomb failure function on a receiver fault due to static stress changes introduced by the earthquake on the main fault, $\Delta\tau_\beta$ is the shear stress change introduced on the same receiver fault plane, μ_β is the effective friction coefficient of the receiver fault (a combination of the friction coefficient and Skempton's coefficient (Skempton, 1954) describing poroelastic effects), and $\Delta\sigma_\beta$ is the change introduced in normal stress on the receiver fault plane. It is important to note that τ_β and σ_β are determined by resolving the stress tensor onto the desired receiver fault plane surrounding the main fault.

We choose the orientation of all the receiver faults to be parallel to the overall trace of the main fault. This assumption will not necessarily be true for every case, but we believe that it is reasonable to assume that aftershocks occur on structures formed due to the same tectonic history as the main fault. Additionally, field studies also reveal parallel faults in strike-slip fault zones such as those observed for the Carboneras fault zone in Spain (Faulkner et al., 2003). All of our calculations assume $\mu_\beta = 0.4$, a value close to the average of the friction values (average of μ_s and μ_d) on the main fault. This value is typically used in the literature for strike-slip or unknown faults (Parsons et al., 1999), and receiver fault orientations parallel to the trace of the main fault. If the calculated values of CFF are positive, it indicates increased likelihood of failure, while decreased values are expected to indicate stress shadows or regions with reduced seismic activity. We combine the calculated CFF values from all realizations of each set of fractal characteristics to compute point statistics.

Our dynamic rupture simulations calculate the change in stresses throughout the

history of the dynamic rupture and thus we directly obtain the full stress tensor after the earthquake from our simulation output. Using the stress tensor we calculate the Coulomb failure function (CFF) using Equ. 2.5 . For all of our CFF calculations, We choose the orientations of receiver faults to be parallel to the overall trace of the main fault. As we are interested in calculating the static stress changes from our simulation results, we do not want the final stresses to include the effects of dynamic wave propagation. To ensure this, we choose a smaller portion of the domain (40 km along the fault and 30 km across the fault) and extract the stress tensor in all of our calculations after the dynamic waves have had sufficient time to propagate away from the central portion of the domain. Since our selected shear wave velocity is 3.464 km/sec, we allow 18.4 sec to give the waves sufficient time to propagate across the entire domain, and away from the central region. To ensure that the point statistics of CFF in the portion of the domain used for analysis are not affected by boundary effects, we run a few additional simulations with a larger domain size. We find that the results presented here are independent of the computational domain size.

In addition to point statistics of the CFF, we also analyze its spatial correlations. In particular, we are interested in the spatial dimension of these correlations. Using the CFF calculations for all 100 realizations of fault profile, we count the zones of positive CFF surrounding the main fault and quantify their size and distance from the fault. Based on the minimum roughness wavelength of the fault profiles, we only consider those positive CFF zones that are at least 500 m long. Our goal is to determine if potential aftershock zones follow any particular spatial trend as a function of distance from the fault. We also compare the spatial correlations in our modeling results with real aftershock observations to make quantitative comparisons. This comparison can further help us examine if there is any relationship between aftershock size, location, and fault roughness. To describe the process of calculating positive CFF zone area in detail, we first select a region of positive CFF at a random distance away from the main fault and calculate its length following the strike of the main fault. This length is then converted into rupture area by supposing that

the positive CFF zone hosts a circular patch rupture at that distance. The idea that small to moderate magnitude earthquake ruptures have a circular dimension is supported by previous work showing the stress drop is independent of source dimensions (Aki, 1972; Thatcher & Hanks, 1973; Hanks, 1977; Scholz, 1982; Allmann & Shearer, 2009). The rupture area then indicates the maximum area that can be ruptured by a hypothetical aftershock at that particular location. We calculate this maximum possible rupture area for each positive CFF zone at each distance for all realizations of fault surface so that we have a statistical ensemble for many different ruptures.

Results

Figure 4 shows the change in (a) normal and (b) shear stress in a rectangular area extending from 20 to 60 km along the fault and from -15 to 15 km across the fault. As seen in the plot, the stresses are spatially heterogeneous but the negative stresses can be seen to dominate the modeling domain, particularly for locations not in the immediate vicinity of the fault surface. We refer to the area near the fault where stresses are highly heterogeneous as the "near-fault" region, while we term the more distant region where stresses are more uniform the "far-fault" region. However, we note that though both of these regions are very close to the fault when viewed on a tectonic scale. The extent of these regions is shown in Fig. 5. We focus our discussion on the near-fault region, as it is the region where the fault roughness effects are dominant. The magnitude of the stress fluctuations decrease as the distance from the fault increases and we note that more uniformity in the stress change is observed at greater distances.

In Fig. 4, we find that zones near the hypocenter exhibit larger stress changes than the changes that are observed for sections into which the rupture has propagated. This behavior is observed in all of our simulations. The presence of these zones is related to the nucleation procedure used to start the dynamic rupture. In the case of Fig. 4, the rupture was initiated at a point 39 km along fault distance with a width of 3 km as is noted in Fig. 4.
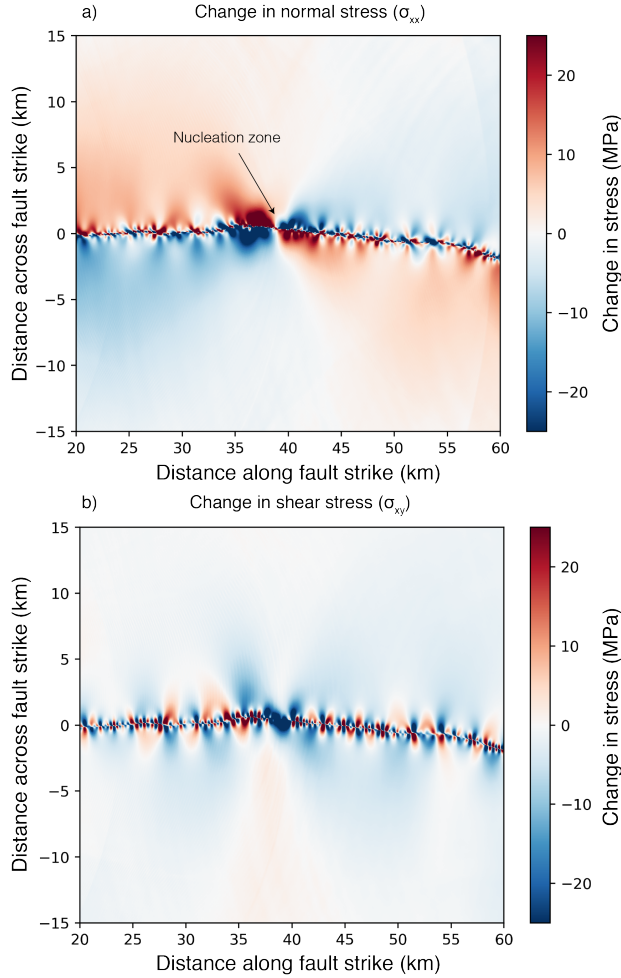
Fig. 4: Change in stresses at the central part of the domain (taken from 20 to 60 km along fault and -15 to 15 km across fault distance) for a self-affine fault with a Hurst exponent of 0.6 and have normalized RMS deviation from planarity of 0.01. The final shear stress is taken once the simulation reaches a time long enough that there are no dynamic stresses related to the wave propagation and stress change is solely due to static stress changes. This complicated shear stress change will also give a complex Coulomb stress change. a) Change in normal stresses. The location of the nucleation zone is marked at a distance of 44 km along the fault strike. b) Change in shear stress for the same realization of the fault profile.

After extracting shear and normal stresses for all of our simulations, we calculate the CFF on receiver faults near the main fault with orientations parallel to the trace of the main fault. Using stresses from Fig. 4, the calculated CFF change is shown in Fig. 5 (a) for the same fault realization. The CFF is highly heterogeneous with positive and negative CFF changes visible around the fault. The negative CFF change values dominate the far-fault region, while mixed positive and negative CFF values dominate the near-fault region. It is important to observe that there are many lobes of positive CFF change in the near-fault region due to roughness of the fault profile. Three of these lobes are labeled on Fig. 5 with labels A, B and C. These positive CFF lobes are potential sources of aftershocks, particularly since the areas where they appear would be seen as stress shadows in typical static stress change calculations due to insufficient resolution of the fault slip. At far-fault distances, negative CFF zones dominate, since the fault roughness effects are not present in the far-fault regions.

Since we calculate the CFF for each individual fault realization, we estimate the width of the near-fault region on each side of the fault in each realization. We do this by calculating the maximum distance away from the fault with more than five positive CFF zones. We do not see any significant variation of the near-fault region width with the value of H. This is evident from Fig. 5 where the width of the near-fault region for $H = 1$ and $H = 0.6$ is shown for RMS ratio of 0.01. We find that the width of the near-fault region changes with the RMS ratio of the fault roughness. Decreasing the RMS ratio from 0.01 to 0.001, we see a decrease in the width of the near-fault region. Using the simulation results, we can calculate the average width of the near-fault region over all of our realizations. The average width of the near-fault region on either side of the fault is ~ 2.7 km for fault profiles having RMS height of 0.01 and ~ 0.9 km for faults having RMS height of 0.001. For distances greater than this width, we observe fewer than five zones with positive CFF. In the far-field, the CFF function is always negative; thus there is an intermediate region with between one and five zones of positive CFF. This region starts where the near-fault
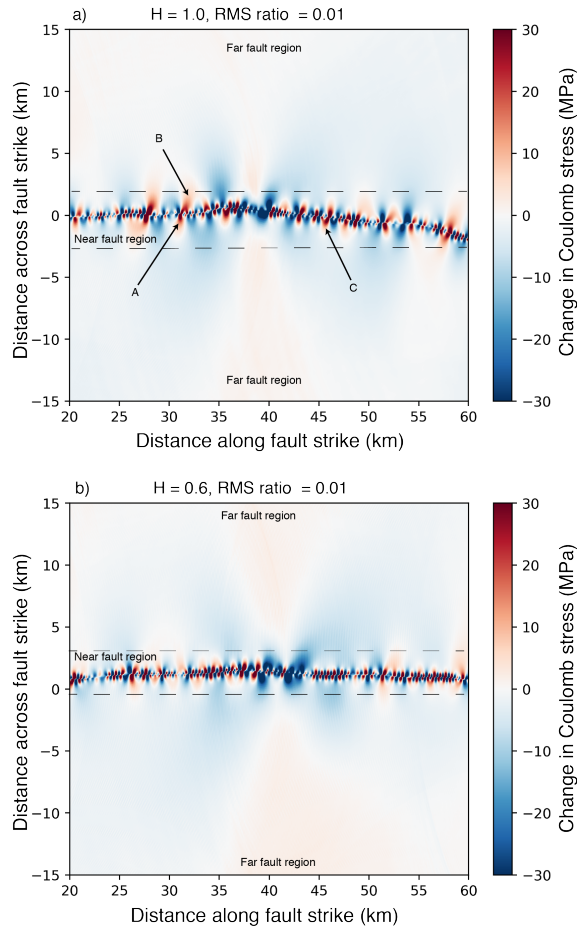
Fig. 5: Change in CFF in the central part of domain. a) The CFF is calculated from the shear and normal stress change (Fig. 4) around the fault due to dynamic earthquake slip on the fault. The Hurst exponent of the fault surface is 1.0 and the normalized RMS deviation from planarity is 0.01. The calculations assume an elastic off-fault material with a friction coefficient of $\mu = 0.4$ and a fault orientation parallel to the overall trace of the main fault. Fault roughness introduces heterogeneous stresses within the main shock rupture area that could promote aftershock production. Positive values indicate increased likelihood of failure, while decreased values are expected to be regions with reduced seismicity. The near-fault and far-fault zones are roughly marked based on the extent of CFF heterogeneity observed in the figure. (b) The CFF is calculated similar to (a) but for a fault surface having a Hurst exponent equal to 0.6 and a normalized RMS deviation from planarity of 0.01.

region ends and reaches to a maximum distance of ~ 5.5 km away from fault for the case of RMS of 0.01. Points beyond the intermediate region are part of the far-fault region.

We examine the statistical properties of the change in static stresses by combining the results for all 100 realizations for each value of H and the RMS height. For computing the CFF function, we only consider those ruptures that have propagated at least 50 km. We see that under our given set of initial conditions (Table 1), all the ruptures with a fault profile having RMS height of 0.001 reach this distance and for fault profiles with RMS height of 0.01, 93% of the ruptures reaches this distance. Figure 6 shows the probability density function (PDF) of CFF as a function of distance from the fault for different RMS ratios and Hurst exponents. The CFF values are highly variable in the near-fault region and include both positive and negative values. As the distance from the fault increases, the range of CFF values squeeze into a narrow range, and for distances further from the fault, we see CFF values cluster tightly around the mean CFF value. We refer to the approximate distance where we see this transition from a large spread of CFF values to a narrow range as the "threshold distance." This distance roughly marks the boundary between the near-fault and intermediate region described above. As is evident from Fig. 6, the location of the threshold distance is controlled by the RMS height of the fault profile and it does not depend strongly on H. Figure 6 (c) shows the results for a smoother fault with an RMS roughness of 0.001, which exhibit an extra band of CFF values that differs from the main band of CFF values. This additional band is due to the hypocentral CFF zones for faults having RMS of 0.001 and reaches distances as large as 5 km away from the fault. The hypocentral zones does not affect the CFF statistics of the positive CFF zones. This is evident in Fig. 6, where no extra bands of CFF values are observed towards the positive side of CFF values.

We also analyze the behavior of the mean CFF with distance under different receiver fault orientations. We change the receiver fault orientation successively from $0°$ to $20°$ from the main fault and observe the pattern of CFF change with distance for each
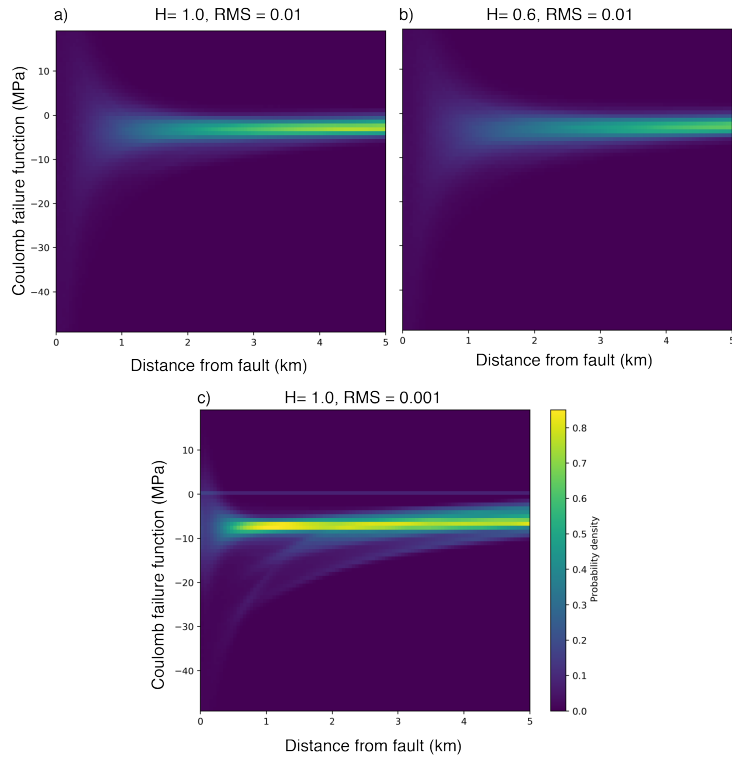
Fig. 6: The probability density function (PDF) values of the CFF relative to the initial stress tensor versus distance away from the fault self-affine fault with a Hurst exponent of 0.6 and a normalized RMS deviation from planarity of 0.01. A wider spread of CFF values can be seen near the fault and this spread squeezes into a narrow band as the distance from the fault increases. This behavior occurs because in the near-fault region, the heterogeneous stress changes due to fault roughness are dominant causing stresses to be highly heterogeneous, while the far-field values collapse to the average stress drop for an earthquake in our suite of simulated events. (a) PDF of CFF change for $H = 1.0$ and RMS of 0.01, (b) same as (a) but for $H = 0.6$ and RMS of 0.01, (c) same as (a) but for $H = 0.6$ and RMS of 0.001. We see an extra band of CFF values that differs from the main band of CFF values. This additional band is due to the hypocentral CFF zones for smoother faults, as the hypocentral zones reach distances as large as 5 km away from the fault.

27

receiver fault orientation. The behavior of the CFF function with distance does not vary significantly when receiver fault orientation angle is changed, although there is an overall change in the average CFF value at each particular distance.

Figure 6 shows one point statistics of our simulation results; however aftershock zones require rupture of a patch of a particular size. Therefore, to relate our results to aftershock occurrence, we must examine the spatial correlations in the resulting CFF distributions. To examine this question, we calculate the locations as well as lengths of probable aftershocks zones using the CFF results. In all of our rough fault scenarios, the probability of occurrence of negative CFF values is greater than the probability of occurrence of positive CFF values. This suggests that we have more zones of seismic inactivity compared to zones of probable aftershock occurrence in the near-fault and intermediate regions. To verify this for the near-fault region, we count total number of positive and negative CFF zones having lengths greater than 500 m at 1.5 km away from the fault in each rupture simulation. Figure 7 shows the number of positive and negative CFF zones in each realization of the fault profile for all 100 fault profiles having $H = 1$ and RMS ratio 0.01 at a distance 1.5 km away from the fault. We can see that the number of negative CFF zones is greater than the number of positive zones in the near-fault region. Though we observe fewer positive CFF zones when compared to negative CFF zones in the near-fault region, their count (average ~ 15) is still much higher than the number of zones we would expect based on typical static stress calculations. These positive CFF zones can potentially trigger earthquakes whose size is small enough to fit in these zones and hence explain aftershocks that appear in stress shadows in static stress calculations based on observational data. Based on positive CFF zone lengths, we next estimate the maximum magnitude earthquake that each of these zones can host. To do this, we consider the resulting earthquake if each zone were to host a rupture of circular shape and we estimate the rupture area by calculating the length of the rupture at a specific distance away from the fault. Figure 8 shows the possible rupture areas of 5000 arbitrarily selected positive
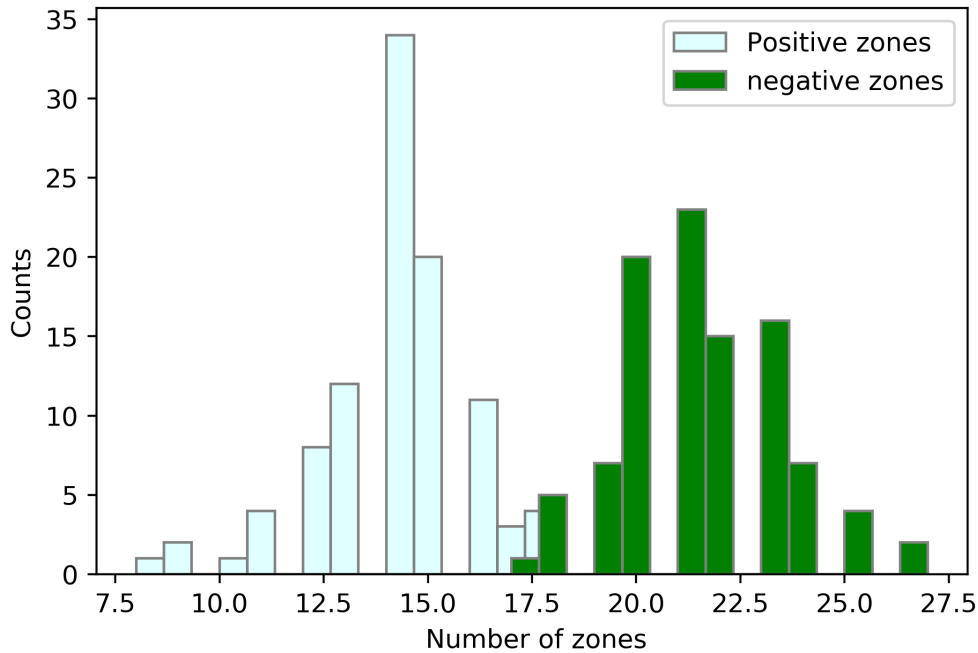
Fig. 7: The figure shows the histogram constructed of the total number of zones with positive or negative changes in the CFF in each simulation using data from all the simulations for a rough fault with Hurst exponent equal to 1.0 and a normalized RMS deviation from planarity of 0.01. The data is taken for CFF zones calculated at a distance of 1 km away from the fault in the near-fault region. The positive CFF change zones occur less frequently than the negative CFF change zones, but the number of positive CFF change zones calculated are many times higher than the number that would be calculated using typical static stress calculations. These positive CFF change zones are the zones that static triggering models suggest could host aftershocks of the simulated ruptures.
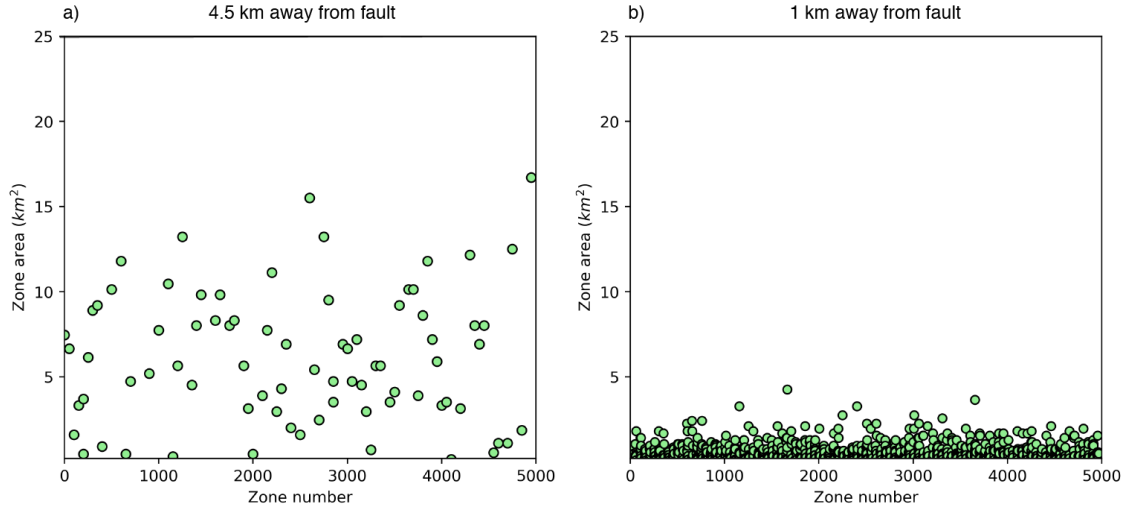
Fig. 8: Figure shows the modeled maximum rupture areas of positive stress change zone at a particular distance from fault in the near-fault zone. (a) Zone area calculated for positive CFF zones at 4.5 km away from the main fault. (b) Same as (a) but for positive CFF zones at 1 km away from fault. There are more positive CFF zones i.e. the zones prone to aftershocks close to the fault (~ 1 km) and these zones have smaller areas. Away from the fault (~ 4.5 km) there are comparatively fewer aftershock prone zones but these zones tend to be larger than the zones found 1 km from the fault.

CFF zones at two different distances away from a fault having $H = 1$ and RMS ratio of 0.01. The distance away from the fault is chosen so that we can observe the behavior of probable rupture areas both in near-fault region and intermediate region. We see that small rupture areas dominate at near-fault distances (~ 1 km) as shown in Fig. 8 (a), while comparatively larger rupture areas are seen at larger distances (~ 4.5 km) in the intermediate region as can be seen in Fig. 8(b). This is because the fault roughness (particularly shorter wavelengths) dominate at regions close to the fault, resulting in many small positive CFF zones. On the other hand, we see larger zones at greater distances since the shorter wavelength effects are restricted to the near-fault region.

To understand the behavior of rupture area as a function of distance, we plot the joint PDF of all probable rupture zones as a function of distance away from the fault for fault profiles with $H = 1$ and RMS of 0.01 as seen in Fig. 9. Based on our results, we observe rupture zones with small rupture areas (3.5 km^2) as well as large rupture areas

(> 3.5 km^2) in the near-fault region (< 3 km distance away from the fault). In this region, the modeling results suggest that smaller rupture areas have a greater probability of occurrence than larger rupture areas. At larger distances within the intermediate region (> 4 km), we see more large rupture areas than small rupture areas. For smaller distances within the intermediate region (< 4 km), we see a behavior similar to the near-fault region in that both small and large rupture areas are present. In this region, smaller rupture areas are roughly equally probable compared to larger rupture areas, a behavior that differs from the near-fault region. However we note that the aftershock zones with a larger area can host any size of rupture smaller than the area of that zone. This is because our model made the initial assumption of a homogeneous regional stress field, but pre-existing stress heterogeneity is likely to be present in the area, which could cause many of these larger CFF zones to host a number of smaller events. This implies that we also expect smaller rupture areas to occur in the intermediate region. We observe from Fig. 9 that in the near-fault region for distances < 50 m, there is no positive CFF zone with rupture area larger than 5 km^2, suggesting that the probability of occurrence of a larger magnitude aftershock is unlikely at distances extremely close to the main fault. This behavior may also be altered if we relax our assumption of a homogeneous initial stress field. Overall, from Fig. 9, we observe that the rupture areas in the near-fault region are mostly below 10 km^2 with very few reaching above it. In the intermediate region, we see ruptures with comparatively larger rupture areas and some of these rupture areas reach 19 km^2 in this region.
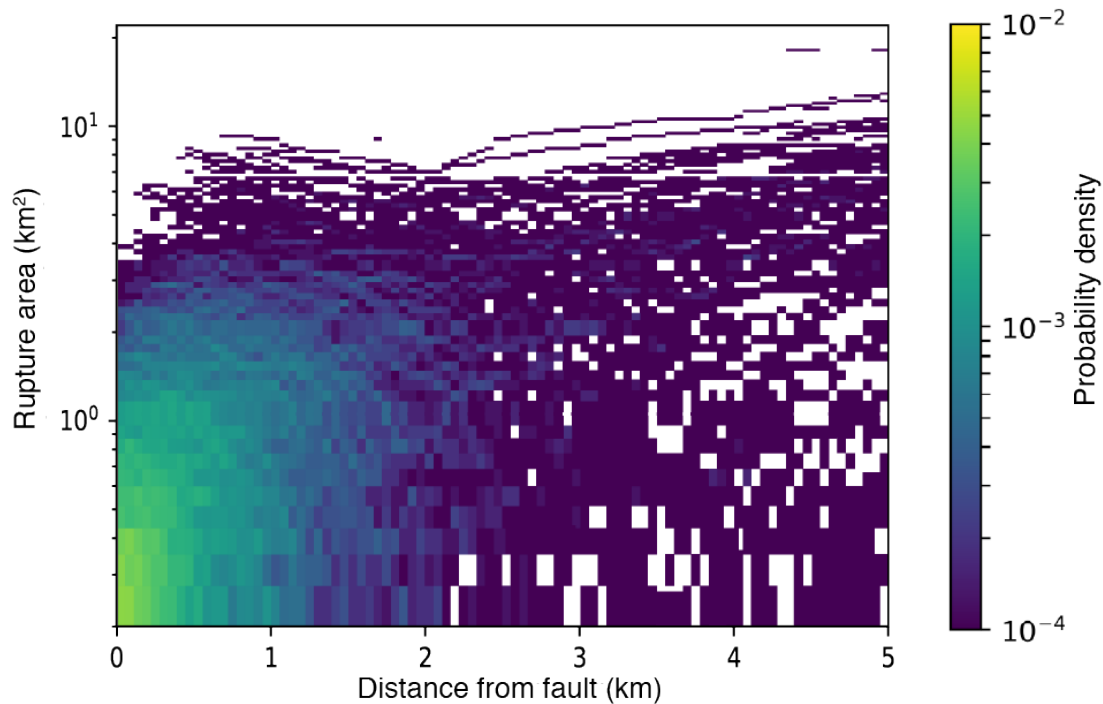
Fig. 9: The plot shows the spatial distribution of positive stress change zones as a function of distance from the fault. The color scale represents the joint PDF values of both parameters (white color means PDF = 0). Our distance scale in this figure represents the near-fault region and the intermediate region. We find high joint PDF values of smaller probable rupture areas in the near-fault region due to the occurrence of many small positive CFF change zones. There are also some larger probable rupture zones present in this region, though they occur less frequently than the smaller ones. In the intermediate region, both larger and smaller rupture zones have a similar probability of occurrence. For natural earthquakes, an aftershock is not required to fill the entire zone, so we expect that we may still find small earthquakes further from fault.

Data Comparison

Our model results describe how the rupture propagation on rough faults perturbs the prevailing stress pattern and defines a spatial CFF pattern in the near-fault region after a major earthquake. We now analyze the observational data of real aftershocks to compare the spatial CFF patterns in our results to those expected for real aftershocks. We take the locations of probable aftershock zones and probable rupture areas from our model results and compare them with the observational aftershock rupture areas and locations. We select five large events from California: the 1984 Morgan Hill Earthquake, the 1989 Loma Prieta Earthquake, the 1992 Landers Earthquake, the 1994 Northridge Earthquake, and the 1999 Hector Mine Earthquake. More details about these earthquakes can be found in Table 2. We use relocated earthquake catalogs from Northern and Southern California starting in 1984 (Shearer et al., 2005; Waldhauser & Schaff, 2008) to extract the aftershocks associated with these earthquakes. We select a fixed time window 5.5 years after the main earthquake to extract aftershocks. This time window is typically used for a magnitude 7 earthquake in southern California (Gardner & Knopoff, 1974; Allen et al., 1965). Detailed information regarding the rupture of these five events is extracted from slip inversions available through SRCMOD, an online database of finite fault inversions for numerous earthquakes (Mai & Thingbaijam, 2014). We translate the magnitude of aftershocks into rupture areas using an empirical relation derived from Hanks & Bakun (2002). Though there are many alternative relationships to convert magnitude into rupture length (Wesnousky, 2008; Hanks & Bakun, 2008; Wells & Coppersmith, 1994), we select this relationship because it takes into account the scaling of small magnitude earthquakes. We also calculate the rupture areas using the seismic moment and the standard Eshelby formula (Eshelby, 1957) assuming a stress drop of 1 MPa. This choice of stress drop value is typical for faults having geometrical heterogeneities (Bailey & Ben-Zion, 2009) or faults with multistrand fault system geometries (Shaw et al., 2015). The rupture areas calculations using Eshelby (1957)

formula are consistent with rupture areas calculations using empirical relation of Hanks & Bakun (2002) and it gives results that are quantitatively similar to those shown here.

We compile a combined dataset by considering aftershocks from all five earthquakes described above. We pick only those aftershocks that are located in the region < 5 km away from the fault rupture to compare them with our near-field model results. There are also some additional aftershocks present at distances > 5 km from fault but we do not consider those since those aftershocks do not provide us any information about the near-fault stress field. Additionally, because the minimum zone length that we consider has an area of approximately 0.2 km^2, we only consider events with M > 3, which corresponds to this minimum area. Figure 10(a) shows the aftershocks for the 1992 Landers earthquake. Due to the Gutenberg-Richter magnitude-frequency distribution (Gutenberg & Richter, 1944), we see most aftershocks with $M_w < 2$. The histogram with respect to distance of these aftershocks (Fig. 10(b)) shows that most of these aftershocks are located very close to the fault. Among all of the events, most of the aftershocks occur between 450 and 500 m away from fault. The magnitude-frequency distribution of the aftershocks shown in Fig. 10(a) is shown in Fig. 10(d). We note that the magnitudes of the aftershocks follow the GR distribution. We also calculate the CFF using the slip model from Wald & Heaton (1994) for the 1992 Landers earthquake for faults parallel to the main fault. Figure 10(c) shows the CFF at 6 km depth, i.e. the focal depth of the 1992 Landers earthquake. We see a prominent stress shadow in the middle of the fault with few positive CFF zones within the main slip area of the fault.

To understand the behavior of the rupture areas as a function of distance, we plot the joint PDF of the rupture area with distance away from fault from our complete compiled data set. This plot is analogous to Fig. 9, but shows observational data rather than our modeling results. As shown in Fig. 11(a), we see a similar behavior to what is observed in our modeling results. Rupture zones with all rupture areas (i.e. both smaller (< 0.45 km^2) and larger (≥ 0.45 km^2)) are present in near-fault as well as intermediate
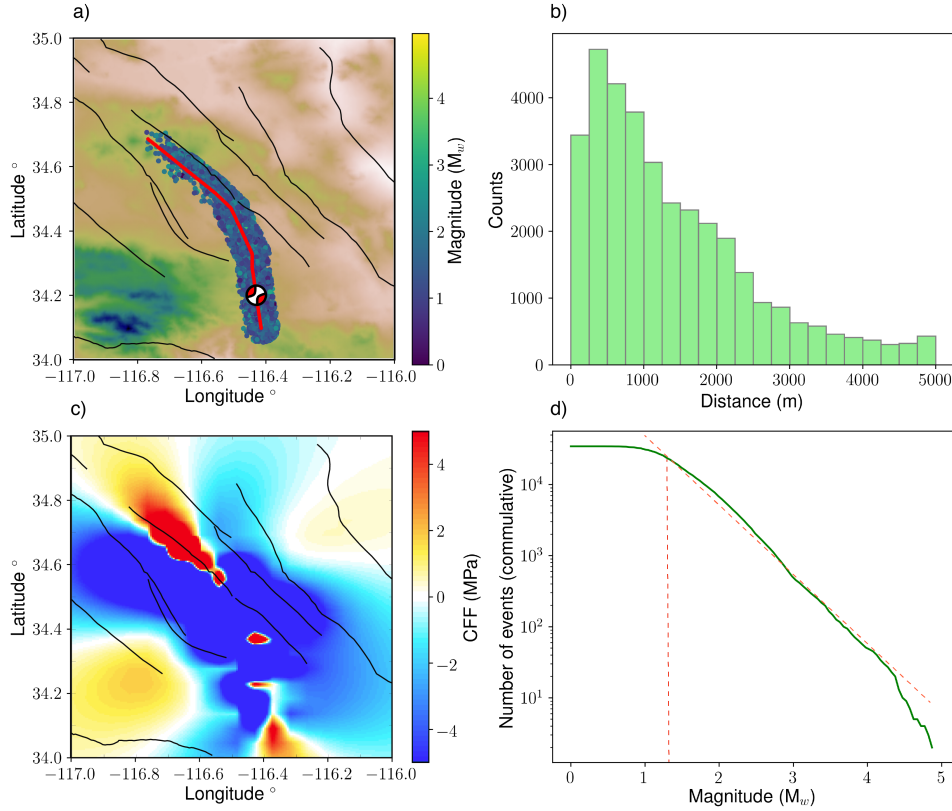
Fig. 10: Characteristics of the aftershock data for the 1992 Landers Earthquake. (a) Map showing aftershock locations in relation to the surface fault trace of the Landers EQ. The fault trace data is extracted from Zeng & Anderson (2000). The focal mechanism is taken from Global CMT solution (Ekström et al., 2012). Aftershocks occurring within 5 km from the fault trace are also shown with their color representing the magnitude. The black lines in the figure show the locations of active faults in the surroundings of the main ruptured fault. We can see that many faults are approximately parallel to the trace of main fault. (b) The histogram of all aftershock distances from the fault plane. The number of aftershocks decreases as the distance away from the fault increases. (c) The CFF calculated for the 1992 Landers earthquake at 6 km depth, on the receiver faults which are parallel to the overall orientation of the main fault. We see few zones of positive CFF change while most part of the near-fault region is dominated by a region exhibiting a stress shadow. (d) The magnitude frequency distribution of the data shown in (a), which follows the Gutenberg-Richter distribution.
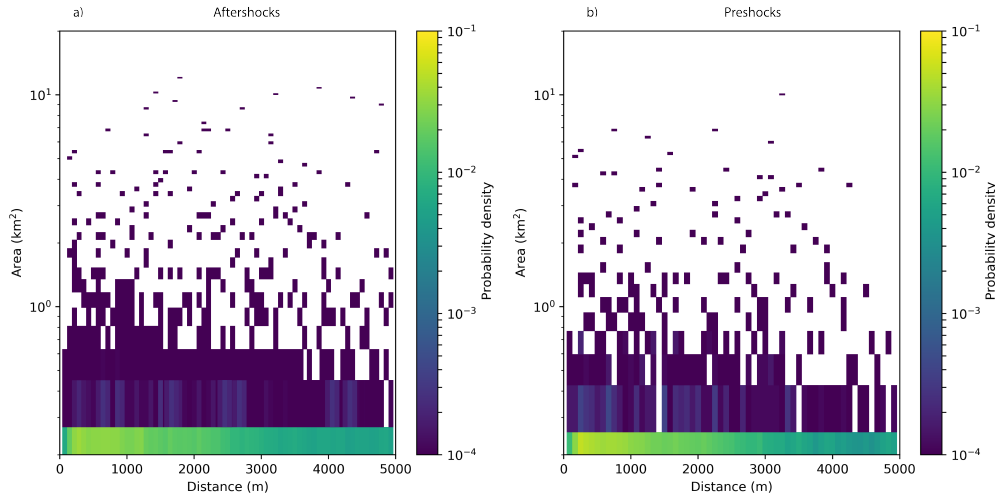
Fig. 11: Spatial and rupture area distributions for aftershocks and preshocks. (a) Distribution of rupture areas and distance from the main fault plane for all the aftershocks that lie within 5 km of the main rupture in our dataset for 5 large earthquakes in California. The data is compiled by combining aftershocks from the 1984 Morgan Hill earthquake, the 1989 Loma Prieta earthquake, the 1992 Landers earthquake, the 1994 Northridge earthquake, and the 1999 Hector mine earthquake. (b) Same as (a), but for events occurring for 5.5 years prior to the same large earthquakes except the 1984 Morgan Hill earthquake. Both datasets in (a) and (b) are similar with no preference for particular magnitudes at certain distance from the fault. This suggests that stresses in the near-fault region are dominated by stress heterogeneity caused by fault roughness over repeated earthquake cycles. The smaller magnitude earthquakes pattern in the near-fault region does not vary much during post-seismic or pre-seismic phase, suggesting that the existing stress field is always very heterogeneous prior to a large earthquake in a manner similar to that found in our simulations.
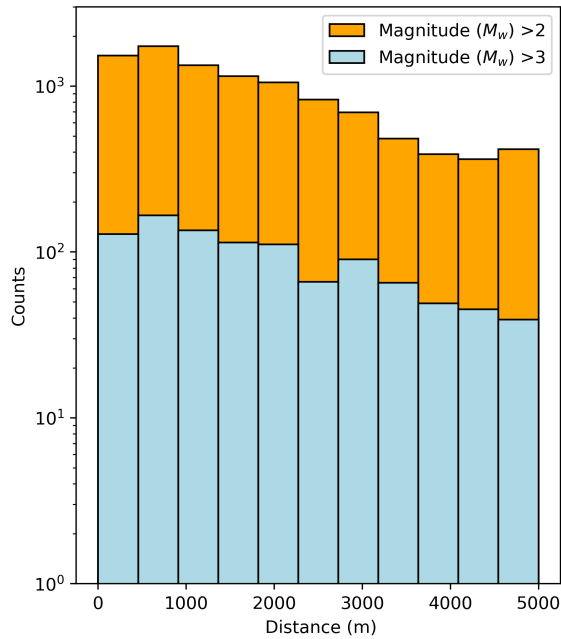
Fig. 12: A comparison of histograms of aftershock distances from the fault plane for two different magnitude ranges. The histogram of aftershock distances from the fault plane for aftershocks with $M_w > 3$ is shown in blue while the histogram of aftershock distances from the fault plane for aftershocks with $M_w > 2$ is shown in orange color. The aftershocks dataset for both histograms is compiled by combining the aftershocks from the 1984 Morgan Hill earthquake, the 1989 Loma Prieta earthquake, the 1992 Landers earthquake, the 1994 Northridge earthquake, and the 1999 Hector mine earthquake. The aftershocks follow the GR distribution at all distances from the fault with an order of magnitude more aftershocks with $M_w > 2$ than aftershocks with $M_w > 3$. Our model suggests this arises due to the fault roughness producing zones of positive stress change of a variety of lengths at all distances from fault, and that these zones can host many smaller events to produce the GR distribution of event sizes.

regions. The smaller rupture lengths are more probable in the near-fault region than the larger rupture lengths, similar to our modeling results. In the intermediate region, we see a relatively high probability of smaller rupture lengths when compared to the larger rupture lengths. Since our modeling results do not preclude smaller events in the large positive CFF zones, we believe that our model is consistent with the higher probability of smaller rupture areas in the intermediate region, though this behavior is not reflected in the probability values in Fig. 9. Figure 12 shows the histograms with respect to distance of aftershocks for two different minimum magnitudes from our complete compiled data set. Based on the comparison of these histograms, we find that the aftershocks in the near-fault region follow the GR distribution, with an order of magnitude more aftershocks with $M_w > 2$ than aftershocks with $M_w > 3$. As seen in Fig. 9, the fault roughness produces many zones of positive stress change with a variety of lengths, and these zones can host many smaller events which will thus produce the GR distribution of event sizes.

To compare our results to seismicity that did not occur in response to an earthquake, we compile a combined dataset by considering events that occurred on the same faults hosting the large earthquakes, with the exception of the 1984 Morgan Hill earthquake due to the start time of the catalog. We select the same time window (5.5 years) for these events. We plot the joint PDF as seen in Fig. 11(b) of the rupture areas (calculated from M_w of preshocks) with distance from fault and see similar behavior to what is observed for aftershocks. For preshock data, we again see ruptures with all lengths in both the near-fault and intermediate regions. Similar to the aftershock data, the smaller rupture lengths are seen to be more probable in the near-fault as well as the intermediate regions when compared to the larger rupture lengths. This suggests that the earthquake stress change did not influence the general decay with distance of earthquakes in the mainshock rupture area, only the temporal characteristics. This suggests that a heterogeneous stress field likely exists throughout the seismic cycle, and its spatial characteristics are not strongly changed by a single earthquake. Rather, a heterogeneous

stress field is maintained and reinforced by complex slip patterns on successive large earthquakes on rough faults.

Discussion and Conclusions

In this work we investigate the occurrence of aftershocks which cannot be explained by traditional static stress change calculations (Kilb et al., 1997; Beroza & Zoback, 1993) or which nucleate in the zones of stress shadows (Segou & Parsons, 2014). We perform dynamic rupture simulations on many realizations of rough faults where the roughness parameters are taken from observational studies (Candela et al., 2012). For each realization of the fault profile, we obtain the static stress change in the volume and then estimate the spatial distribution of static stress change due to dynamic fault slip surrounding the main fault. We observe that the pattern of static stress change is highly complex (Chester & Chester, 2000; Dieterich & Smith, 2009) in the near-fault regions with negative values of stresses more prevalent than positive values. The width of the region where stresses are highly complex depends on the RMS ratio of the fault roughness. We do not find a strong dependence of the width of near-fault region on the H value.

The zones of negative CFF (i.e. the zones not susceptible to aftershocks) are more prevalent in the far-fault and intermediate regions but many of those zones also exist in the near-fault region. In addition to negative CFF zones, there are many positive CFF zones present in the near-fault region. These zones are of particular importance since these are the zones which are locations of potential aftershocks. We count the number of positive CFF zones having length > 500 m in the near-fault region at different distances away from the fault. Based on our data, the average number of total positive CFF zones found in a single earthquake simulation is ~ 15 in the middle of near-fault region. This value is many times higher than the positive CFF zones found from the usual static stress calculations (e.g. (Lin & Stein, 2004; Toda et al., 1998, 2008)) in the near-fault region. Since the positive CFF zones have the capability to host earthquakes whose size is small enough to fit in these zones, they could host earthquakes that appear in zones of stress shadows in

static stress calculations in the near-fault region. However, similar seismicity pattern are observed prior to the mainshocks, suggesting that general stress heterogeneity also exists throughout the seismic cycle and plays an important role in earthquake occurrence.

Furthermore, we calculate the rupture area of each positive CFF zone by considering the possibility that each zone were to host a rupture of circular shape and observe that smaller rupture areas are more dominant inside the near-fault region than the large rupture areas. This is because we have a larger fraction of small positive CFF zones close to the fault due to the fault roughness effects prevailing in this region. The equivalent areas in the near-fault region are mostly below 10 km^2. In the intermediate region, where the fault roughness effects are less important, we see fewer positive CFF zones but larger areas when compared to the near-fault region. Based on our modeling results, we conclude that the aftershocks occurring in the near fault region of a rough fault are result of complex static stress change pattern resulting from the stress heterogeneities introduced by fault roughness over many seismic cycles.

Our comparison between aftershock data and preshock data provides a method for understanding how the stress perturbations due to fault roughness affect the seimicity patterns in the near-fault region. We see that both aftershocks and preshocks show similar spatial characteristics, suggesting the stress heterogeneities driving their occurrence are similar. Based on the similarities of behavior of both datasets, we believe that stresses in the near-fault region are always heterogeneous as suggested by some other observational studies using InSAR and GPS data (Erlingsson & Einarsson, 1989; Pedersen et al., 2003). Our results show that these near-fault stresses are dominated by stress perturbations caused by fault roughness throughout the history of the earthquake cycle. We suggest that the locations of small ruptures (either as preshocks or aftershocks) are independent of their timing relative to an earthquake in the near-fault region and are predominately controlled by the stress heterogeneities imposed by fault surface complexity. The occurrence of small aftershocks at all distances from the main fault in the observational data suggests that

heterogeneous stress can cause multiple small events within a patch of increased CFF due to earthquake slip. The pattern of smaller magnitude earthquakes in the near-fault region does not change between the post-seismic and pre-seismic phases, suggesting that the existing stress field is always very heterogeneous.

Aftershock distribution and static stress changes in the context of rough faults has been modeled by many previous studies. Bailey & Ben-Zion (2009) used a quasi-static modeling approach to model the stress drop due to an earthquake on a geometrically heterogeneous fault. They showed that spatial heterogeneity of the fault surface causes the stress drop to significantly reduced (an order of magnitude lower) as compared to traditional estimates with a homogeneous fault. Smith & Dieterich (2010) performed quasi-static modeling with heterogeneous fault geometry to capture the occurrence of aftershocks in stress shadows and temporal changes in the focal mechanisms of aftershocks. Shaw et al. (2015) used a quasi-static modeling approach with a multistrand fault system geometry to explain the reduced ground motions for aftershocks observed in the near-fault regions. They showed that the observed reduced ground motions in the near-fault region are due to the smaller stress drop of aftershocks (compared to mainshock of similar magnitude events) in this region. Our results agree with these static calculations in terms of the general statistical trends that emerge when stress changes are averaged along strike and over many ruptures. Further work is needed to assess the similarities of the predictions for individual events, and if the stress changes exhibit the same variability along strike when dynamic rupture effects are included.

The near-fault zone of natural faults exhibits a complex damage pattern (Myers & Aydin, 2004; Faulkner et al., 2003; Andrews, 2004, 2005; Rice et al., 2005) and this pattern may further introduce second order stress perturbations. The near-fault region of high damage (sometimes referred to as a weak zone), is observed to strongly influence the geographical distribution of seismicity both before and after a major earthquake (Hauksson, 2011, 2010) . Powers & Jordan (2010) showed that the width of this near-fault

region of high damage is controlled by the stress variations caused by the fault roughness. Our results also show that the width of the near-fault region and stress field heterogeneity (which in turns control the geographical distribution of seismicity) is controlled by the roughness of the fault and that this roughness computed dynamically gives similar results to quasi-static calculations. Some discrepancies in our model results and real data may arise due to the secondary static stress changes (secondary triggering) associated with the secondary earthquakes (aftershocks) that occur as a result of a major earthquake (Meier et al., 2014). Some studies suggest that every single earthquake has its role in redistributing the prevailing static stresses (Meier et al., 2014; Marsan, 2005; Hanks, 1992; Kagan, 1994; Helmstetter et al., 2005), an effect not captured by our simulations. A further effect influencing the off-fault stresses include yielding of the off-fault material due to plastic deformation (Dunham et al., 2011c,a; Gabriel et al., 2013; Shi & Day, 2013; Andrews, 2005) that may alter the spatial pattern of stress change. This topic will be the subject of future work.

We assumed a pre-defined single receiver fault orientation to calculate static stress changes. Since the realistic fault systems do not always include parallel faults, calculating the static stress change with multiple receiver fault orientations may improve the spatial distributions of aftershocks. Hainzl et al. (2010) showed that their aftershock model with multiple receiver fault orientations showed a good agreement with directly triggered aftershocks from 1992 $M7.2$ Landers earthquake. We will consider calculating the CFF using multiple receiver faults in future work, using calculated fault orientations from the off-fault damage. This method will address the open question regarding if the spatial decay of seismicity is due to the stress field or the damage zone. This approach can also examine if the fault orientations derived from dynamic simulations provide additional benefits over those assumed in static calculations.

The stress changes due to co-seismic slip on an earthquake can cause a pore-pressure variation in the region surrounding the main fault which can change the strength of host

faults to initiate further earthquakes (Nur & Booker, 1972; El Hariri et al., 2010; Gupta, 2002; Chen et al., 2012). Furthermore, the diffusion of pore-pressure can cause seismicity to migrate over time (Chen et al., 2012; El Hariri et al., 2010). Similarly, a time-dependent increase in pore pressure due to passing seismic waves can also increase seismicity of a region as observed in many locations with geothermal or volcanic activity (Hill et al., 1993; Freed, 2005). Aseismic slip can also modify the stresses on the fault and bring it close to failure, changing seismicity over time (Vidale et al., 2006; Vidale & Shearer, 2006) and causing more aftershocks to occur. Constraining the effect of fluid flow and aseismic slip on the aftershock triggering is a challenging problem (El Hariri et al., 2010; Vidale et al., 2006; Vidale & Shearer, 2006), and in particular isolating the role of each of these mechanisms in aftershock triggering is not straightforward (Lohman & McGuire, 2007; Vidale & Shearer, 2006). Some studies suggest that both of these mechanisms work together (Hainzl, 2004; Waite & Smith, 2002), and are common in areas of earthquake bursts and swarms (Vidale et al., 2006; Vidale & Shearer, 2006; Hainzl, 2004). We do not model the pore pressure or aseismic slip, and our observational data may include effects from these mechanisms. Additionally, the observational data may include effects from heat flow, topography, V_p/V_s ratio, crustal thickness (Hauksson, 2011) and material contrasts (Rubin & Ampuero, 2007; Rubin & Gillard, 2000) which we did not consider in this study. However, we note that our results are consistent with overall trends in the spatial locations of seismicity, suggesting these additional mechanisms may be more important for describing the transient behavior of aftershocks rather than their spatial occurrence patterns.

Our simulations are in 2D but real earthquakes occur on faults in 3D, an effect which is not captured in the present study. By running simulations in 3D, the rupture process will not always be coherent in the third direction (Dunham et al., 2011c; Shi & Day, 2013), which may cause some differences in the stress change pattern surrounding a fault compared to our 2D model results. Our initial simulations are in 2D due to the fact that 3D simulations are much more computationally expensive. We have also assumed that

the initial stress state is uniform in space, which neglects the previous deformation history of the fault, including the interseismic phase of the seismic cycle to build up stresses to the level of failure. Our results suggest this background heterogenity is important, and it is possible that we can quantitatively account for this history of stress heterogenity by deriving the initial stress state from a long term tectonic model to initiate our model with stresses that are consistent with the slip history of the fault at the start of our simulation. This is a much more challenging computational problem, since the model must resolve both the slow loading of the interseismic period and the rapid slip during the coseismic period, and will be addressed in subsequent work.

Focal mechanisms provide a method to examine the stress orientations compatible with the radiation pattern of a particular earthquake (e.g. (Hardebeck et al., 1998; Steacy et al., 2004; Meier et al., 2014; Hardebeck, 2010, 2015), but since in most cases the focal plane is ambiguous (Nandan et al., 2016), there is always uncertainty involved in determining fault plane orientations and hence the resulting static stresses. Moreover, the alignments of focal mechanisms may not always follow a particular pattern. For instance, large variability of primary focal mechanisms of aftershocks was observed by Mallman & Parsons (2008) during an investigation of world-wide $M > 7$ earthquakes. Similarly, focal mechanisms following the 1989 Loma Prieta earthquake are diverse, and are not aligned with the directions expected for static stress triggering (Beroza & Zoback, 1993; Kilb et al., 1997). While the heterogeneity of alignments of focal mechanisms introduces uncertainty in determining static stresses, this heterogeneity has been proven useful in many cases e.g. the case of central and southern California region, where this heterogeneity has been used to learn the long-term evolution of fault zones and their seismic behavior (Bailey et al., 2010). Similarly, this heterogeneity has been used to estimate the crustal stress heterogeneity in southern California (Smith & Heaton, 2011). Additionally, the effects of static stress changes are not always straightforward to reconcile with subsequent seismicity, such as a spatial correlation observed between stress shadows and seismicity rate reduction

Table 1: List of parameter values used in chapter 2

Parameter name	Symbol used	Value
Model Domain parameters		
Domain length	X_{tot}	80 km
Domain width	Y_{tot}	40 km
Material properties parameters		
Shear wave speed	α	6000 m/sec
Compressional wave speed	β	3464 m/sec
Lame′s parameters	λ and G	32.04 GPa
Friction law parameters		
Static frictional coefficient	μ_s	0.7
Dynamic frictional coefficient	μ_d	0.2
Critical slip distance	D_c	0.4 m
Initial condition parameters		
Stress	σ_{xx}	-100 MPa
Stress	σ_{xy}	45 MPa
Stress	σ_{yy}	-110 MPa
Fault Roughness parameters		
Hurst exponent	H	0.6 - 1.0
RMS height to wavelength ratio	γ	0.01, 0.001

(Toda et al., 2012) at one point in space while a complete absence of a stress shadow (Felzer & Brodsky, 2006) may occur in another region.

Based on our results of dynamic rupture modeling, we relate the spatial distribution of aftershocks in the near fault region of a rough fault to its fractal geometry. Our results provide improved constraints on the magnitude and spatial distributions of aftershock occurrence, which help scientists better understand the basic physics of earthquake interaction and spatial locations of earthquakes in general, an important concern of current earthquake science (Cocco & Rice, 2002; King et al., 2001; Hill et al., 2002). Such knowledge is essential for improving estimates of future hazard and risk in earthquake-prone areas worldwide.

Table 2: List of major earthquakes used in chapter 2.

Earthquake	Mw	Epicenter location	Rupture from
1984 Morgan Hill earthquake	6.2	37.32° N, 121.68° E	Beroza & Spudich (1988)
1989 Loma Prieta earthquake	6.9	37.04° N, 121.88° E	Zeng & Anderson (2000)
1992 Landers earthquake	7.2	34.02° N, 116.43° E	Zeng & Anderson (2000)
1994 Northridge earthquake	6.6	34.21° N, 118.54° E	Zeng & Anderson (2000)
1999 Hector Mine earthquake	7.1	34.59° N, 116.27° E	Salichon et al. (2004)

Chapter 3

Effect of fault roughness on aftershock distribution: Plastic off-fault material properties

Abstract

We perform spontaneous earthquake rupture simulations on rough strike-slip faults with off-fault plastic material properties. We examine the off-fault stress change and co-seismic damage pattern resulting from dynamic fault slip. We use the stress output from each simulation to calculate the Coulomb failure function (CFF). We calculate the CFF values on the extensional and compressional side of the fault using parallel receiver fault orientations. We also calculate the CFF values on the extensional side of the fault using variable receiver fault orientations determined using the angle at which plastic shear strain is maximum. We calculate the probability density function (PDF) for the CFF values across the fault as a function of distance. We observe a similar overall trend of the CFF values with distance for the extensional and compressional sides - our simulations show a broad range of values in the near-fault region, while a narrow range of values occurs further from the fault. In the near-fault region, we observe many more positive CFF change zones using variable receiver fault orientations than using parallel orientations. We calculate the areas and amplitudes of these positive CFF zones as a function of distance away from fault. Our comparison of CFF amplitudes as a function of rupture area suggests that the spatial aftershock distribution surrounding a fault is controlled by both stress heterogeneity as well as the co-seismic damage zone complexity. The calculations of rupture areas using our model are consistent with ruptured areas of observed aftershocks in California.

Introduction

An earthquake causes stress changes in its surrounding region. These induced stress changes can either increase or decrease the seismic activity of that region (Steacy et al., 2005; Stein, 1999; Freed, 2005; Lin & Stein, 2004; King et al., 1994; Stein, 2003; Lin & Stein, 2004; Toda et al., 1998, 2005). This change in seismic activity due to stress changes is referred to as earthquake triggering (Freed, 2005). Understanding the mechanics of aftershock triggering is an important aspect of earthquake science, as an understanding of time-dependent earthquake rates helps constrain the risk they pose to humans and property (Scholz, 2002; Hill et al., 2002; Cocco & Rice, 2002; King et al., 2001). Many studies have been dedicated to understanding aftershock triggering and have proposed different triggering mechanisms. These effects include changes in static stress(Harris & Simpson, 1992; King et al., 1994; Stein, 1999), dynamic stresses from passing seismic waves (Gomberg et al., 2003; Hill et al., 1993; Pankow et al., 2004), aseismic afterslip below a rupture fault plane (Perfettini & Avouac, 2004)), fluid pressure variation due to its flow (Nur & Booker, 1972) and visco-elastic relaxation in the asthenosphere (Lippiello et al., 2015). Although all of these mechanisms are believed to play a role in aftershock triggering, the relative importance of each mechanism remains an open issue in earthquake science. Furthermore, the contribution of each of these mechanisms is not straightforward to quantify (Freed, 2005; Vidale et al., 2006; Vidale & Shearer, 2006; El Hariri et al., 2010).

The static stress changes are calculated based on the Coulomb failure function (CFF) (King et al., 1994; Freed, 2005; Jaeger et al., 2009; Bruhn, 1990). The change in normal and shear stresses on a fault determine the Coulomb stress change for that fault. A positive change in Coulomb stress brings a fault closer to failure, while a negative change in Coulomb stress brings a fault away from failure. The static stress changes can explain many features of seismicity such as the spatial distribution of aftershocks and their temporal sequences, and the seismic inactivity after a large earthquake in a seismically active region (Freed, 2005). The static stress change model has been successful in

predicting the aftershocks observed within distances of 1-2 fault lengths, but even within this distance, this model is not able to explain the occurrence of aftershocks in stress shadows. For instance, the 1989 Loma Prieta Earthquake with moment magnitude (M_w) = 6.9 produced aftershocks in regions of stress shadows within a few fault lengths which cannot be explained by static stress changes (Segou & Parsons, 2014).

To better understand the static stress effects induced by an earthquake, we perform spontaneous earthquake rupture simulations of large earthquakes on a geometrically complex fault. Dynamic rupture simulations solve physics-based model of stresses and slip and hence these models can be used to calculate the static stress changes after the dynamic phase of an earthquake, which gives us an estimate of the expected aftershock triggering locations. Spontaneous earthquake rupture simulations have been extensively used by the earthquake science community (both in 2D and 3D) to understand the physical processes that occur during propagation of earthquake rupture (Harris, 2004; Daub & Carlson, 2008, 2010; Aochi et al., 2000; Dalguer et al., 2003; Bizzarri & Cocco, 2005; Shi & Day, 2013; Harris & Day, 1997; Dunham & Archuleta, 2005; Tinti, Bizzarri & Cocco, 2005; Shi & Ben-Zion, 2006). An advantage of using dynamic rupture models to calculate static stress changes is its ability to resolve small scale details of slip and stress change when compared to kinematically inverted fault models. These small scale details play an important role in determining the near-fault stress change following an earthquake, particularly since the small scale changes in stresses may change the locations and extent of stress shadows over length scales relevant for the typical rupture lengths of smaller aftershocks.

Our dynamic earthquake rupture simulations consider continuum plasticity (Andrews, 2005; Dunham et al., 2011c,a; Shi & Day, 2013; Gabriel et al., 2013) to describe the off-fault material. We consider plastic rather than elastic off-fault material properties (Aslam & Daub, 2018) in this study since the elastic off-fault material properties may predict extreme stress conditions near the rupture front (e.g (Noda et al., 2009)) which are high enough for the material to deform inelastically (Shi & Day, 2013; Johri et al., 2014;

Dunham et al., 2011c,a; Rice et al., 2005; Poliakov et al., 2002). Many recent dynamic earthquake rupture simulation studies have used continuum plasticity to represent off-fault material properties (Andrews, 2005; Ben-Zion & Shi, 2005; Duan, 2008; Templeton & Rice, 2008; Viesca et al., 2008; Dunham et al., 2011c,a; Ma & Beroza, 2008). For example, Andrews (2005) performed dynamic rupture simulations on a flat fault in 2D with off-fault plasticity and observed that the distribution of plastic strain has a uniform magnitude along the fault while its thickness across the fault is proportional to the distance of rupture propagation. Ben-Zion & Shi (2005) performed dynamic rupture simulations in 2D on flat faults with off-fault plasticity and based on the damage observed as a result of different input parameters (normal stress, cohesion, etc...). They noted that the off-fault material damage is significant in the top few kilometers of the crust. Duan (2008) performed dynamic rupture simulations in 2D on flat faults with off-fault plasticity to study the effects of a low-velocity fault zone (LVFZ) on the rupture propagation. They observed larger slip rate values due to the presence of LVFZ and significant amplification of ground shaking in areas within the LVFZ region. Templeton & Rice (2008) performed dynamic rupture simulations in 2D on flat faults with off-fault plasticity in dry materials to learn how different parameters affect and control the extent of off-fault damage during rupture propagation. Viesca et al. (2008) performed similar rupture simulations in fluid-saturated materials to observe how the fluid-saturated material respond to dynamic rupture propagation in comparison to the dry material.

Most of the studies discussed above considered flat faults to perform dynamic rupture simulations. Since real faults are not flat but rather exhibit complex geometries (Renard et al., 2006; Power & Tullis, 1995; Power et al., 1987; Brown & Scholz, 1985; Candela et al., 2012), considering these heterogeneities of the fault surface is important since a real geological fault with geometrical complexities can introduce significant changes in the stress distribution when the fault slips. These stress perturbations sometimes reach the level of existing tectonic stresses of the area (Dieterich & Smith, 2009; Chester &

Chester, 2000) and have a significant effect on the static stress change in the region surrounding the fault. Many quasi-static modeling studies have considered complex fault geometries in order to calculate the slip distribution and resulting stress changes as a result of failure on the geometrically complex fault (Smith & Dieterich, 2010; Bailey & Ben-Zion, 2009; Powers & Jordan, 2010). A few recent studies of dynamic rupture have performed dynamic rupture simulations on geometrically complex rough faults (e.g. (Dunham et al., 2011a; Bruhat et al., 2016; Shi & Day, 2013; Johri et al., 2014; Harris et al., 2018; Fang & Dunham, 2013)) rather than the conventional flat faults to examine the physical processes that occur during propagation of earthquakes for more realistic geometries.

In our previous study (Aslam & Daub, 2018), we performed dynamic rupture simulations on rough faults with off-fault elasticity to study the effects of fault roughness on the aftershocks. We found that the extent of the near-fault region of complex static stress changes is mainly controlled by RMS height of the rough fault profile, and the Hurst exponent of the fault profile does not affect the spatial extent of the near-fault region. Our study assumed elastic off-fault material properties, which provided many insights into the point statistics and expected spatial characteristics of the static stress changes. However, these results may not be relevant when extreme stress conditions are encountered that cause the material to deform inelastically. Similarly, all of our calculations of static stress changes were based on the assumption of a predefined single receiver fault orientation, while the orientations of faults in a multi-fault system may not be parallel in general. Hainzl et al. (2010) observed that incorporating realistic multiple receiver fault orientations changes the spatial pattern of predicted aftershocks, and the new pattern shows better agreement with observed data (i.e. aftershocks of the 1992 Landers earthquake with $M_w = 7.3$). Although our study addressed the question of relating the spatial distribution of aftershocks with the static stress changes in detail, we did not address the relationship of aftershock seismicity with the co-seismic damage zone and multiple receiver fault orientations.
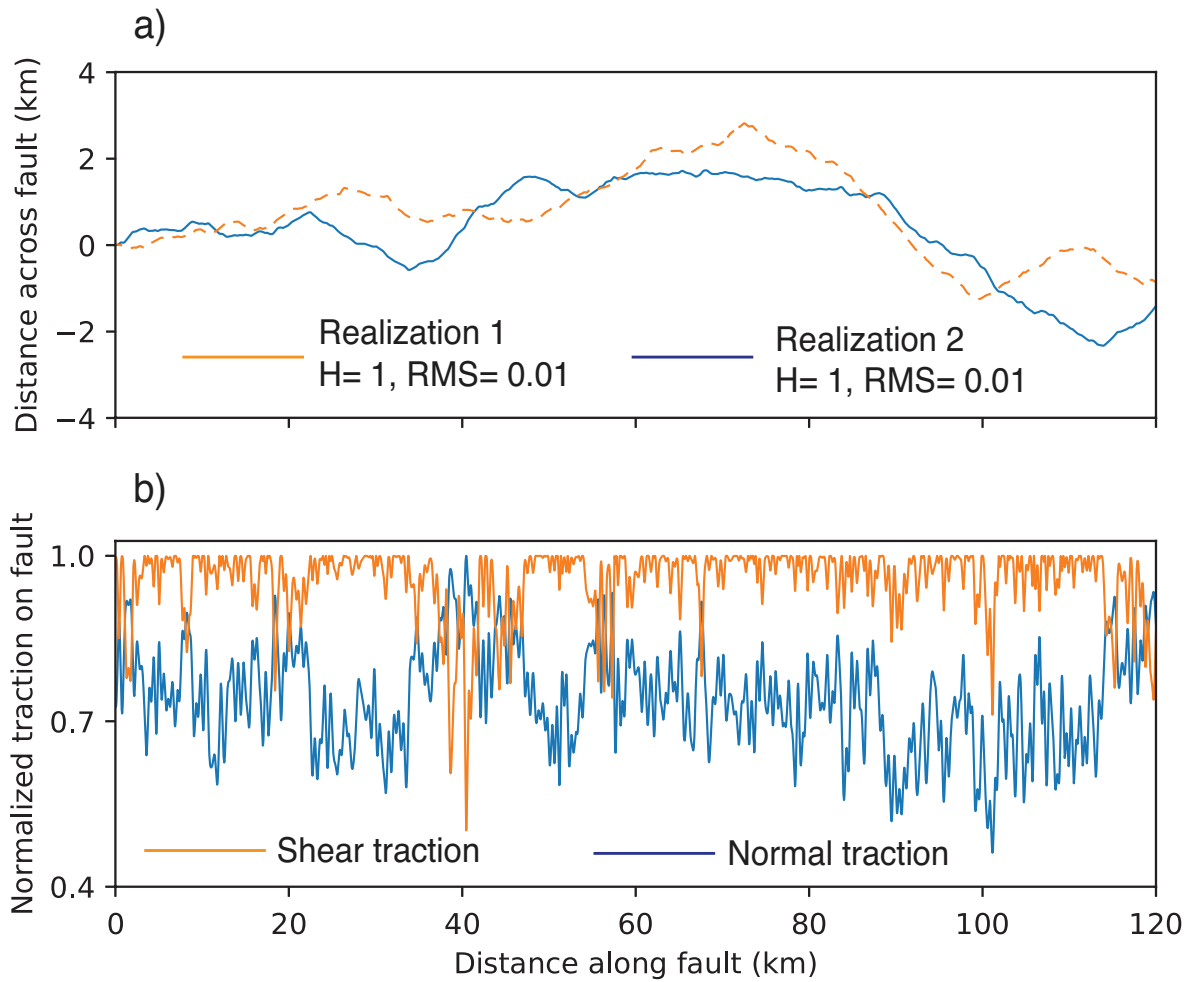
Fig. 13: (a) Two different realizations of a self-similar rough fault with RMS height of 0.01. (b) The normal and shear traction values resolved on realization 2 of the rough fault profile shown in (a). The traction values along the the fault are heterogeneous even though the regional stresses are uniform. The heterogeneous tractions on the fault are solely due to the rough fault profile.

This study expands upon our previous work in order to investigate if the stress field or damage zone controls the off-fault seismic activity. We build upon our previous dynamic rupture studies described above and perform numerous two dimensional (2D) earthquake simulations on rough strike slip fault profiles. We quantify the stress changes in the off-fault material due to dynamic slip on the fault where the off-fault material properties are described using plasticity. We use Drucker-Prager visco-plasticity to account for off-fault material failure. We use self similar fault fractal profiles (Hurst exponent = 1), with fault roughness amplitude values of 0.01 to represent our fault profile. These fault roughness values are taken from major strike slip fault observational studies (Candela et al., 2012). We run our simulations for numerous realizations of the fault profile and then calculate the amplitudes of the CFF for each of these realizations. We calculate the probability density function (PDF) of the CFF from all fault realizations in order to quantify and compare it with the aftershock distributions in space using observational data. We use relocated earthquake catalogs from California (Waldhauser & Schaff, 2008; Shearer et al., 2005) for the comparison of our model results with naturally occurring seismicity.

Inelastic off-fault material response and plasticity

Experimental studies show a pressure-dependent yielding in both rocks and soils (Brace et al., 1966; Hirth & Tullis, 1992; Mogi, 1971, 1974, 1972; Templeton & Rice, 2008). The onset of this inelastic deformation is dependent upon the mean normal stress. In brittle rocks, this deformation occurs as a result of frictional sliding on micro cracks and fractures (Dunham et al., 2011a; Rudnicki & Rice, 1975). We use the Drucker-Prager model to describe this inelastic deformation. This model is similar to the Mohr-Coulomb model and under certain stress states, the yield criterion of both models become equivalent.

Under Drucker-Prager viscoplasticity, the material flows when stresses exceed the yield function $F(\sigma_{ij})$:

$$F(\sigma_{ij}) = \bar{\tau} - c_{DP} + \mu_{DP}\sigma_{kk}/3, \tag{3.1}$$

where $\bar{\tau} = \sqrt{s_{ij}s_{ij}/2}$ is the second invariant of the deviatoric stress tensor $s_{ij} = \sigma_{ij} - (\sigma_{kk}/3)\delta_{ij}$, c_{DP} is related to the cohesion, and μ_{DP} is related to the internal coefficient of friction. When $F(\sigma_{ij})$ is negative, the material behaves elastically (Fig. 14). Since the material close to the fault is already damaged (Chester & Logan, 1986; Chester et al., 1993, 2004; Biegel & Sammis, 2004; Caine et al., 1996), we do not consider any cohesion for the off-fault material. Hence the above equation reduces to

$$F(\sigma_{ij}) = \bar{\tau} + \mu_{DP}\sigma_{kk}/3. \tag{3.2}$$

Our study does not consider the effects of pore fluids, but the effect of fluid pressure can be introduced into this equation by considering the stresses in the above equation as effective stresses for a fluid-saturated medium (Dunham et al., 2011c; Viesca et al., 2008).

For viscoplasticity, the stresses are allowed to exceed the yield function according to

$$F(\sigma_{ij}) = \Lambda\eta, \tag{3.3}$$

where $\Lambda = \sqrt{2\dot{e}_{ij}^{pl}\dot{e}_{ij}^{pl}}$ is the equivalent plastic strain rate from the deviatoric plastic strain rate $\dot{e}_{ij}^{pl} = \dot{\epsilon}_{ij}^{pl} - (\dot{\epsilon}_{kk}^{pl}/3)\delta_{ij}$ and η is a viscoplastic viscosity defining the time scale over which stresses can exceed the yield stress.
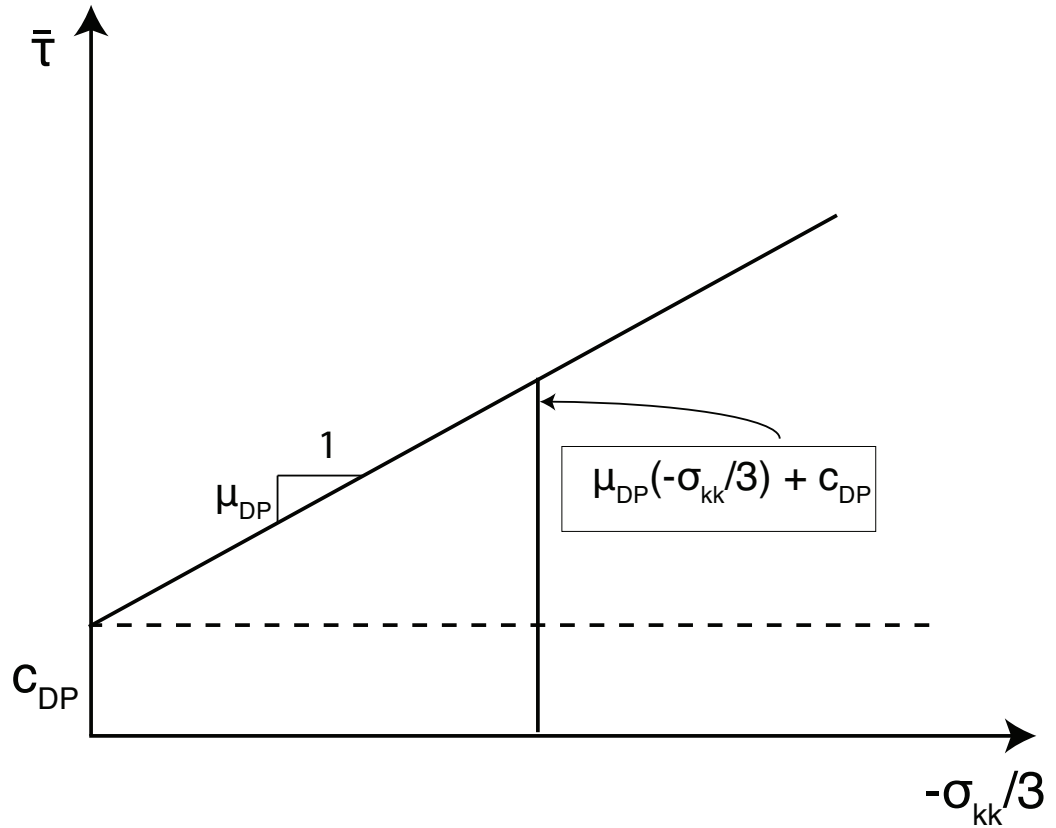
Fig. 14: Yield criteria of Drucker-prager plasticity, which is used to model plastic deformation of rocks in numerical modeling of spontaneous earthquake rupture propagation. In our simulations, we assume a cohensionless off-fault material (i.e. $c_{DP} = 0$), while considering a cohesion value for the material will cause the material to yield at higher stress level.

Fault roughness

Recent studies of fault surface topography measurements (Candela et al., 2011, 2012, 2009; Brodsky et al., 2011; Renard et al., 2006; Sagy et al., 2007) suggest that fault surfaces are self-affine fractals. A few other studies (Brown & Scholz, 1985; Power & Tullis, 1995; Lee & Bruhn, 1996; Shi & Day, 2013) suggest that fault surfaces are better described by a type of self-affine fractals that are self similar fractals. A self-affine fractal profile is one that requires a separate length and height scaling to obtain a similar statistical profile, while a self-similar fractal profile requires same length and height scaling (Russ, 1994). A self-affine fault profile can be described by two parameters. The first parameter is called the Hurst exponent. This parameter quantifies the fractal scaling of the power spectrum of the fault. We denote this parameter by H. The second parameter quantifies the maximum roughness amplitude of a fractal fault profile, which we quantify through the RMS deviation of the fault profile from planarity. This parameter is dependent on the maturity of the fault. A detailed description of the self-affinity and the two parameters can be found in (Aslam & Daub, 2018).

We run all of our simulations in this study on an immature self-similar fault profile. A self-similar fractal fault profile is described by $H = 1$. We describe the immaturity of the fault profile by an RMS height value of 0.01 (Brodsky et al., 2011). We run 500 spontaneous earthquake rupture simulations, each with a different realization of the immature self-similar fault profile (RMS height = 0.01 and $H = 1$) . We use a Fourier method to generate the fault profiles (Andrews & Barall, 2011), and cut off the fractals at a wavelength corresponding to 20 times the grid spacing. Figure 13(a) shows a self-similar fractal fault profile with RMS height of 0.01, while the variation in the shear and normal traction due to the fault profile is shown in Fig. 13(b). The plot of the shear and normal components shows that the geometry of the fault profile causes the tractions to be highly non-uniform, which subsequently alters the slip distribution of the fault when it fails.

Model setup

We use a plane strain model to run all of our spontaneous earthquake rupture simulations. Figure 15 shows a schematic of the model setup. The simulation domain is 130 km long and 70 km wide. The fault surface has the same length as the domain length. The fault profile is a self-similar fractal curve $f(x)$ deviating from $y = 0$, and has a RMS height to wavelength ratio $= 0.01$. We run 500 earthquake rupture simulations each with a different fault surface realization. We do this by changing the fault profile in each simulation, but keeping the rest of the modeling setup the same. We use a fixed grid spacing ($\Delta x = 25$) along strike in all of our simulations. We have run a few simulations with shorter grid spacing in our previous study and determined that the simulations are well resolved at our selected resolution. The minimum resolvable wavelength of fault roughness is 0.5 km based on our selected grid spacing ($\lambda_{min} = 20\Delta x = 0.5$ km). Our simulation are accurate up to frequencies of ~ 7 Hz assuming 20 grid points per wavelength (a Fourier amplitude spectrum of velocity from the near-fault region is provided in Fig. 16). All of our simulations assume Drucker-Prager plastic off-fault material properties. The plastic parameter values used in this study are given in Table 1. We use `fdfault` to run all of our rupture simulations. This code has been verified on multiple SCEC benchmark problems (Harris et al., 2009, 2018) both with elastic and plastic off-fault material properties.

We assume a uniform regional stress field over the whole domain. An important point to note is that when the uniform stress field is resolved on each point along the fault, it provides heterogeneous values of normal and shear traction (due to the geometry of the fault profile) on the fault. As an example, Fig. 13(b) shows the traction values resolved on the fault profile (shown in Fig. 13(a)) due to the uniform stress field given in Table 1. In this study, we represent compressive stresses as negative. We do not encounter any tensile normal traction in our simulations with plastic off-fault material properties.

We use the linear slip weakening (SW) friction law to model friction on the fault
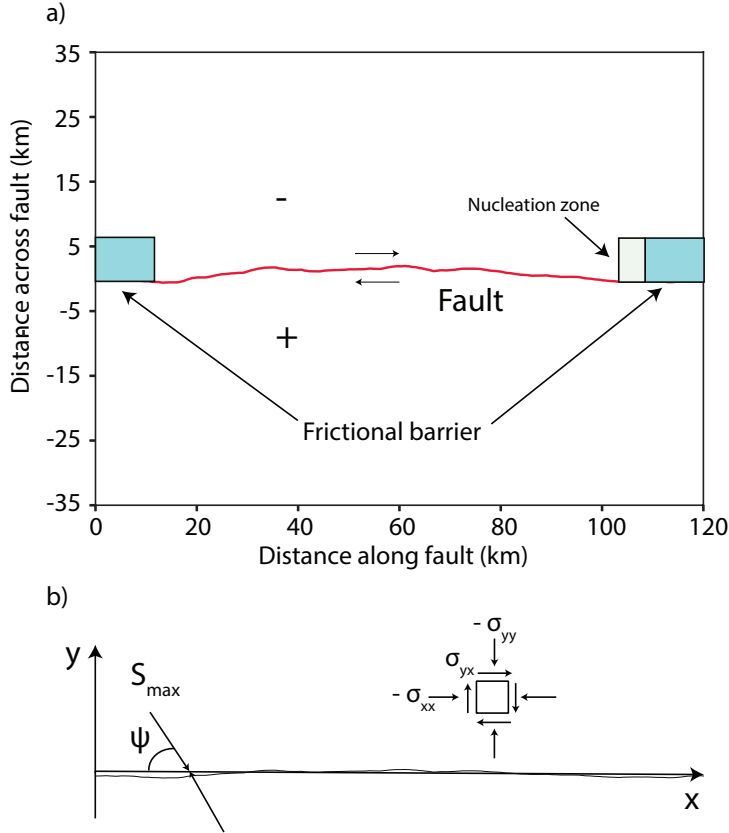
Fig. 15: (a) Modeling setup of our simulations. A self-similar rough fault profile is shown having a RMS height to wavelength ratio of 0.01. The minimum wavelength of the fault roughness is 500 m. The fault has a right lateral strike slip sense of slip, a length of 130 km, and a frictional barrier on either side. The barrier on the left is 15 km long, while the barrier on the right side starts at the edge of nucleation zone and extends to the edge of the simulation domain. The rupture always initiates on the right side of the fault. This results in accumulation of plastic deformation predominantly on the extensional side of the fault. The extensional side is marked in the figure with '−' sign while the compressional side is marked with a '+' sign. In each rupture simulation, the domain setup remains the same while the profile of the rough fault changes. (b) We load the medium with homogeneous stresses while the maximum compressional stress (S_{max}) inclines at an angle Ψ on the fault. We observe plastic deformation predominantly on one side of the fault since the value of Ψ is high (40 degrees) for our simulations (Templeton & Rice, 2008).
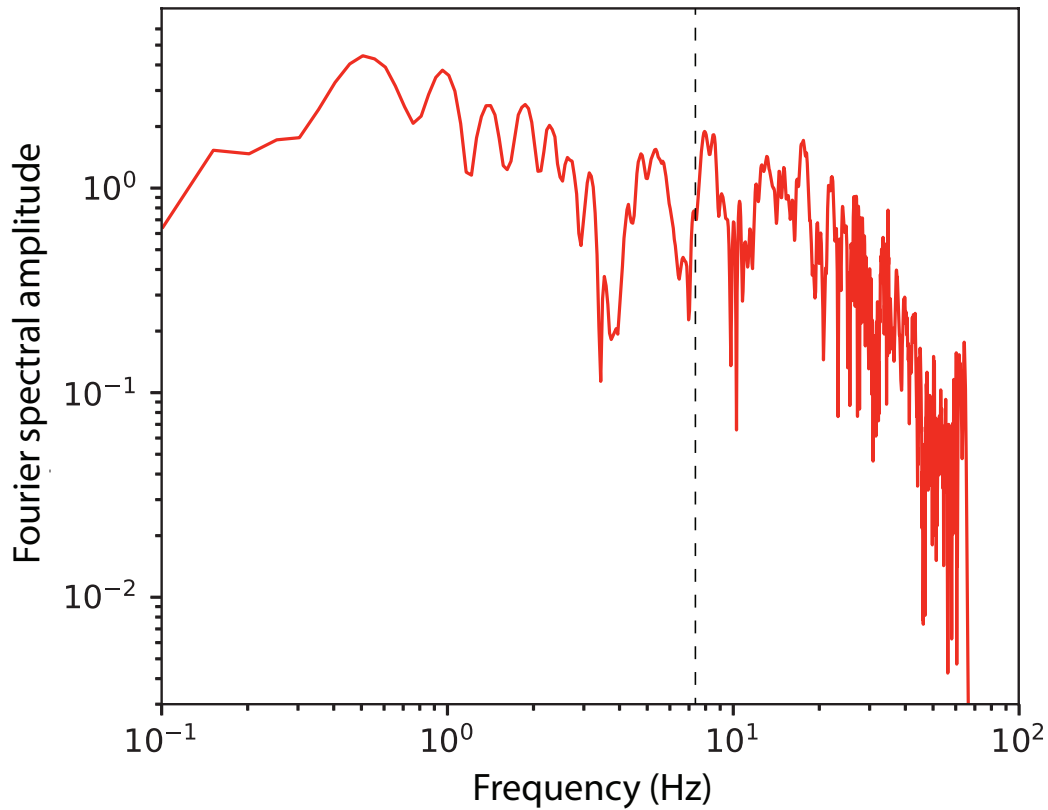
Fig. 16: The Fourier amplitude spectrum of velocity (fault normal) recorded at a pseudo station placed at 1.5 km away from the fault at the extensional side. The spectrum is flat at high frequencies since geometrical heterogeneity of fault profile causes slip heterogeneity along the fault which results in excitation of waves of manny different wavelengths. The vertical line indicates the maximum resolved frequency of our simulations.

(Ida, 1972; Day, 1982; Andrews, 1985, 1976). According to this model, a static friction value μ_s drops to a dynamic friction value μ_d as a function of slip U on the fault over a certain critical slip distance D_c. Although this friction law has a simple formulation (Bizzarri, 2010), it captures the basic weakening characteristics of the friction on the fault and hence has been used in many rupture simulation studies (e.g. (Harris et al., 2009)). This law does not include any healing to friction with time, hence some rupture simulation studies (e.g. (Okubo, 1989; Dunham et al., 2011a,c; Schmitt et al., 2015; Bizzarri & Cocco, 2006a,b)) have used other friction laws such as rate and state friction (Dieterich, 1979; Ruina, 1983) or the Shear Transformation Zone friction law (Daub & Carlson, 2010) to account for the fault friction properties. We choose $\mu_s = 0.7$, $\mu_d = 0.2$ and $D_c = 0.4$ m in this study. A low value of dynamic friction with a higher strength is chosen based on lab experiments (Han et al., 2007; Beeler et al., 2008; Tsutsumi & Shimamoto, 1997; Hirose & Shimamoto, 2005; Di Toro et al., 2004, 2011; Hirose & Bystricky, 2007; Goldsby & Tullis, 2002, 2011) and theoretical/numerical studies (Bizzarri, 2011; Suzuki & Yamashita, 2006; Beeler et al., 2008; Andrews, 2002; Rice, 2006) to provide strong dynamic weakening. Our static friction value for the SW law remains constant but at any time snapshot the friction on the fault is variable along the fault due to the heterogeneous distribution of fault slip. We provide stress drop and some other dynamic rupture properties values in Table 2.

Studies of dynamic rupture simulations show that the plastic strain accumulation occurs predominantly on the extensional side of the fault (Templeton & Rice, 2008; Ben-Zion & Shi, 2005). The extensional side can be defined by the sign of the fault parallel component of the strain tensor (ϵ_{xx}) near the rupture front (Templeton & Rice, 2008). The static stress changes induced by co-seismic slip on the fault during rupture propagation vary in space, with a dependence on whether the point is located on the compressional or extensional side of the fault. Since our main focus in this study is to calculate static stress changes as a result of earthquake rupture, we aim to compare the static stress changes on both the extensional and compressional sides of the fault. To make this comparison more

straightforward, we run a unilateral rupture in all of our rupture simulations. Doing this enables the compression to be dominant along one side of the fault and extension to be dominant along the other side of the fault. We choose the right side of the fault (a 3 km nucleation patch between $80 - 120$ km along fault distance) to initiate slip in all of our rupture simulations. To pick the exact location of the 3 km nucleation patch between the along fault distances of 80 and 120 km, we calculate the shear to normal stress ratio (S/N ratio) at every grid point along the fault, low-pass filter the resulting signal, and choose the location where the S/N ratio is highest. These locations are the places where ruptures are more likely to nucleate (Fang & Dunham, 2013; Oglesby & Mai, 2012; Mai et al., 2005). Since every fault profile does not fulfill this criteria, we generate a large number of fault profiles and calculate the S/N ratio of each of these fault profiles. If the S/N ratio is highest between $80 - 120$ km along fault distance, we keep this fault profile for rupture simulation; otherwise we discard the fault profile. To force the rupture to propagate only towards the left side of the fault, we place a frictional barrier (constant $\mu_s = 1000$) on the right side of the fault. The frictional barrier length starts from the right edge of the nucleation zone and ends at the right fault edge as can be seen in Fig. 15. We select 500 different fault profiles using the above criteria and run simulations on those fault profiles. After running the simulations, 187 ruptures propagate more than 60 km from the nucleation point before dying out, while the ruptures in the remaining simulations die out early due to the unfavorable fault geometry. For our results section, we only consider those 187 ruptures that have ruptured at least 60 km along strike.

Previous researchers have used many strategies to spontaneously nucleate a rupture for the SW friction law (Andrews, 1985; Ionescu & Campillo, 1999; Dunham & Archuleta, 2005; Bizzarri & Cocco, 2005; Day, 1982). Strategies that are commonly used include time independent over-stressing of the fault (e.g. (Harris et al., 2009)) and over-stressing a single node point within a critically stressed nucleation patch (e.g. (Schmedes et al., 2010)). We choose the time independent over-stressing of the fault nucleation patch based

Table 3: List of parameter values used in chapter 3

Parameter name	Symbol used	Value
Model Domain parameters		
Domain length	X_{tot}	130 km
Domain width	Y_{tot}	70 km
Material properties parameters		
Compressional wave speed	V_p	6000 m/sec
Shear wave speed	V_s	3464 m/sec
DP internal friction parameter	μ_{DP}	0.5735
DP plastic dilatancy parameter	β	0.2867
DP viscosity parameter	η	0.2775 GPa.s
Friction law parameters		
Static frictional coefficient	μ_s	0.7
Dynamic frictional coefficient	μ_d	0.2
Critical slip distance	D_c	0.4 m
Initial condition parameters		
Stress	σ_{xx}	-100 MPa
Stress	σ_{xy}	52.0 MPa
Stress	σ_{yy}	-120 MPa
Stress	σ_{zz}	-110 MPa
Fault Roughness parameters		
Hurst exponent	H	1.0
RMS height to wavelength ratio	γ	0.01

on our analysis of different nucleation strategies in our previous study. The fault nucleation patch is 3 km wide while the central point of the patch is the point with the highest S/N ratio. The shear traction on each point of this nucleation patch is increased from its current value to a value defined by the failure stress on the fault: $T_s^{(i)} = 1.01 T_f^{(i)} = \mu_s T_n^{(i)}$, where $T_s^{(i)}$ is the shear traction, $T_f^{(i)}$ is the failure traction and $T_n^{(i)}$ is the normal traction on the ith point on the fault.

Receiver fault orientations and potential aftershock zone calculations

The static stress change on a receiver fault is calculated using the CFF equation. The CFF is based on the change in the normal and shear stress on a receiver fault (King et al., 1994):

$$\Delta\sigma_\beta^f = \Delta\tau_\beta - \mu_\beta \Delta\sigma_\beta. \tag{3.4}$$

Here $\Delta\sigma_\beta^f$ is the Coulomb stress change, $\Delta\tau_\beta$ is the shear stress change, μ_β is the friction coefficient and $\Delta\sigma_\beta$ is the normal stress change on the receiver fault. The subscript β specifies that all the stress values are calculated on the receiver fault plane (i.e. τ_β and σ_β are calculated by resolving the off-fault stresses onto the receiver fault plane). An increase in the CFF value moves the fault closer to failure, while a decrease in the CFF value moves the fault away from failure.

Since the dynamic rupture simulations solve for the stresses directly during slip, we have the complete stress tensor available at the end of the simulation. Once we know the receiver fault orientation, we can calculate the static stress change on the receiver fault. We assume a frictional coefficient value (μ_β) of 0.4, a value typical for strike-slip receiver faults (Parsons et al., 1999).

We treat the compression and extensional sides separately when calculating CFF values. We calculate CFF values on the compressional side of the fault using a single receiver fault orientation. This orientation is parallel to the overall trace of the host fault. The assumption of parallel receiver faults is usually reasonable for strike slip fault zones (Faulkner et al., 2003) or for receiver faults that have formed under a similar tectonic history to the main fault. We calculate CFF values on the extensional side of the fault using the fault parallel receiver fault orientation (similar to the compressional side), and also using a second receiver fault orientation that is spatially variable. We determine this second orientation of the receiver fault using the final plastic strain tensor of dynamic rupture simulation. Using this tensor, we calculate the orientation at which the plastic shear strain is maximum, which should serve as a proxy for the likely orientation of faults in that area due to off-fault damage.

We extract the plastic strain and final stress tensor after a sufficiently long simulation time to ensure that our calculation of the static stress change is not affected by the dynamic stresses due to passing seismic waves. We also select a smaller domain of the model to extract the stress and plastic strain tensor rather the full domain which further

reduces the effects of boundaries and dynamic waves. We extract both tensors after 41.13 s of rupture simulation. Based on the shear wave velocity, this time is sufficient for the waves to propagate away from the central part of the modeling domain. The smaller domain is 50 km long and 40 km wide, beginning at 20 km along fault distance and ending at 70 km along fault distance for the fault parallel direction while starting at -15 km and ending at 25 km across fault distance for the fault perpendicular direction as can be seen in Fig. 17. The dashed vertical lines shows the sub-region along fault strike that is used for analysis. We only consider those ruptures that have ruptured the whole sub-region. This means that we consider a 2D rupture equivalent to a magnitude 7 earthquake (Wells & Coppersmith, 1994) for our analysis.

Once we calculate the CFF on both sides of the fault from all of the simulations, we compute point statistics by combining the calculated CFF values from each realization. We also analyze the spatial and amplitude correlations of these CFF values. We do this by identifying the zones of positive CFF change on each side of the main fault for all 187 simulations and then calculate the size, location and mean CFF amplitude of each zone. We only consider positive CFF zones that have a length of 100 m or more. In addition to the size and location of these zones, we calculate the total number of these positive CFF zones that exist within the selected sub-domain in each realization on each side of the fault. This comparison illustrates how static stress changes (due to co-seimic fault slip) are distributed on the compressional and extensional sides of the fault.

To compare our model results with real aftershock data as described in the following section, we find the distance of each positive CFF zone from the host fault and its area assuming a circular source dimension. The assumption of a circular rupture is frequently used for small to moderate earthquakes (Allmann & Shearer, 2009; Scholz, 1982; Hanks, 1977; Thatcher & Hanks, 1973; Aki, 1972).

Aftershocks and fault trace data

To compare our model results with real data, we select five major earthquakes in California. These events include the Morgan Hill Earthquake of 1984 with $M_w = 6.2$ (Beroza & Spudich, 1988), the Loma Prieta Earthquake of 1989 with $M_w = 6.9$ (Wald et al., 1991), the Landers Earthquake of 1992 with $M_w = 7.2$ (Wald & Heaton, 1994), the Northridge Earthquake of 1994 with $M_w = 6.2$ (Hartzell et al., 1996), and the Hector Mine Earthquake of 1999 with $M_w = 7.1$ (Salichon et al., 2004). We use the relocated Northern and Southern California earthquake catalog (Waldhauser & Schaff, 2008; Shearer et al., 2005) to extract the aftershocks related to the earthquakes described above. We keep a fixed time window after the main shock to extract aftershocks. Previous works have used a magnitude-dependent time window to determine aftershocks (Gardner & Knopoff, 1974; Allen et al., 1965); however, we use a fixed time window to ensure uniform treatment of all events. We extract the fault trace of all the earthquakes described above using the slip inversion of these earthquakes. The slip inversions are freely available through an online database (SRCMOD) (Mai & Thingbaijam, 2014). This database has the record of the estimated slip model for many major earthquakes around the globe through finite fault inversion studies.

To perform a quantitative comparison of the observational data with our model results, we calculate the earthquake rupture area of all aftershocks from the five major earthquakes described above using the standard Eshelby formula (Eshelby, 1957) which assumes a circular source dimension and a constant stress drop value. We assume a stress drop of 1 MPa which is typical for geometrically heterogeneous faults (Bailey & Ben-Zion, 2009; Shaw et al., 2015).

Results

Point statistics

Figure 17(a) shows the pattern of off-fault plastic deformation during one of the rupture simulations. The pattern of off-fault plastic deformation is shown using the
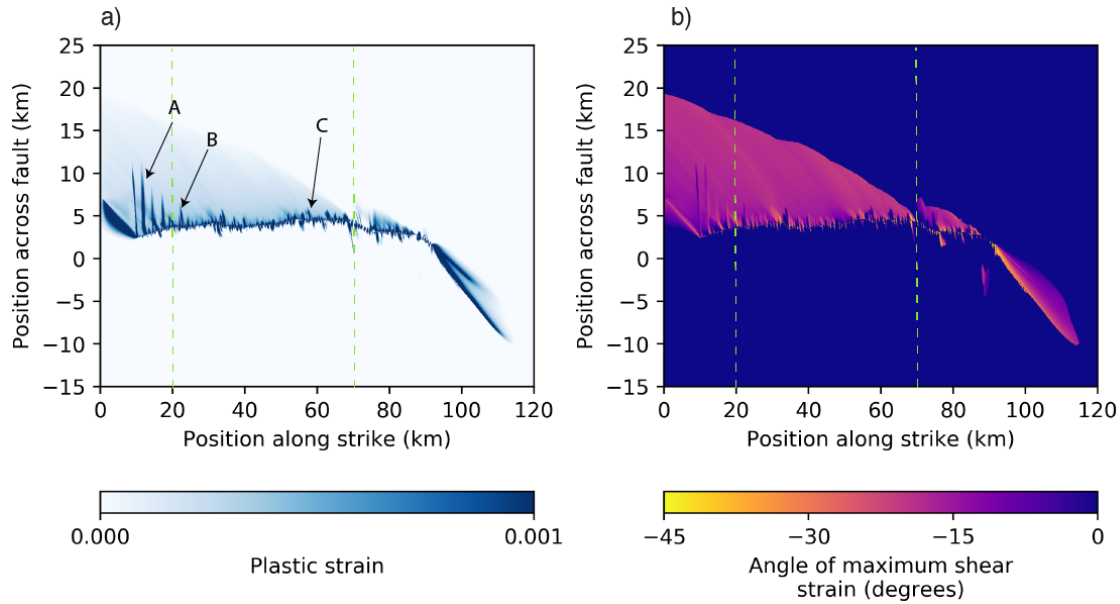
Fig. 17: (a) Snapshot of the pattern of off-fault scalar plastic strain in the modeling domain at time = 41.3 sec after the start of the rupture propagation. We extract stresses and plastic strains from all the rupture simulations at time = 41.3 sec. The modeling sub-domain region (20 to 70 km along fault and -15 to 25 km across fault distance) is also marked with vertical dashed lines. The geometric heterogeneity of the fault profile leads to a complex damage distribution across the main fault. The roughness of the fault profile concentrates the regions of highest plastic strain immediately next to the geometrical fault bends resulting in localized high strain zones marked by 'A', 'B' and 'C'. (b) Estimated receiver fault orientations using the direction of maximum plastic shear strain. The orientations are heterogeneous in space, with orientations mostly within 25° of the main rupture trace. Note that the vertical scale in both (a) and (b) is exaggerated.

equivalent plastic strain γ^p, defined as $\Lambda = \frac{d\gamma^p}{dt}$. The plastic strain accumulates along the extensional side of the fault as observed in many other studies (Templeton & Rice, 2008; Ben-Zion & Shi, 2005; Andrews, 2005) with the width of plastic deformation zone increasing with the rupture propagation distance. The roughness of the fault profile concentrates the regions of highest plastic strain immediately next to the geometrical fault bends. These high strain zones tend to be localized in space due to stress concentrations as shown in Fig. 17(a). Some of these localized higher plastic strain zones are marked in Fig. 17(a) by 'A', 'B' and 'C'. The restraining bends of the fault geometry make it difficult for the rupture to break through, causing stress concentration nearby. These localized zones of plastic strain have been observed by previous dynamic rupture studies performed on geometrically complex rough faults (Dunham et al., 2011c; Johri et al., 2014). Figure 17(b) shows the estimated receiver fault orientations using the direction of maximum plastic shear strain. The orientations vary between 0°-45° from the overall trace of the main fault. The receiver fault orientations are mostly within 20° of the main rupture trace. The dashed vertical line shows the sub-region from which the stress and plastic strain values are extracted for further static stress calculation.

Figure 18 shows the change in stresses (normal and shear) for the sub-region marked in Fig. 4. As can be seen in Fig. 18, the stresses are highly complex in the region near the fault. The geometric heterogeneity of the fault profile leads to this complexity in the stress distribution. Farther from the fault profile, the stress complexity is reduced as the fault roughness effects are not as prevalent at those distances. Furthermore, though the stresses are highly complex, we note from Fig. 18(b) that the negative shear stress change values dominate the positive values of stress change. Similar to our previous study (Aslam & Daub, 2018), we divide the region across the fault into three sub-regions based on the stress pattern. We refer the region close to the fault where the stresses are more complex as the the 'near-fault' region, while we refer the region of relatively uniform stresses as the 'far-fault' region. We refer the transition region between the near-fault region and the
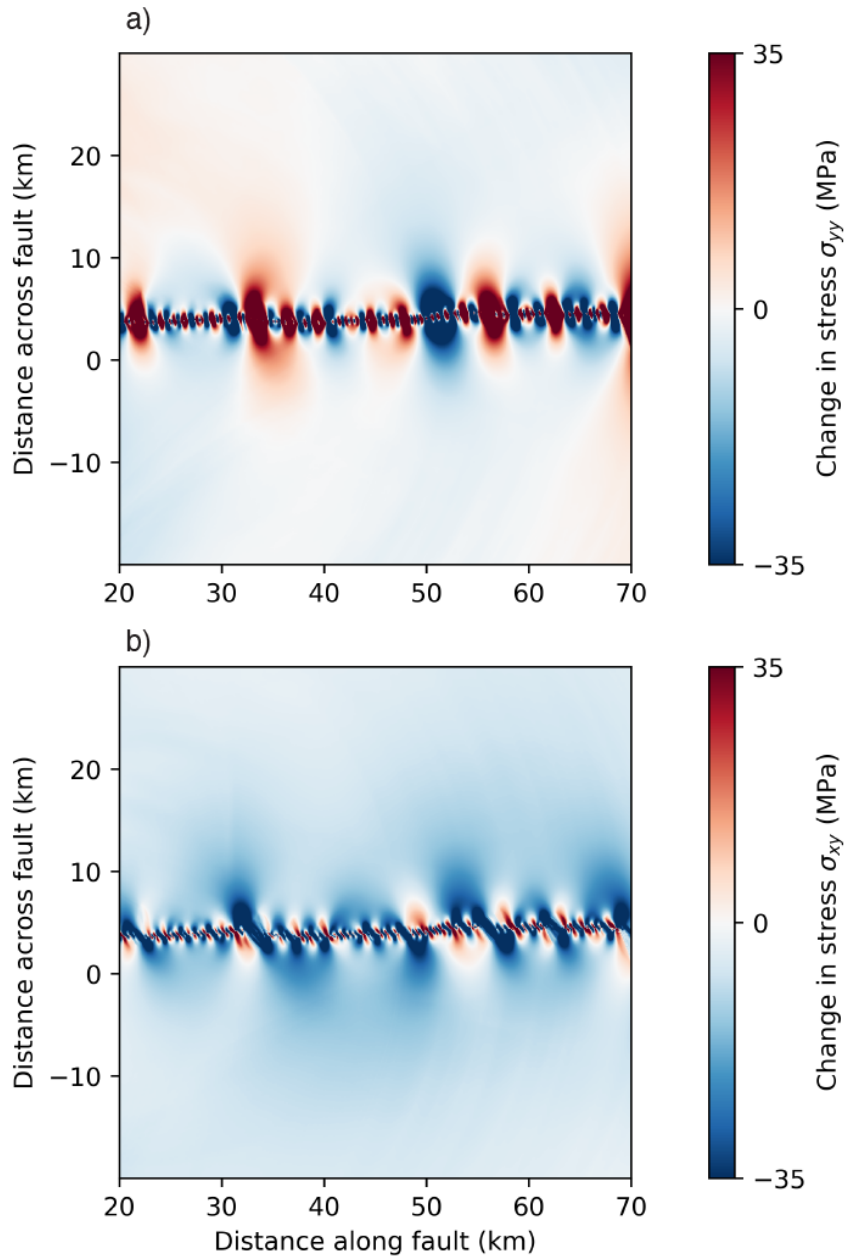
Fig. 18: Change in stresses in the sub-domain region of the modeling domain for the fault profile shown in Fig. 17. The simulation is run for a sufficient length of time ($= 41.3$ sec) such that there are no dynamic stresses related to the wave propagation and hence the stress change in the domain is present only due to static stress changes. a) Change in the normal stress in the modeling sub-domain. b) Change in the shear stress in the modeling sub-domain. The stress change in the near-fault region is highly complex, with most of the regions of the modeling sub-domain showing a decrease in the shear stress values.

far-fault region as the intermediate region. Most of our discussion of results in this study is related to the near-fault region since this region is mainly affected by the fault roughness during rupture propagation. We note that this naming convention is only for the purpose of discussing the results in this study; on tectonic scales, these regions are all close to the fault.

Using the final stress tensor from each of the rupture simulations, we calculate the CFF in the region surrounding the main fault. To calculate the CFF values, we use two different receiver fault orientation approaches. In the first approach, we assume parallel receiver fault orientations, while in the second approach, we calculate CFF values based on the receiver fault orientations calculated from the direction of maximum plastic shear strain. Since no plastic strain accumulates on the compressional side of the fault profile, we only calculate the CFF using the second approach for the extensional side of the fault. Figure 19 shows the CFF calculated using the parallel receiver fault orientation on both the compressional and extensional sides of the fault. Similar to the distribution of stresses shown in Fig. 18, the CFF distribution is also highly complex across the fault in the near-fault region with both negative and positive CFF change zones present in this region. At distances farther from the near-fault region, the CFF change pattern is more uniform, with negative CFF values dominating. Based on the realization shown in Fig. 19, there is not an obvious difference between the extensional and compressional sides of the fault. Therefore, we examine a statistical ensemble of all CFF values from both the extensional and compressional sides of the fault in addition to examining each side separately. The regions of positive CFF change in Fig. 19 are of particular importance, as these are the regions which are brought closer to failure and are potential locations of aftershocks. We note from Fig. 19 that the roughness of the fault profile causes many small positive CFF zones to occur within broader negative CFF zones. These small positive CFF zones are not resolvable using the usual CFF calculations due to coarser resolution of fault slip from the inversion studies, and hence these zones would appear as stress shadows. At far-fault
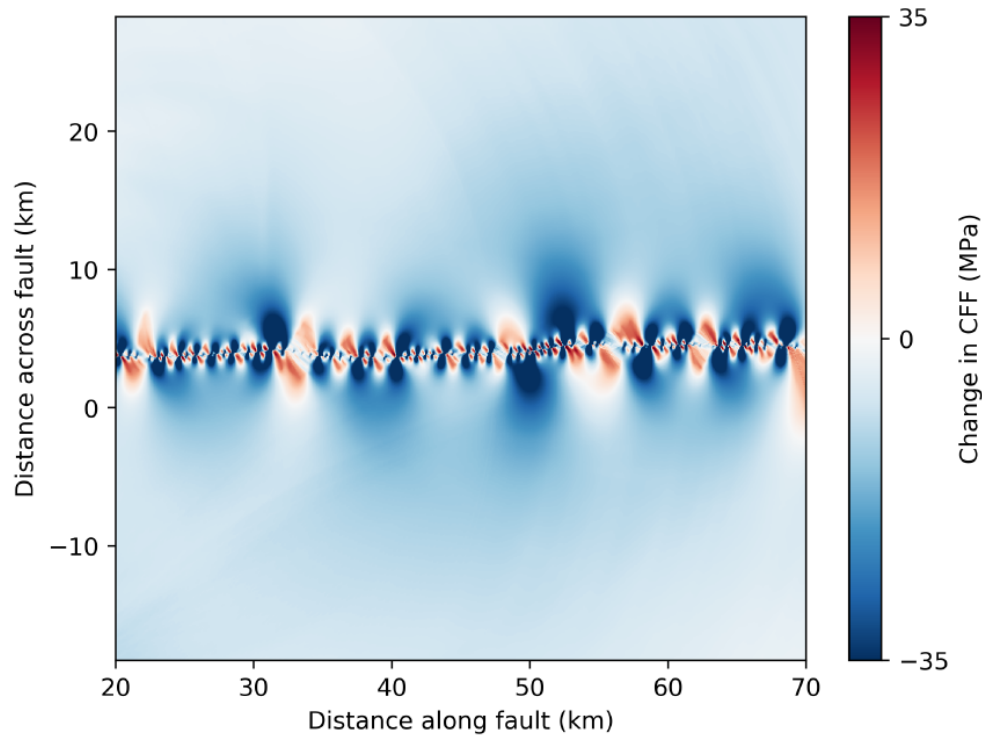
Fig. 19: The CFF change calculated in the sub-domain region of the simulation for the fault profile shown in Fig. 17. The CFF is calculated from the stress change values (both shear and normal stresses, shown in Fig. 18) as a result of dynamic earthquake slip on the rough fault. The calculations assume a frictional coefficient $\mu_\beta = 0.4$ and receiver fault orientations parallel to the mean host fault profile. The fault roughness of the fault profile results in a heterogeneous stress field within the rupture area of the main shock, resulting in an increased probability of occurrence of aftershocks within this area. Positive values of CFF change indicate that there is a higher probability of aftershock occurrence, while negative values of CFF change indicate regions of reduced probability of aftershocks. As can be seen, there is no obvious difference between the calculated CFF values in the extensional and compressional side of the fault. Note that the CFF values calculated here are based on events that ruptured unilaterally; however natural faults may not always rupture this way.

distances, where the fault roughness effects are not present, we do not see these positive CFF zones.

We mark the boundaries between the near-fault, intermediate, and far-fault regions based on the number of positive CFF zones. In this study, we consider a region to be a positive CFF zone if it has a length of at least 100 m (i.e. at least 4 consecutive positive CFF values along the direction of the receiver fault orientation). In each simulation, we first count the total number of positive CFF zones at each distance away from the trace of the main fault and then include distances with more than 8 positive CFF zones in the near-fault region. The distance at which the number of positive zones decreases from > 8 to ≤ 8 marks the boundary between the near-fault region and the intermediate region. The distance where no positive zones are observed designates the start of the far-fault region. We calculate the width of the near-fault region for both the compressional and the extensional side from each rupture simulation. The width of the near-fault region describes the distance over which the stress complexity as well as the damage pattern complexity may influence seismicity patterns. The average width of the near-fault region is 1890 m on the extensional side when CFF values are calculated using parallel receiver fault orientations, 2730 m when the CFF values are calculated using variable receiver fault orientations, and 1680 m on the compressional side of the fault.

We combine the CFF data from each side (both extensional and compressional) for all 187 rupture simulations to examine the statistical properties of the CFF as a function of distance. Figure 20 shows the PDF values of the CFF as a function of distance from the fault. Figure 20(a) shows the PDF of the CFF for the compressional side, Fig. 20(b) shows the PDF of the CFF for the extensional side, and Fig. 20(c) shows the PDF of the CFF by combining CFF values from the extensional and compressional side. It is important to note that Figs. 20(a), 20(b) and 20(c) are constructed using parallel receiver fault orientations. Figure 20(d) shows the PDF of the CFF as a function of distance on the extensional side where the CFF is calculated using variable receiver fault orientations. In each of the plots
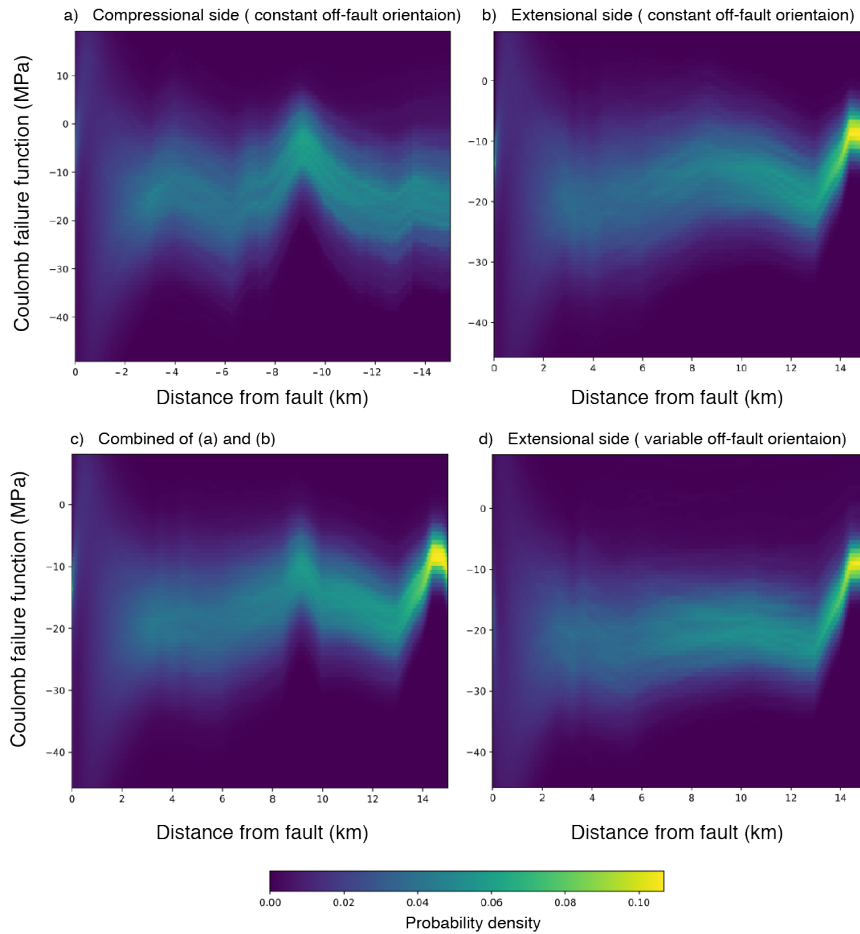
Fig. 20: The probability density function (PDF) of the change in CFF values as a function of distance away from the fault. The CFF values are highly variable at distances very close to the fault, and collapse into a relatively very narrow range at greater distances from the fault. This behavior is due to the fact that in the near-fault region, fault roughness effects cause the stress to be heterogeneous. In the intermediate/far-field region, where the fault roughness effects are weaker, the CFF value spread is relatively narrow when compared to the near-fault region. (a) PDF of CFF change for the compressional side with parallel receiver fault orientations. (b) Same as (a) but for the extensional side. (c) Same as (a) but based on the combined values of (a) and (b). (d) Same as (b) but with variable receiver fault orientations. The optimum orientations of the receiver faults predominantly change the CFF values at the extremes of the distribution at a given distance. This is the reason that the difference between (b) and (d) is not obvious from point statistics but stands out when the spatial correlations (Fig. 21 and Fig. 22) are considered.

in Fig. 20, the general behavior of the CFF values with distance from the fault remains the same. The regions close to the fault show a wider spread of CFF values, and as the distance from the fault increases, this spread gradually squeezes to a relatively narrow band of values. The distance at which we begin observing a narrow band of values of the CFF marks the transitional boundary between the near-fault region and the intermediate/far-fault region. The spread of the CFF values in the intermediate/far-fault region is not as narrow as is observed when running the same simulations with elastic off-fault properties (Aslam & Daub, 2018) (the figure showing the PDF of the CFF calculated assuming elastic off-fault response is provided in Fig. 6). This may be related to the fact that the off-fault stresses are smoothed when considering off-fault plasticity. Furthermore, we note from Fig. 20 that the range of values in the intermediate/far-fault region remains the same for simulations with elastic material properties but fluctuates between different upper and lower CFF bounds for the case of simulations with plastic off-fault material properties. When comparing the CFF values between the extensional side (Fig. 20(b) and 20(d)) and the compressional side (Fig. 20(a)) for the intermediate/far-fault region, we observe that the compressional side has more sharp fluctuations between different upper and lower CFF bounds, as no damage occurs on that side of the fault. In Fig. 20(d), the optimum orientations of the receiver faults change mainly the extreme CFF values with the largest and smallest CFF values. This is the reason that the difference between Fig. 20(b) and Fig. 20(d) is not obvious by eye. However, this change in the extreme values of the CFF does influence the locations of aftershocks, which we investigate through the spatial correlations of the CFF function.

Spatial correlations

All of our results described above are based on one point statistics from our simulations. Although one point statistics provide many useful insights into the static stresses, aftershocks are not point features, but spatially extended events that rupture an area that depends upon the magnitude of the aftershock. To study this, we extract

information related to the spatial correlations in the positive CFF values. To do this, we use the locations as well as lengths of positive CFF zones. To calculate the length of a positive CFF zone, we first pick a point at any distance away from the fault and then find the orientation of the receiver fault at that point ($0°$ for the case of parallel receiver fault orientations and a spatially-dependent value for the case of variable receiver fault orientations). We then calculate the CFF value at that point, if the CFF value is positive, we move 25 m further along the direction of the receiver fault orientation and calculate the CFF value at the next point. If this point is not on a grid point, we calculate its CFF value by interpolating the stress values at this point. We use linear interpolation (Barber et al., 1996) to compute the stress values at points which do not lie on the simulation grid. We continue along the same direction and increase the length of the positive zone until we encounter a negative CFF value. Figure 21 shows the total number of positive CFF zones in each rupture simulation at two different distances from the main fault on the extensional side of the fault. Figure 21(a) shows the number of positive CFF zones 100 m from the fault, while Fig. 21(b) shows the number of positive CFF zones 3.5 km from fault. We observe that the number of positive zones decreases as the distance from the fault increases. This is because at greater distances, the fault roughness effects are less prevalent, as is evident from Figs. 18 and 19. This behavior remains the same irrespective of the methodology used to calculate the positive CFF zones (i.e. either CFF calculated using a parallel receiver fault orientation or calculated using a variable receiver fault orientation). In the near-fault region, we observe twice the number of positive CFF zones for the variable off-fault orientations case when compared to the parallel receiver fault orientations (Fig. 21(b)). This is because when calculating CFF assuming variable receiver fault orientations, the directions that have minimum compressive normal stress and maximum shear stress are favored. This causes many more locations to have a positive CFF value than those found using a parallel receiver fault orientation. An increase in the number of positive CFF zones for the case of variable receiver fault orientations means an increase in

75
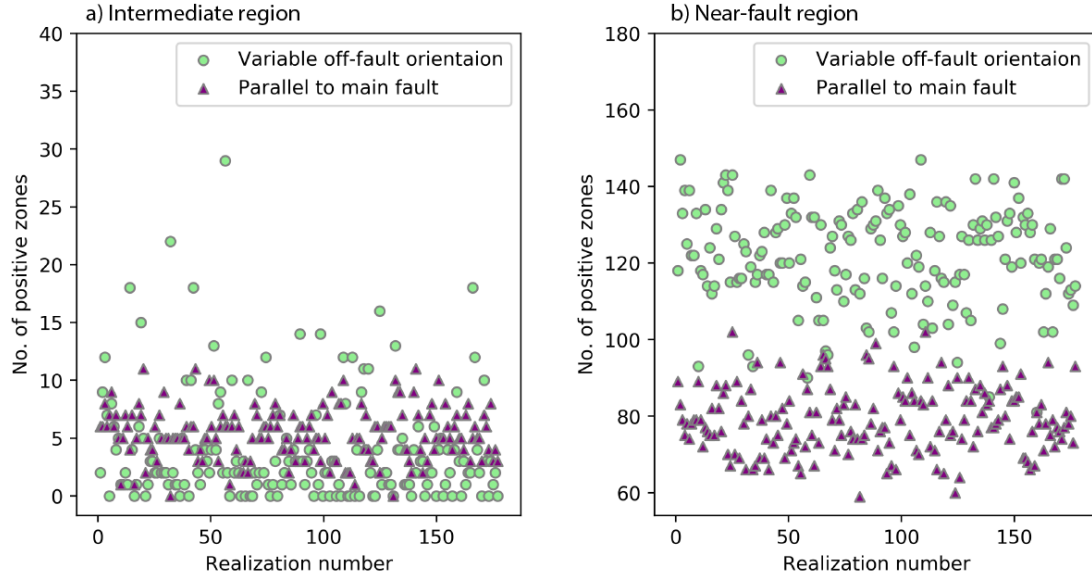
Fig. 21: Figure shows total number of positive CFF zones calculated from all rupture simulations for the near-fault region and the intermediate region. (a) Number of positive zones calculated at 3.5 km away from the main fault using variable receiver fault orientations (circles) as well as parallel fault orientations (triangles). (b) Same as (a) but for positive zones 100 m away from fault. The orientations derived from the damage zone are clearly well aligned with the stress field in the near-fault region, while they lead to a greater variability in the number of zones in the intermediate region.

the width of the near-fault region. This indicates that the fault roughness effects are observed at greater distances when off-fault material damage and dynamic calculations of receiver fault orientations are considered. The comparison between the number of positive CFF zones with the two types of receiver fault orientations suggests that the calculations of dynamic off-fault orientations are important at distances close to the fault since they can significantly affect the spatial location and magnitude of aftershocks. Furthermore, comparing Figs. 21(a) and 21(b), we can see that the orientations derived from the damage zone are clearly well aligned with the stress field in the near-fault region, and they lead to a greater variability in the number of zones in the intermediate region.

Since we have calculated the locations and rupture lengths of the positive CFF zones surrounding the main fault in each simulation, we can combine this information from each simulation to examine the spatial characteristics of probable aftershock zones

76

surrounding a complex fault. To estimate the maximum possible magnitude of each of the calculated positive zones, we assume that each patch hosts a circular patch rupture and convert that area into a magnitude using standard scaling relations. Figure 22 shows the plot of joint PDF of rupture areas as a function of distance for all probable aftershock zones. The plot combines all the positive CFF zone data from each simulation. The plots shows both smaller rupture zones with small rupture areas (< 2.5 km^2) and larger rupture zones with larger rupture areas (> 2.5 km^2) are present at all distances from the fault. The smaller rupture zones have a higher probability of occurrence at distances closer to the near-fault region than the larger rupture zones. This behavior is observed independent of the choice of receiver fault orientation. For distances within the intermediate zone, we observe smaller and larger rupture zones to have a similar probability of occurrence. This behavior remains the same for calculations using both parallel and variable receiver fault orientations. When comparing Figs. 22(a) and 22(b), we see that the higher probabilities for smaller rupture zones in the near-fault region are more uniformly distributed with distance when calculated using variable off-fault orientations as compared to rupture zones calculated using parallel receiver fault orientations. This is due to the fact that there are a higher number of smaller zones calculated using variable off-fault orientations than for the case of parallel fault orientations. We observe no larger ruptures (with rupture areas > 1 km^2) for distances less than 200 m in Fig. 22(a) when compared to Fig. 22(b), and fewer smaller ruptures (with rupture area < 0.1 km^2) for distances greater than 4 km. Figure 22(b) is more complete in terms of probable rupture areas (fewer white spaces with PDF value = 0) because we observe many more rupture zones with a range of areas calculated using variable receiver fault orientations. These rupture zones are distributed throughout the near-fault and intermediate regions surrounding the main fault and fill in the empty portions of Fig. 22(b). Since the region closer to the fault is highly damaged (Faulkner et al., 2011), and the stresses in this region are complex (Erlingsson & Einarsson, 1989;

77

Aslam & Daub, 2018; Pedersen et al., 2003), we expect real aftershocks to have a range of rupture lengths giving rise to behavior that is similar to what we observe in Fig. 22(b).

Our modeling suggests a greater probability of occurrence of smaller area rupture zones in the near-fault region as compared to the intermediate region. There may also be a correlation between positive CFF zone areas and the mean amplitude of stress increase. To examine this, we calculate the mean CFF amplitude for each rupture zone. Figure 23 shows the amplitude of CFF as a function of rupture area from all of our simulations. Figures 23(a)-(c) show rupture zones calculated using parallel receiver fault orientations while Figs. 23(d)-(f) are based on calculations using variable receiver fault orientations. It is evident in Figs. 23(a) and 23(d) that the mean CFF amplitude decays with distance and with increasing zone area. Similarly, it can be clearly observed from Figs. 23(c) and 23(f) that the rupture zones are mostly smaller in the near-fault region and have higher CFF amplitudes, while the CFF amplitudes are smaller at intermediate distances for both smaller and larger zones (Figs. 23(b) and 23(e)). Based on the comparison of CFF amplitudes in the near-fault region (Figs. 23(c) and 23(f)), we find that the CFF amplitudes calculated using variable receiver off-fault orientations are relatively low when compared to CFF amplitudes calculated using parallel off-fault receiver orientations. Similarly, the CFF amplitudes have a greater spread in Fig. 23(c) as compared to Fig. 23(f). This is because the optimum orientations of the receiver fault tend to smooth the CFF values, which increases the connectivity between positive zones, as plastic deformation tends to remove extreme stress values from the distribution.

Real data comparison

To compare our modeling results with real observations, we compile a dataset by considering aftershocks from five major earthquakes in California. Figure 24(a) shows the trace of the rupture of 1999 Hector Mine earthquake. The induced CFF change in the surrounding region due to this earthquake, at the focal depth of 7.5 km, is calculated and plotted in Fig. 24(a). The CFF change is calculated using the slip model of Salichon et al.
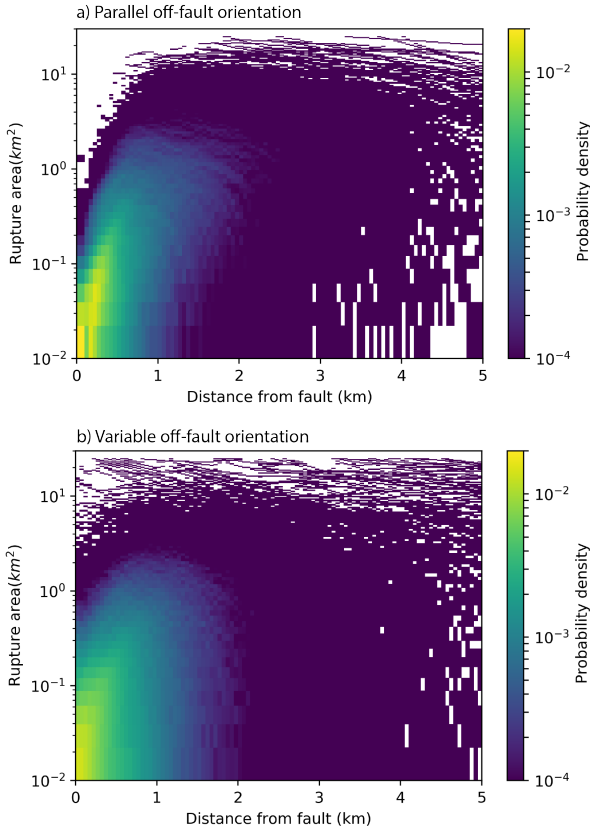
Fig. 22: Areas of positive CFF zones versus distance from the fault. (a) Rupture areas calculated using parallel off-fault orientations. (b) Same as (a), but rupture areas are calculated using variable receiver fault orientations. The color scale in both (a) and (b) represents the joint PDF values of positive CFF area and distance. Our modeling results show that smaller zones are more probable close to the fault than large zones (both in (a) and (b)). This is because the stresses are more heterogeneous near the fault, leading to shorter correlation lengths and smaller zones. The larger rupture zones occur less frequently in the near-fault region as compared to the smaller zones. In the intermediate region, both smaller and larger rupture areas have equal probability of occurrence. Since a real aftershock does not always fill an entire positive CFF region, we expect many aftershocks with smaller rupture areas may be present at intermediate distances. Furthermore, (b) is more complete in terms of probable rupture areas (fewer white spaces with PDF value = 0). This is because the optimal orientations of the receiver fault result in many more positive zones with variable lengths (Fig. 21), which fill in most of the empty spaces observed in (a).
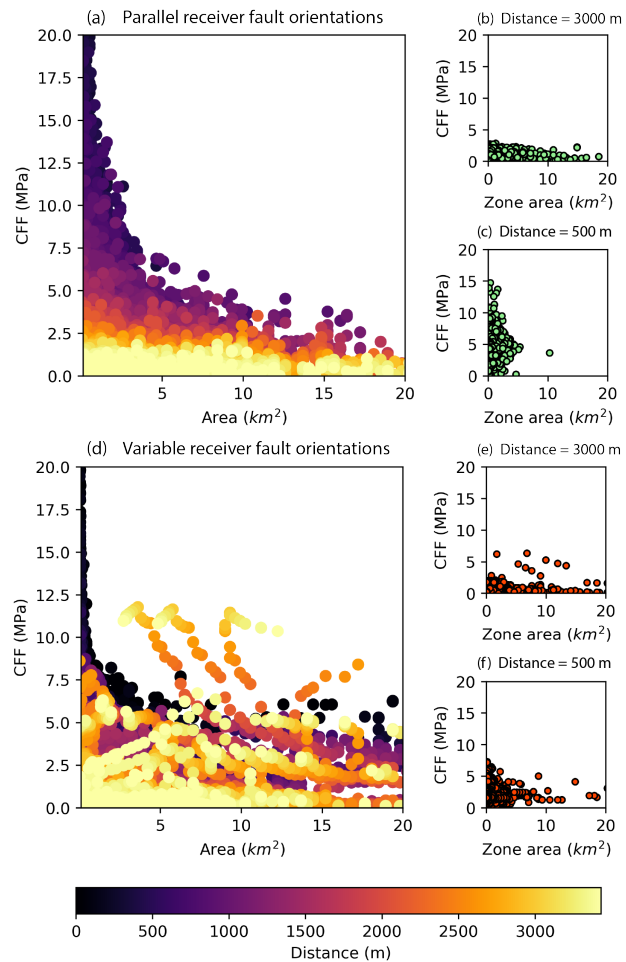
Fig. 23: The plot shows the amplitude of CFF increase as a function of the zone area. (a) Rupture zone areas calculated using fault parallel receiver fault orientations, (d) Rupture zone areas calculated using variable receiver fault orientations. The color scale in both (a) and (d) represents the distance of each positive zone from the fault. (b) The amplitude of CFF increase as a function of the zone area calculated using similar receiver fault orientations for a distance of 3000 m away from fault. (c) The amplitude of CFF increase as a function of the zone area calculated using fault parallel receiver fault orientations for a distance of 500 m away from fault. (e) Same as (b), but the amplitude of CFF increase is calculated using variable receiver fault orientations. (f) Same as (c), but the amplitude of CFF increase as a function of the zone area is calculated using variable receiver fault orientations. As can be seen in (d), (e) and (f), the optimum orientations of the receiver fault tend to smooth the stress field, giving less extreme CFF values but increased connectivity between different positive zones.

80

(2004). We can observe a prominent stress shadow in the center of the fault with two positive CFF zones around the fault in the near-fault region. Figure 24(b) shows the magnitude-frequency distribution of all the aftershocks from the compiled dataset. We note that the magnitudes of the aftershocks follow the Gutenberg-Richter magnitude-frequency (GR) distribution (Gutenberg & Richter, 1944). To construct Fig. 24(b), we only pick those aftershocks that are located in regions within 5 km from the fault rupture to compare them with our model results. Note that these aftershocks may include secondary triggered aftershocks (Meier et al., 2014). To determine how the rupture areas of these aftershocks depend on distance, we calculate the joint PDF values of the rupture areas and distances from the fault for the aftershocks of five major earthquakes. It is important to note that Fig. 24(c) shows the same information as Fig. 22, but it illustrates the joint PDF for aftershocks rather than the positive CFF zone areas from our models. The data shown in in Fig. 24(c) presents similar behavior to what is observed from our modeling results. We observe rupture zones with both smaller rupture areas (< 0.45 km^2) and larger rupture areas (≥ 0.45 km^2) present in both the near-fault and intermediate regions. Similar to our modeling results, the smaller rupture areas are relatively more probable than the larger rupture areas in the near-fault region. In the intermediate region, we observe a relatively higher probability of smaller rupture areas when compared to the larger rupture areas. Since our model does not add any constraints on the existence of smaller size events within the larger CFF zone, the additional events with small rupture areas at all distances in the observations are likely due to events that do not fill the entire positive CFF zone. Note that the spatial characteristics of aftershocks (Fig. 24(c)) may also be affected by stress heterogeneities due to previous events and pore-pressure fluids. We do not model those effects, as they are difficult to quantify in the earth; however, we suggest that our model results are broadly consistent with the spatial characteristics of aftershocks data. Furthermore, a comparison of the histograms of aftershock distances (i.e. distance between the fault rupture plane and aftershock's epicenter) for $M_w > 2$ and $M_w > 3$ in Fig. 24(d)

shows that the aftershocks follow a GR distribution at all distances ($M_w > 2$ are an order of magnitude more frequent than magnitude $M_w > 3$). Based on our model results, we suggest that this arises possibly due to the roughness of the fault which produces positive CFF change zones of a variety of different areas at all distances in the near-fault region. Hence, these positive CFF zones are likely to host some smaller events, resulting in the GR distribution at all distances.
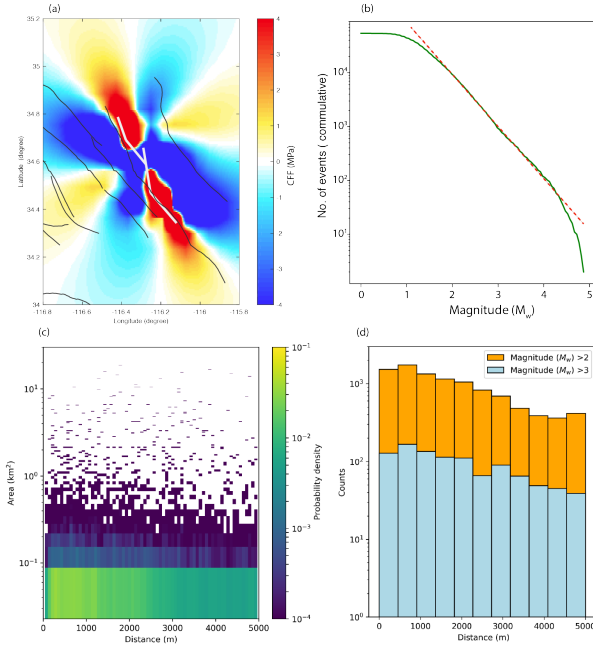
Fig. 24: (a) The CFF calculated for the 1999 Hector Mine earthquake at 7.5 km focal depth, on the optimum orientations of strike slip receiver faults. We observe two positive CFF change zones while a siginificant part of the near-fault region is dominated by a stress shadow. The white line shows the surface fault trace (Salichon et al., 2004). The black lines marks the trace of the known active faults present in the region. (b) The magnitude frequency distribution of the compiled dataset of aftershocks from five large earthquakes from the California region. These earthquakes include the 1984 Morgan Hill earthquake, the 1989 Loma Prieta earthquake, the 1992 Landers earthquake, the 1994 Northridge earthquake, and the 1999 Hector Mine earthquake. The magnitude frequency distribution follows the Gutenberg-Richter distribution. (c) Rupture areas and distance distribution for all the aftershocks occurring within 5 km from the main fault. The dataset is complied from 5 large earthquakes of California described in (b). (d) A comparison of histograms of aftershock distances from the fault plane for two different magnitude ranges for aftershock data shown in (b). The aftershocks follow the GR distribution at all distances from the fault with an order of magnitude more aftershocks with $M_w > 2$ than aftershocks with $M_w > 3$. Based on our model results, we suggest that this arises due to the roughness of the fault which produces positive CFF change zones of a variety of different lengths at all distances in the near-fault region.

Discussion

In this work, we perform dynamic rupture simulations with off-fault plasticity on rough strike slip faults to investigate the occurrence of aftershocks in the near-fault region and in the region of stress shadows (Segou & Parsons, 2014; Kilb et al., 1997; Beroza & Zoback, 1993). We perform rupture simulations on many realization of a self-similar rough fault profile with RMS height of 0.01. We calculate the CFF values on the extensional side using variable and parallel receiver fault orientations. We use plastic strain accumulation (Templeton & Rice, 2008; Ben-Zion & Shi, 2005; Andrews, 2005) to calculate the variable orientations of receiver faults. The pattern of static stress change is highly complex (Chester & Chester, 2000; Dieterich & Smith, 2009) in the near-fault region irrespective of which approach is used to calculate the CFF value. Similarly, our calculations suggest that the PDF of the CFF distribution follows a pattern where a large spread of the CFF values occurs in the near-fault region and collapses to a narrow CFF spread at intermediate and far-fault distances. This behavior is expected since static stress changes decay inversely with the squared distance from the main fault (Powers & Jordan, 2010; Hauksson, 2010; Smith & Dieterich, 2010).

We extract the spatial correlation characteristics of the positive CFF values from our model results. In particular, we are interested in the spatial extent of positive CFF zones since these are potential locations of future aftershocks. We find many small positive CFF zones to be present within larger negative CFF zones. These smaller positive CFF zones which are not resolvable using the usual CFF calculations would appear as stress shadows in observational studies (Freed, 2005; Segou & Parsons, 2014). Our calculations show that, in the near-fault region, the positive CFF zones are twice as probable in the near-fault region when CFF values are calculated using variable off-fault orientations in comparison to CFF values calculated using parallel receiver fault orientations. An increase in the number of positive CFF zones causes an increase in the width of the near-fault region for the case of variable receiver fault orientations. This suggests that off-fault

material damage tends to affect the spatial characteristics and decay of aftershocks with distance. Furthermore, if many more positive zones at close distances are present within a certain region, there is a higher probability that the rupture on these small zones can propagate through the zone of negative CFF values between them and grow into a larger rupture. This suggests that the off-fault damage (Chester & Logan, 1986; Myers & Aydin, 2004; Faulkner et al., 2011; Chester et al., 1993, 2004; Biegel & Sammis, 2004; Caine et al., 1996) is important along with the observed stress complexity of the fault system (Erlingsson & Einarsson, 1989; Pedersen et al., 2003) in order to determine the locations and magnitudes of aftershocks in a particular region.

Most of the aftershocks occur in the immediate vicinity of a large fault (King et al., 1994; Stein et al., 1994; Freed, 2005; Liu et al., 2003). The material in this region is much weaker than the adjacent country rock (Faulkner et al., 2003; Cochran et al., 2009; Hauksson, 2011, 2010). The weaker zone is due to the complex damage in the near-fault region that has been observed by many observational studies (Faulkner et al., 2010, 2011; Myers & Aydin, 2004; Andrews, 2004, 2005; Rice et al., 2005). This highly damaged weak zone influences the spatial seismicity distribution (Hauksson, 2011, 2010). Some studies (e.g. (Liu et al., 2003; Powers & Jordan, 2010)) were carried out to estimate the size of the damage zone surrounding a large fault using aftershock data. In this study, we examine if the decay of seismicity with distance from the fault is controlled only by the stress field decay or if the damage zone also influences the decay of seismicity. Our comparison of amplitudes of CFF as a function of areas and distances (Fig. 23) suggests that both the stress field decay and the damage zone complexity affect the decay of seismicity with distance. The stress field fluctuations decay with distance, but the damage zone plays a role by aligning fault orientations with the optimal stress orientations for failure. This is particularly obvious from the outlier values seen in Figs. 23 (d) and (e), which do not follow the usual trend of the amplitude as a function of distance seen in Fig. 23(a),

suggesting that the damage zone complexity cannot be neglected when examining seismicity patterns near active faults.

Many quasi-static modeling studies have examined static stress changes and the consequent aftershock distribution in the near-fault region as a result of slip on rough faults. Shaw et al. (2015) considered a multi-strand fault system to run their quasi-static model and found that the reduced ground motion amplitudes of aftershocks occurred in the near-fault regions are predominantly due to smaller stress drop of these events. Their model was able to capture many of the characteristics of spatial and temporal clustering of aftershocks. Smith & Dieterich (2010) also considered a rough fault to perform quasi-static modeling and showed the occurrence of aftershocks in small positive CFF zones within stress shadows. Powers & Jordan (2010) used the quasi-static model of Dieterich & Smith (2009) to constrain the width of the near-fault region for different faults in California. Though the quasi-static models of fault slip on rough faults were able to explain some of the important characteristics of aftershock distribution, these calculations were solely based on stresses since these models lack any physical representation of likely orientations of receiver faults in the damage zone. Our results suggest that using the orientation of maximum plastic shear strain as a proxy for possible aftershock fault planes allow more positive CFF zones than the simple fault-parallel orientations in the near-fault region. Our dynamic earthquake rupture simulation study can provide constraints on the characteristics of damage zone that may be included into the quasi-static models to get improved estimates of the spatial distribution of aftershocks in a self-consistent manner.

A focal mechanism solution provides the information of slip direction and fault-plane orientation of an earthquake through its radiation pattern (Hardebeck & Shearer, 2002). This information is then used to derive the orientation of stresses causing the earthquake (e.g. (Mallman & Parsons, 2008; Hardebeck, 2015; Beroza & Zoback, 1993; Hardebeck, 2010). In many cases, the focal mechanisms are diverse in the near-fault region (Beroza & Zoback, 1993; Bailey et al., 2010; Smith & Heaton, 2011) and do not align,

suggesting a complete stress drop in order to produce the variable orientations of aftershocks. This was the case for orientations observed by Kilb et al. (1997) from earthquakes following the 1989 Loma Prieta earthquake. However, some studies show good alignment of focal mechanisms of aftershocks with the mainshock (Michele et al., 2016). We see that our receiver fault orientations are predominantly within the "acceptable" range of the Kilb et al. (1997) study, suggesting that the dynamic rupture studies can be used to infer the likely orientations of receiver faults in the damage zone. Furthermore, our simulations show heterogeneous orientations of receiver faults very close to the main fault which may suggest that the diverse aftershock mechanisms observed near the fault for the case of 1989 Loma Prieta earthquake were caused by co-seismic off-fault deformation (expressed as microcracking and secondary faulting).

All of our simulations are performed in 2D. A real earthquake does not occur in 2D but rather occurs in 3D on a 2D fault. In 3D ruptures, the process of rupture propagation may change if the rupture in the third direction is not coherent (Dunham et al., 2011c; Shi & Day, 2013). This may also cause some differences in the pattern of stress change in the off-fault region. Furthermore, we use the plastic strain accumulation during rupture propagation to calculate receiver fault orientations. This approach only accounts for the faults that are created during the dynamic rupture events. This may not always be the case as the receiver faults may also be pre-existing and have an orientation that is unrelated to the present tectonic behavior (Toda et al., 2008; Lin & Stein, 2004; Toda et al., 2005; Tse & Rice, 1986; Rice, 1993; Nielsen & Knopoff, 1998; Hainzl et al., 2010; Lapusta et al., 2000; Duan & Oglesby, 2005b; Oglesby & Mai, 2012). However, if such knowledge is available from, for instance, geological mapping studies, it can easily be included in the present methodology.

We calculate the CFF values in the off-fault medium as a result of rupture on fractal faults. The real faults may show non-fractal large-scale geometrical complexities like macro-scale fault bends and step-overs. These large-scale geometrical complexities play

major role in controlling the rupture propagation characteristics (Ulrich et al., 2019; Kyriakopoulos et al., 2019). The regions of large-scale geometrical complexities are observed as regions of pronounced off-fault deformation during an earthquake rupture (Milliner et al., 2015). Our rupture simulations suggest that the stresses concentrate around the fault bends during rupture propagation causing plastic deformation to be highly pronounced (as seen at location A,B,C in Fig. 17) in regions of high geometrical heterogeneity. These regions of pronounced plastic deformation has a higher probability of occurrence of aftershocks since the structures are more likely to be optimally oriented in this region.

Slip inversion studies of some large earthquakes (e.g. the 1999 Izmit earthquake of magnitude 7.5, the 2010 El-Mayor Cucapah earthquake of 7.2, the 1992 Landers earthquake of 7.3) have shown that the co-seismic slip decrease from depth towards the surface of earth (Gonzalez-Ortega et al., 2014; Simons et al., 2002; Fialko, 2004). This deficit of co-seismic slip at shallower depths is usually termed as shallow slip deficit (SSD). Some studies have suggested the inelastic deformation during co-seismic deformation as a potential explanation of the SSD. Kaneko & Fialko (2011) performed a 2D dynamic earthquake rupture simulation of a depth dependent model to investigate the presence of SSD. They performed their simulations with homogeneous structural properties of subsurface layers. Roten et al. (2017) also performed dynamic rupture simulation in 3D to investigate the presence of the SSD but they used SCEC community velocity model (CVM) with a low velocity layer to represent the sub-surface structural properties. Both studies showed that the SSD observed during the slip of large earthquakes, can be explained by shallow inelastic deformation. The degree to which plastic deformation occurs near the surface is proportional to the amount of the slip deficit. The plastic deformation at shallow depths broadens, making a flower like structure that distributes the deformation over a broad region near the surface. This flower structure has also been observed in other dynamic rupture studies (Ma & Andrews, 2010). Our study suggests that broadening of
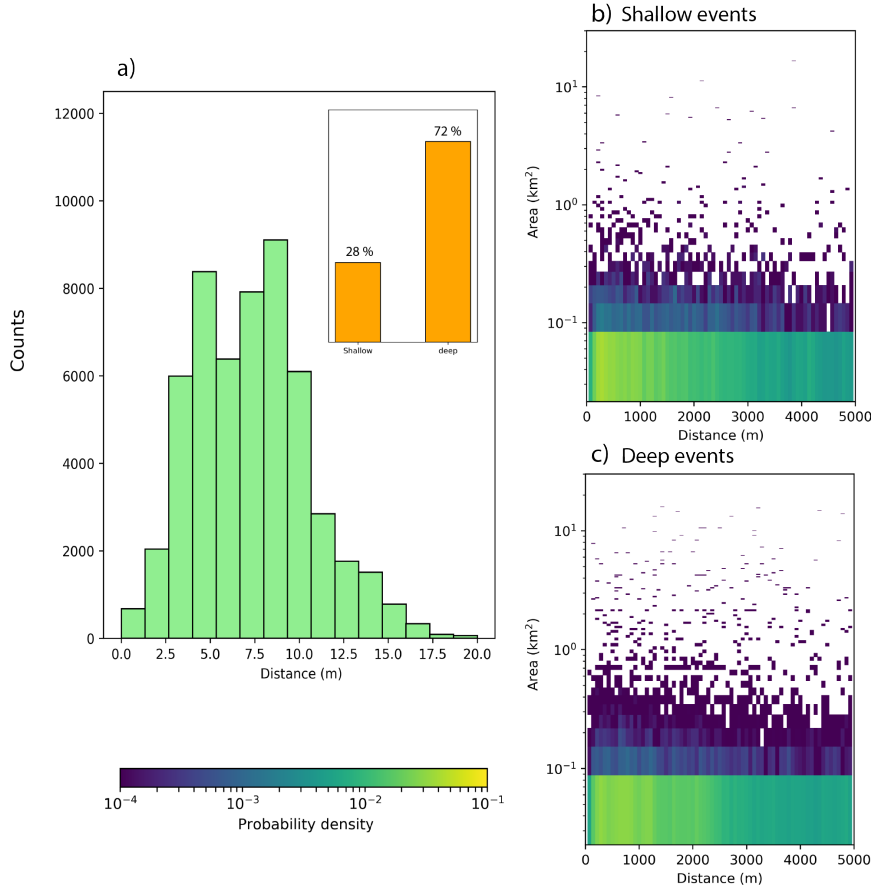
Fig. 25: (a) Histograms of depths for all aftershocks from our compiled dataset of five large earthquakes from the California region, shown in Fig. 11(b). Most of the aftershocks occur at depth between $7.5 - 10$ km. The inset shows the percentage of occurrence of shallow and deep events. Note that shallow events are those, which occurred at a depth of 5 km or less, while deep events are those, which occurred at depth of greater than 5 km. We select 5 km level to separate shallow and deep events, since it is the maximum depth till where widening of zone of plastic deformation was observed by previous studies. (b) Rupture areas and distance distribution for all the shallower events. (c) Rupture areas and distance distribution for all the deeper events. When comparing (b) and (c), we do not find any obvious difference between rupture areas and distance distribution of shallower and deeper events.

89

plastic deformation increases the extent of the near-fault region, which means that the width of aftershock zone is greater for shallower events than deeper events. However, the rupture areas of shallower aftershocks (depth $\leq$ 5 km, comprising $\sim 28\%$ of the aftershocks data) do not show any obvious difference to rupture areas of deeper aftershocks (depth $>$ 5 km, comprising $\sim 72\%$ of the aftershocks data), when compared as a function of distance (Fig. 25). A possible explanation could be that the damage zone gets wider at shallower depths, but due to weak stress changes due to lower slip at those depths, the effects essentially cancel out. However, a further investigation is required to make some quantitative predictions to evaluate which effects might be strongest, which is a topic for further research.

Our model suggests a higher probability of smaller rupture zones in the near-fault region as compared to larger rupture zones. This behavior is similar to the aftershock data which suggests a higher probability of smaller rupture zones in the near-fault region as compared to the larger rupture areas. One effect that we do not include is the secondary triggering caused by aftershocks (Helmstetter et al., 2005; Kagan, 1994; Hanks, 1992; Marsan, 2005; Meier et al., 2014) after one major earthquake causing the static stresses to redistribute. Our model does not capture this effect, though the secondary triggering methodology could be combined with our approach. The static stress changes can also cause pore-pressure variations if the medium is saturated with fluids. This process can affect the aftershock distribution of a region in space (Chen et al., 2012; Gupta, 2002; El Hariri et al., 2010; Nur & Booker, 1972) and time (Freed, 2005; El Hariri et al., 2010; Chen et al., 2012). The aseismic slip of a fault also has the tendency to change the static stresses induced due to the co-seismic slip on the fault (Vidale et al., 2006; Vidale & Shearer, 2006). Constraining the role of each of these mechanisms described above is difficult (Waite & Smith, 2002; Hainzl, 2004; Vidale & Shearer, 2006; Lohman & McGuire, 2007), and it is not clear if these mechanisms may work together in a certain region to change static stresses or a single mechanism may dominate over the other mechanisms.

Table 4: List of few dynamic rupture properties

Parameter name	Symbol used	Value	Expression taken from
S ratio	S_{ratio}	1.2	(Templeton & Rice, 2008)
Cohesive zone length	R_0	252 m	(Templeton & Rice, 2008)
Mean stress drop	$\Delta\tau$	28.0 MPa	

Furthermore, other factors like topography of a region, heat flow and crustal thickness, V_p/V_s ratio of a region (Hauksson, 2011), and material contrasts (Rubin & Gillard, 2000; Rubin & Ampuero, 2007) across a major fault have also been observed to change the static stresses of those regions causing variations in the distribution of aftershocks. We do not model any of these phenomena in our calculations, while the observational data may include effects from these mechanisms. Overall, our findings from this modeling study are consistent with the general behavior observed in the spatial seismicity patterns. This may suggest that the supplementary mechanisms (mentioned above) are more important to include in the models when more emphasis is given to the temporal behavior of aftershocks, rather than their spatial location.

Based on our modeling results, we suggest that the damage zone is an important factor for estimating the future hazard and risk estimates of a particular region. This is because the damage zone controls the decay of aftershocks with distance together with the stress field decay with distance. A modification to the classical Coulomb failure function which considers the damage state of the near-fault region may provide a better fit to spatial aftershock distribution observed for large earthquakes as compared to classical static stress calculations. Our results suggest that knowledge of the damage zone and the likely orientations of receiver faults from physical models can provide improved constraints on the spatial distributions and magnitude of aftershock occurrence. Such methods may help improve forecasting of off-fault seismicity and improve estimates of seismic hazard in a variety of tectonic contexts.

Chapter 4

Modeling damage evolution in the inter-seismic phase as a result of rupture on complex faults

Abstract

We model the co-seismic and the inter-seismic phases of an earthquake by coupling a dynamic rupture model with a long-term tectonic model (LTM). We do this to investigate how induced static stress changes during the co-seismic phase of an earthquake influence the dynamics of strain accumulation during the inter-seismic phase. We perform dynamic rupture simulations on complex strike slip faults in 2D, incorporating off-fault plastic failure and strong dynamic weakening on the fault governed by the slip weakening law. Our strike slip fault has a self-similar fractal profile with RMS height taken from observational studies. Our dynamic rupture simulation results show that the stresses in the region surrounding the fault are highly complex and heterogeneous. We extract these complex stresses together with the plastic deformation from the dynamic model and use them as input to run the LTM. We run the LTM for a time duration of an earthquake cycle. Our LTM results show that most of the shear zones (i.e. zones accumulating plastic strain) develop and grow at oblique angles to the main fault while considerable amount of damage keeps accumulating along the immediate sides of the fault profile. The development and growth of these new features occurs in the locations where geometrical bends in the fault profile have caused the deformation in the dynamic phase to be localized. This localized deformation due to fault roughness acts as a seed for the development of new features. We conclude that the observed complex damage pattern in natural fault zones is mainly due to the fault surface roughness effects. During the co-seismic phase, the stresses concentrate near the fault bends due to the rough fault profile. During the inter-seismic phase, these locations are favored for the development of new shear features, as further tectonic loading pushes these locations towards failure.

Introduction

The long-term evolution of geological systems by numerical simulations is referred to as long-term tectonic modeling (LTM) (Choi et al., 2013). LTM modeling generally follows two types of motivations. The first motivation is based on geological observational studies. In this type of model, geological observational studies such as regional mapping studies (Bartholomew, 1987; Bartholomew et al., 1981; Whitaker & Bartholomew, 1999; Schultz & Bartholomew, 2009; Schultz, 1988), outcrop-scale studies (Gray, 1981; Simon & Gray, 1982; Bartholomew et al., 2010; Whitaker & Bartholomew, 1999; Spraggins, 1999), or fault damage zone studies ((Chester & Logan, 1986; Chester et al., 1993, 2004; Biegel & Sammis, 2004; Caine et al., 1996) observe complex geological features in a certain tectonic setting and then LTM models attempt to replicate those geological observations using a numerical approach. This type of LTM study is done to investigate the physical processes that occur within the geological system that lead to the development of such features. The second motivation focuses on understanding the dynamics of a certain geological system under a certain set of initial conditions rather trying to replicate a specific observation (Hobbs et al., 2009, 2008; Regenauer-Lieb & Yuen, 2003; Ahamed, 2018). The purpose of this type of LTM approach is to get an improved understanding of the behavior of the geological system under complex but more realistic initial conditions.

Our study is based on the second type of LTM approach. We investigate the evolution of the damage pattern in the near-fault region in response to the stresses imposed as a result of earthquake rupture on a complex fault. We do this by coupling the LTM model with a short term dynamic earthquake rupture model. We run the short term simulation of dynamic rupture (i.e. co-seismic phase of an earthquake) on a rough fault with off-fault inelastic deformation governed by continuum plasticity (Andrews, 2005; Dunham et al., 2011*c*,*a*; Shi & Day, 2013; Gabriel et al., 2013). This results in a complex stress, strain and damage pattern in the near-fault region. We then run LTM model with initial conditions of stress, strain and damage taken from the dynamic model and

investigate the behavior of strain accumulation and subsequent damage formation in the near-fault zone during the inter-seismic phase of that earthquake.

Dynamic rupture models are a common tool for exploring the basic physics of earthquake rupture (Aochi et al., 2000; Harris, 2004; Bizzarri & Cocco, 2005; Dalguer et al., 2003; Daub & Carlson, 2008, 2010; Shi & Day, 2013; Harris & Day, 1997; Dunham & Archuleta, 2005; Tinti, Bizzarri & Cocco, 2005; Shi & Ben-Zion, 2006; Aslam & Daub, 2018). Most of dynamic rupture studies are performed on planar flat faults (Okubo, 1989; Dieterich, 1992; Kato & Seno, 2003; Lapusta et al., 2000; Lapusta & Rice, 2003; Dunham et al., 2011b). Since natural faults are not flat but rather exhibit a fractal profile, some more recent studies also include the non-planner geometries of fault (Duan & Oglesby, 2005b,a; Zhang et al., 2006, 2004) and the fault roughness (Dunham et al., 2011d; Shi & Day, 2013) to understand the effect of complexity of fault geometry on rupture characteristics. Our study also performs dynamic rupture simulations on rough faults rather than planar faults with off-fault plasticity to account for the damage in the near-fault zone.

Dynamic rupture simulation studies typically follow the approach of only simulating the co-seismic phase of an earthquake. Some dynamic rupture simulation studies also performed multi-cycle/full-cycle earthquake simulation, where the interseismic phase is modeled using different methodologies. Zhang et al. (2004, 2006) modeled the interseismic loading by imposing a uniform slip rate on the bottom of the fault in order to understand earthquake nucleation on a dip slip fault. Ahamed (2018) performed a LTM simulation to get the long-term stresses in the modeling domain and then used these stresses to provide the tractions on a dip slip fault to run a dynamic rupture simulation. Duan & Oglesby (2005b) used a visco-elastic model to include the inter-seismic phase of earthquake cycle. They simulated multi-cycle earthquake on a strike slip fault with a bend in its geometry so that they could investigate how fault geometry (i.e. the fault bend) influences the normal stresses in the vicinity of the bend. In our study, we perform a full earthquake cycle

simulation by coupling dynamic rupture model and LTM model to investigate how the static stress changes and plastic deformation after a spontaneous earthquake rupture simulation affects the evolution of damage pattern in the near-fault region during the loading phase of the next earthquake.

The description of our coupled model is as follows: we perform two dimensional (2D) spontaneous earthquake rupture simulations on rough strike slip faults using off-fault plasticity. Our simulations then consider the post-seismic dynamics of off-fault deformation, transitioning into the full inter-seismic period using long-term tectonic model (LTM). The fault is pre-existing in the dynamic rupture model and the resulting stress and strain fields from this model are input to the LTM simulation. The process of co-seismic fault failure during rupture propagation is governed by the slip weakening friction (SW) law. For the dynamic rupture simulation, we consider the fault to be an self-affine fractal. The off-fault material inelasticity during rupture propagation and LTM is governed by continuum plasticity.

Fault roughness and its parameters

Fault traces are commonly linear features with wavy irregularities (Candela et al., 2012; Brown & Scholz, 1985) observed at all spatial scales (Brown & Scholz, 1985; Power et al., 1987; Power & Tullis, 1995; Renard et al., 2006). A newly formed young fault has a higher level of fault roughness and then the slip on the fault decreases it over time (Sagy et al., 2007). The fault profile and its related roughness properties are important since these can change the behavior of rupture propagation during an earthquake (Bruhat et al., 2016) and can introduce local stress heterogeneities that are in some cases similar to magnitude of regional stresses of the area (Chester et al., 2004). In our study, we change the fault profile while keeping all the other parameters fixed and run multiple dynamic rupture simulations to get different earthquake rupture scenarios, and then analyze how the stresses in each rupture scenario define the damage in the fault zone. Fault roughness profiles are described using self-affinity in literature (Dieterich & Smith, 2009; Bruhat

et al., 2016). A self-affine fractal is a curve which needs the re-scaling of its height and length by different factors to get similar statistical properties, i.e. if $x \rightarrow \alpha x$ then $y \rightarrow \alpha^H y$. Here 'H' is called the Hurst exponent. if $H = 1$, it means the length and height are multiplied by same factor. This is the case of self-similar fractals. In this study, we only consider ruptures on a self-similar fault profile. Earlier studies (Brown & Scholz, 1985; Power & Tullis, 1995; Lee & Bruhn, 1996) showed that natural fault surfaces are self-similar fractals. Recent studies (Sagy et al., 2007; Renard et al., 2006; Brodsky et al., 2011; Candela et al., 2012, 2009, 2011) are able to provide very high resolution fault roughness measurements. Some of these measurements suggest that fault surfaces specifically in the slip-parallel direction are better described as self-affine fractals.

The power spectral density of a self affine fractal profile can be represented as:

$$p(k) \propto k^{-1-2H}, \tag{4.1}$$

Where $p(k)$ represents the spectral density and k represents the wave number (i.e. spatial frequency) defined as $k = \frac{2\pi}{\lambda}$. For the case of a self-similar fault profile, the exponent in equation 4.1 becomes -3. The proportionality constant for Eq. 4.1 is equal to $2\pi^3\gamma^2$, where γ is the RMS height to wavelength ratio of the fractal fault profile. This ratio (also referred to as RMS deviation of a fault profile from planarity) represents the maturity of the fault profile and takes values between 10^{-2} to 10^{-3} based on a fault maturity (Brodsky et al., 2011). We use an RMS value of 10^{-2} in all of our simulations. This value is typical for immature young faults that have not hosted many earthquakes. These immature faults are particluarly relevant for this study due to the fact that immature faults do not yet have well formed damage zones (Faulkner et al., 2011; Myers & Aydin, 2004; Andrews, 2004). It remains an open question how these damage zones form temporally over the initial earthquakes occurring on an immature fault, and our study aims to use numerical modeling to examine those dynamics.

In the dynamic rupture code, the desired fault surface is constructed using a Fourier

method given by Andrews & Barall (2011). The minimum wavelength in all of our dynamic rupture simulations is taken to be 20 times the short term model grid spacing (Δx) as given in Table 1.

Model setup

We consider a 2D plane strain model for both short-term dynamic model (SDM) and long term tectonic model (LTM) simulations. The details of SDM and LTM model are given in the following subsections.

Short term simulations: Dynamic earthquake rupture modeling

To model short time scale dynamics related to earthquake rupture propagation, we use rupture dynamics code fdfault v.1.0. This code solves the elastodynamics wave equation using finite differences and is been verified in different benchmarks problems developed by the Southern California Earthquake Center (Harris et al., 2009, 2018). The code has a 4th order accuracy in both time and space.

For this model, our domain is 120 km long and 70 km wide as can be seen in Fig. 26. A strike-slip fault is pre-existing in the model with same length as the length of the model domain. The fault is represented by a self-similar fractal fault profile with RMS height of 0.01 as can be seen by curve $f(x)$, shown in Fig 26(a) by red color. This profile deviates from $y = 35$ based on the values of RMS height.

We run numerous simulations of rupture propagation on different realizations of the self-similar fault profile to pick three different rupture propagation scenarios. The three different rupture scenarios are sub-shear rupture, super-shear rupture and arrested rupture. In the sub-shear rupture scenario, the earthquake rupture starts with a sub-shear velocity from its nucleation zone and follows similar rupture speeds while breaking the whole length of the fault. In the super-shear rupture scenario, the earthquake rupture starts with a sub-shear velocity from its nucleation zone but soon converts into super-shear rupture while breaking the whole length of the fault. The transition from sub-shear to super-shear happens due to the geometry of the fault profile (Bruhat et al., 2016; Aslam & Daub, 2018).

98
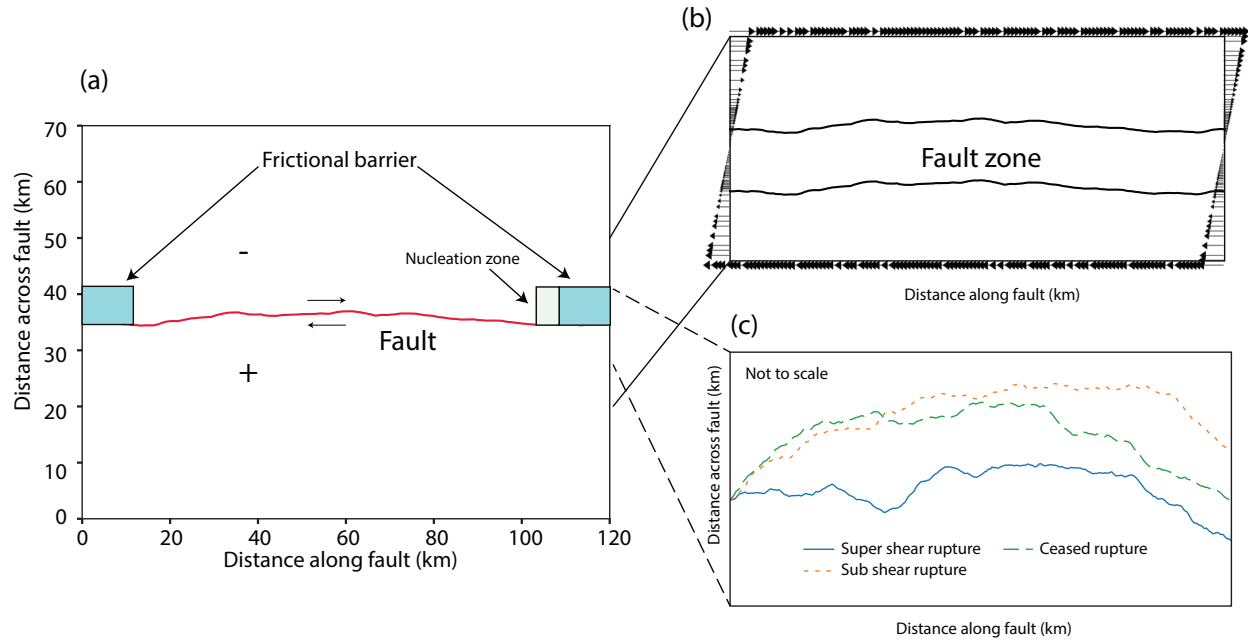
Fig. 26: A sketch of model setup for both SDM and LTM simulations. (a) Domain setup for the SDM model. A pre-existing strike-slip fault with inherent roughness is shown. The fault is 120 km long with two frictional barriers of 15 km width at each side. The rupture starts at one side of the fault so that in each case we get a unilateral rupture with most of the plastic deformation on one side of the fault. In our case, most of the plastic deformation occurs on the extensional side of the fault. The extensional side is marked in the figure with '-' sign while the compressional side is marked with a '+' sign. The compressional and extensional sides are determined by the sign of the fault-parallel strain ϵ_{xx} along the fault surface right next to the rupture front. The fault has $H = 1$ and RMS height $= 0.01$. (b) Domain setup for the LTM model. The model is driven by a shear velocity boundary condition (a half plate velocity of 1 cm/yr) while the initial conditions of stress and strain are provided from the SDM model. (c) Three realization of fault profile with $H = 1$ and RMS height $= 0.01$. These fault profiles are responsible for the three different earthquake rupture scenarios.

In the arrested rupture case, the earthquake rupture starts with a sub-shear velocity from its nucleation zone and dies out after rupturing a certain length of the fault. The arrest of the rupture occurs due to the geometry of the fault profile. A few of the fault profiles used in this study are shown in Fig. 26(c). In each of our simulations, all the initial conditions of the model (given in Table 1) remains the same except the geometry of the fault profile.

All of our simulations assume Drucker-Prager plastic off-fault material properties. The plastic parameter values used in this study are given in Table 1. The yield criterion for the Drucker-Prager plasticity can be found in Fig. 27. We assume a uniform initial background stress field (negative for compressive stresses and vice versa) in all of our simulations (Table 1). These stresses give heterogeneous initial shear and normal tractions along each point on the fault due to non-planarity of the fault surface.

We describe the on-fault failure using the slip weakening friction (SWF) law (Ida, 1972; Andrews, 1976, 1985; Day, 1982). The SWF law gives a linear decrease of static friction to dynamic friction as a function of slip on the fault over a critical slip distance. We choose the static friction value $\mu_s = 0.7$ and dynamic frictional value $\mu_d = 0.2$, which gives us a larger value of the strength drop. We use a critical slip distance of 0.4 m.

We always nucleate ruptures from right side of the fault. Instead of choosing the rupture nucleation location arbitrarily, we choose it based on the location where the shear to normal stress ratio is highest. We expect such locations to be representative of the locations on natural faults where ruptures are likely to initiate (Fang & Dunham, 2013; Oglesby & Mai, 2012; Mai et al., 2005). We generate many fault profiles and calculate the shear to normal stress ratio across the whole length of the fault. If this ratio is highest between our desired sub-length (i.e. from 80 to 110 km along fault), we perform rupture simulation on this profile, otherwise we discard this fault profile.

The choice of initiation strategy is important to consider when using SWF law to initiate ruptures, since the final slip distribution as well as the initial release of seismic waves during an earthquake dynamic rupture are sensitive to the initiation strategy. Based

$\bar{\tau}$

μ_{dp} | 1

c_{dp}

$\mu_{dp}(-\sigma_{kk}/3) + c_{dp}$

$-\sigma_{kk}/3$

τ

$CF = \bar{\tau}/ (\mu_{dp}(-\sigma_{kk}/3) + c_{dp})$
$c_{dp} = c\ \cos\phi$
$\mu_{dp} = \sin\phi$

c

$-\sigma_m$

$-\sigma_n$
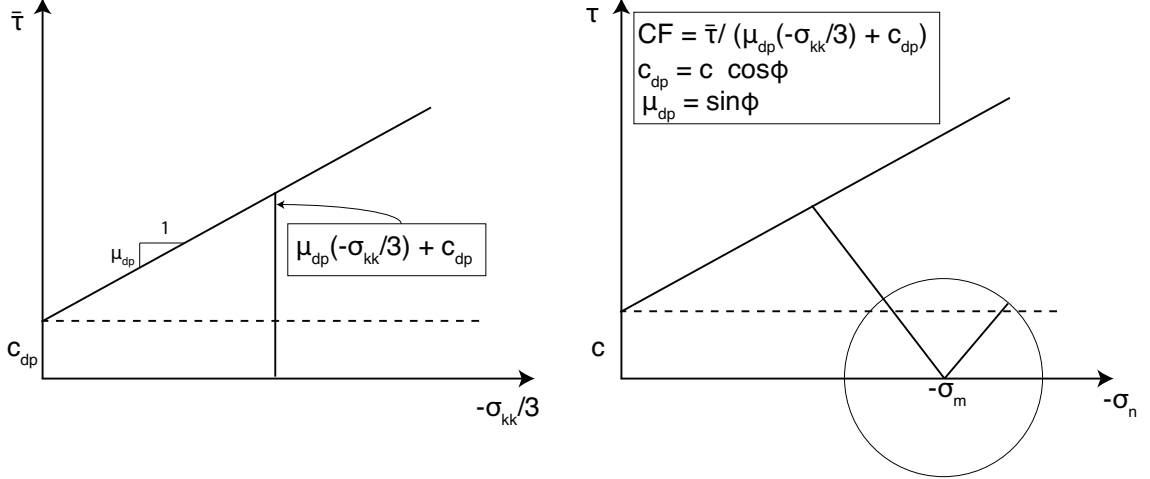
Fig. 27: (a) Yield criteria of the Drucker-prager (DP) plasticity. We use DP plasticity to describe the plastic deformation of rocks in our earthquake rupture propagation simulations. (b) Yield criteria of the Mohr-Coulomb (MC) plasticity. We use the MC plasticity to describe the plastic deformation in our LTM simulations. It is important to note that both criteria exactly coincide under certain 2D stress conditions.

on our previous work (Aslam & Daub, 2018), we select the strategy of over-stressing a certain patch length (3 km) of the fault and increase its shear traction to a value equal to 1.01 of the failure stress of the fault.

Long term simulations: Tectonic modeling

To explore how the heterogeneous stresses and damage influence strain accumulation during inter-seismic phase, we run our LTM model with initial conditions taken from SDM model. We use DynEarthSol3D (Choi et al., 2013) to run our inter-seismic earthquake phase simulation. DES3D is an explicit dynamic finite element code providing quasi-static solutions to the momentum balance equation via dynamic relaxation (Cundall, 1989) and mass scaling (e.g. Chung et al., 1998). The explicit formulation makes it easy to run the model over relatively shorter time scales (relative to the earthquake cycle) rather than the timescales of million of years typically associated with LTM models.

For this model, our domain is 40 km wide and has a length of 60 km. Figure 26(b) shows the simulation domain of LTM model. The LTM model starts with initial conditions provided by the SDM model. To discuss this in detail, we give the stress tensor, full strain
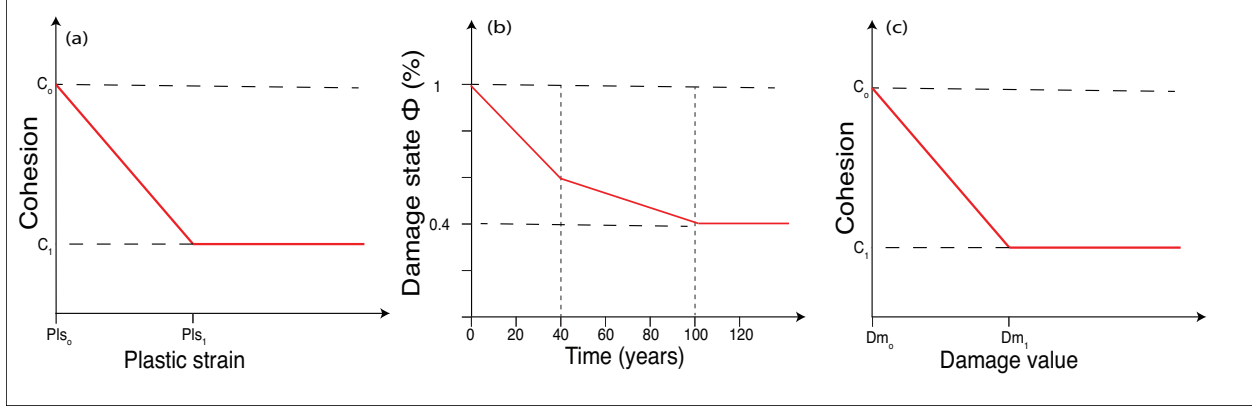
Fig. 28: Plots showing the strain and state behavior of off-fault material. (a) Strain dependence is modeled using strain softning. The cohesion value (after a certain value) is reduced with the increase of plastic strain accumulation. This is done until a threshold value is reached. (b) A damage parameter is used to model the state evolution. As the time increases, the damage state recovers from its initial state to a healed state. (c) With the recovery of the damage, the cohesion value also recovers.

tensor and plastic strain from SDM model to LTM. We extract these values at a certain time from sub-domain of SDM (i.e. from 20 to 80 km along fault and 15 to 55 km across fault distance) and then provide it to initialize the LTM model to start the LTM simulation. The LTM model is loaded with a half plate velocity of 1 cm/year from top and bottom boundaries. On the left and right boundaries, the loading conditions impose simple shear. At the farthest distance from the location of fault zone, the loading magnitude is same as the shared top or bottom boundary and then it gradually decreases towards the fault. The loading magnitude reaches a zero at the fault profile. It is important to note that no fault exists in the case of LTM model.

We model the off-fault material deformation with Mohr-Coulomb (MC) frictional law [e.g., Poliakov et al., 1994; Poliakov and Buck, 1998]. An important point to note is that both DP and MC criteria exactly coincide (Fig. 27) for 2-D stress state if $S_{zz} = (S_{xx} + S_{yy})/2 = S_{kk}/3$. Here S_{zz} is out of plane principal stress and S_{xx} and S_{yy} are in plane principal stresses. The cohesion and the friction angle are related to the DP parameters as follows: $c_{dp} = c \cos\phi$ and $\mu_{dp} = \sin\phi$. Figure 27 shows both DP and MC yield criteria.

We consider the strain and state dependence of plastic deformation of the off-fault material. We model the strain dependence using strain softning while state dependence using a state evolution law. The strain softning is observed once the friction coefficient or cohesion is decreased with the increase of permanent deformation, this strain dependence is used to produce strain localization (Popov & Sobolev, 2008; Poliakov & Buck, 1998; Choi et al., 2013) in LTM models. Figure 28 (a) shows the process of strain softning: the cohesion is kept constant until a certain plastic deformation value (Pls_0) is reached. Once the plastic deformation exceeds this value, the cohesion value decreases linearly with the accumulation of more plastic strain to a certain plastic strain value given by Pls_1. A similar model can be used to decrease the friction coefficient from its initial value ϕ_0 to final ϕ_1 value with the increase in plastic deformation. Our strain weakening parameter values are provided in Table 2. To model the state dependence, we define a damage state of the off-fault material at each time step during the simulation. The damage value of this damage state is equivalent to the plastic strain accumulated at that time step. The damage state then recovers (heals) with time according to the law shown in Fig. 28(b). The healing process decreases the value of damage parameter and then based on the new value of damage parameter, the cohesion value is healed as shown in Fig. 28(c). This time evolution law (shown in Fig 28(b)) is a simplified form of the damage model used by Finzi et al. (2009), which was adopted based on observational (Ben-Zion et al., 2003; Peng et al., 2003; Hamiel & Fialko, 2007) and laboratory studies (Tenthorey et al., 2003). As can be observed in Fig. 28(b), the healing process is faster in the first 40 years of inter-seismic phase and then the rate of healing slows down to half of its starting rate. No healing occurs after 100 years during interseismic phase.

Table 5: List of parameter values for SDM used in this study

Parameters for	Parameter name	Symbol used	Value
Model Domain			
	Domain length	X_{SDM}	110 km
	Domain Width	Y_{SDM}	70 km
Material properties			
	Shear wave speed	α	6000 m/sec
	Compressional wave speed	β	3464 m/sec
	DP internal friction parameter	μ_{DP}	0.5735
	DP plastic dilatancy parameter	β	0.2867
	DP cohesion parameter	c	5 MPa
	DP viscosity parameter	η	0.2775 GPa.s
Friction law			
	Static frictional coefficient	μ_s	0.7 km
	Dynamic frictional coefficient	μ_d	0.2 km
	Critical slip distance	D_c	0.4 m
Initial condition			
	Stress	σ_{xx}	-100 MPa
	Stress	σ_{xy}	45 MPa
	Stress	σ_{xz}	110 MPa
Fault Roughness			
	Hurst exponent	H	0.5 - 1.0
	RMS height to wavelength ratio	γ	0.01 - 0.001

Results

Figure 29 shows the initial shear and normal tractions on the fault for three different SDM simulations. The initial stress tensor is uniform in the SDM model but the heterogeneity of the geometry of the fault profile leads to the complex initial tractions on the fault. As can be seen in Fig. 29, for some points on the fault the traction value is half of its maximum value. The fault profiles responsible for the tractions seen in Fig. 29 are shown in Fig. 26(c). Note that while all of the fault profiles have the same statistical properties, random variability creates different conditions that allow the ruptures to propagate differently. The sub-shear rupture has fairly uniform shear and normal tractions along strike (Fig. 29(a)), leading to steady rupture propagation (as shown in plot Fig. 29(b)). The super-shear rupture exhibits lower normal tractions (Fig. 29(c)) on the fault, allowing the shear waves radiated from the hypocenter to nucleate a second rupture that travels faster than the shear wave speed (Fig. 29(d)). The lower plots (Fig. 29(e-f)) show the rupture that gets arrested. This particular fault profile has a patch with a high normal traction around 40 km along strike that the rupture is unable to break, leading to arrest. This suggests that geometry of the fault profile is an important factor to consider since it can cause huge variations of traction along the fault which leads to a significant effect on the rupture propagation.

We next examine how different geometrical heterogeneities control the stress distribution in the off-fault region for these different rupture scenarios. We are interested in how ruptures that propagated differently exhibit variations in the stress redistribution in the near-fault region. Figure 30 shows the shear and normal stress in the simulation domain after 48 sec in the sub-domain of the model. We select the middle portion of the whole domain since we are interested in the static stress changes, and selecting a small portion of the modeling domain can avoid effects from dynamic waves that are propagating away from the modeling sub-domain. The time chosen to extract these stress values in each rupture case is long enough so that dynamic waves have significant time to propagate away
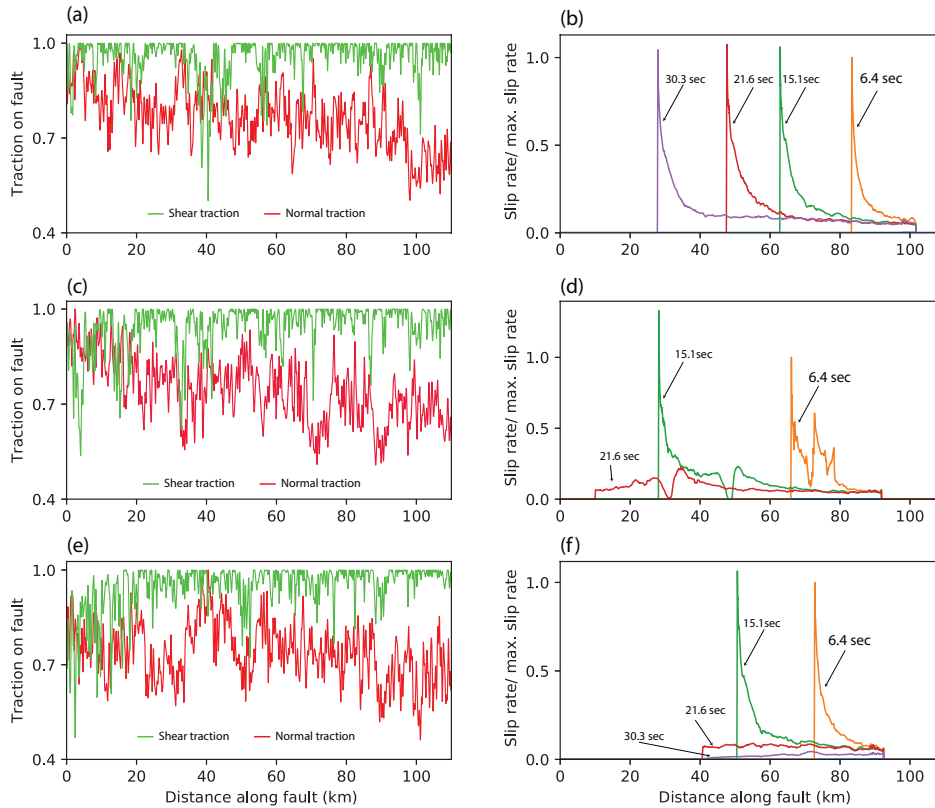
Fig. 29: Plots showing initial tractions on the fault and snapshot of slip rate along the fault at different times. Both shear and normal traction values are normalized by the maximum value. The geometry of fault profile causes the tractions on the fault to be highly heterogeneous although the regional stresses are homogeneous. The slip rate values are normalized by the maximum slip rate value at 6.4 sec. We do this to analyze if slip rate grows or decays with time as the rupture propagates. (a) Initial values of shear and normal tractions at the fault surface for the case of sub-shear rupture. (b) The slip rate along the fault at different times for the fault profile whose tractions are given in (a). The rupture starts and propagates with a sub-shear velocity. (c) Initial values of shear and normal tractions on the fault surface for the case of super-shear rupture. (d) The slip rate along the fault at different times for the fault profile whose tractions are given in (c). The rupture starts with sub-shear velocity but later on transitions into a super-shear rupture due to favorable fault geometry. (e) Initial values of shear and normal tractions on the fault surface for the case of arrested rupture. (f) The slip rate along the fault at different times for the fault profile whose tractions are given in (e). The rupture starts with a sub-shear velocity but dies at a particular time since it gets trapped due to a fault geometry that is not favorable for further rupture propagation.

from the sub-domain. As can be seen that for all the rupture cases (Fig. 30), the stresses are heterogeneous in the vicinity of the fault. There is no major difference between the stresses observed for any of the rupture propagation scenarios around the fault length that has already been ruptured. We observe many regions of positive shear stress change present around the ruptured fault which are important for future seismic hazard as the Coulomb failure stress may also be higher in those regions. For the case of arrested rupture, as expected, we see a band of stress increase in the region next to the rupture arrest. The stress heterogeneity dominates the locations closer to the fault, while away from the fault, the heterogeneity reduces and the stresses are more uniform. The distance to which the stress heterogeneity is dominant depends upon the RMS height of the fault profile. We refer to the off-fault region where it is affected by fault roughness as the region affected by fault roughness (RAFR) and focus our discussion to that region.

Figure 31 shows the accumulated plastic strain (second invariant of plastic strain tensor) for the domain shown in Fig. 26. The plastic strain accumulates on the extensional side of the fault as can be seen in the figure. The strain is localized as a result of local bends in the geometry of the fault profile. For the case of super-shear rupture (Fig. 31(b)), most of the plastic strain accumulates in the vicinity of the fault or exactly on the fault. Similarly, for the sub-shear as well as the arrested rupture case 31(a) and 31(c), we observe the plastic strain to be localized to locations closer to the fault profile. We note a clear difference between the plastic strain fields for the sub-shear and super-shear ruptures: the super-shear rupture exhibits patches of strong damage further from the fault than we see in the sub-shear rupture. The sub-shear rupture plastic deformation is restricted to being closer to the fault, though the differences are probably not significant enough to permit comparison with different observations of off-fault damage. This difference in spatial location is likely due to differences in the coherence of the shear waves, which carry the dynamic stresses responsible for bringing a fault to the yield point. Since the super-shear rupture produces more coherent waves further from the fault, it produces more damage

107
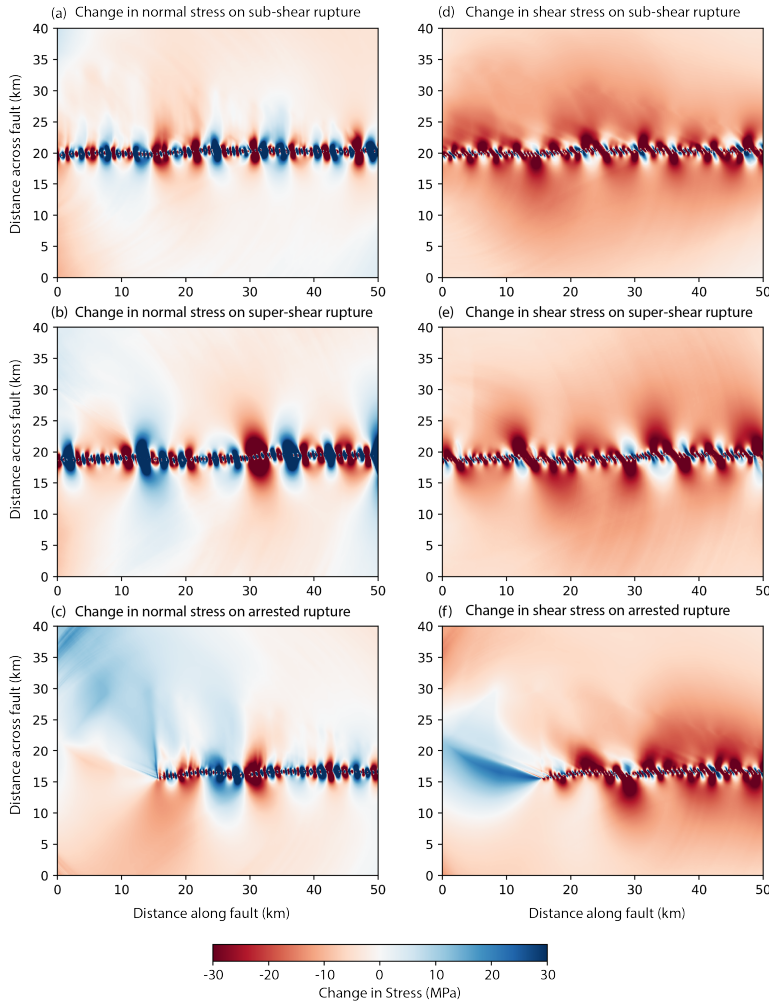
Fig. 30: Change in stresses at the central part of the domain (taken from 25 to 75 km along fault and 15 to 55 km across the fault). Figure (a), (b) and (c) are showing change in normal stresses in the central part of modeling domain while (d), (e) and (f) are showing change in shear stresses in the central part of modeling domain. These stresses are taken at a particular time ($\sim$ 48 sec) so that the rupture has propagated far enough from the central part and there are no dynamic stresses related to the wave propagation and stress change is solely due to static stress changes. This complicated shear and normal stress change will also give a complex Coulomb stress change.

Fig. 31: Accumulated plastic strain (second invariant of plastic strain tensor) in the central part of the domain (20 to 70 km along fault distance and 15 to 45 across fault distance) at the time ~ 48 sec after the start of rupture simulation. (a) The case of sub-shear rupture, (b) the case of super-shear rupture, (c) the case of arrested rupture. We have taken this sub-domain to provide results that does not involve any boundary effects.

farther from the fault. The arrested rupture includes a strong patch of plastic strain near the crack tip that does not align with the main fault, which we will see leads to further deformation along this same direction.

To study the evolution of damage in the region close to the fault in the inter-seismic phase as a result of earthquake on a complex fault, we extract the stress tensor, full strain tensor, and the scalar plasticity from SDM subdomain as an initial condition for LTM model and then run the LTM model for 200 years to examine how the complex initial conditions of off-fault medium due to earthquake rupture on a complex fault governs the evolution of damage in the near-fault region during the inter-seismic phase. Figure 32 shows the plastic strain accumulated during the inter-seismic phase in the region $10 - 60$ km along the fault parallel direction, as a result of the tectonic plate loading. The region outside this sub-domain is not shown as that region may have been contaminated by boundary effects. In all of the rupture cases, we observe shear features forming and mostly growing at oblique angles to the main fault. Some of these features are marked with A,B, C and D in Fig. 32. The development and growth of these new features occurs in the locations where geometrical bends in the fault profile have caused the deformation in the dynamic phase to be localized. This localized deformation due to fault roughness acts as a seed for the development of new features. As can be seen together with the shear bands growing with the provided loading, there is considerable amount of strain accumulated along the immediate sides of the fault profile. These are the locations where the next earthquake is likely to nucleate in each simulation due to the stress conditions combined with the plastic deformation leading to reduced cohesion. The arrested rupture clearly favors rupture at the arrested crack tip, though many locations in the ruptured areas of each simulation also lead to additional deformation. We find that the deformation in each case is steady with time, and does not show any particular temporal characteristics beyond the linear ramp provided by the external loading.

The off-fault deformation is complex with development of new shear features in the
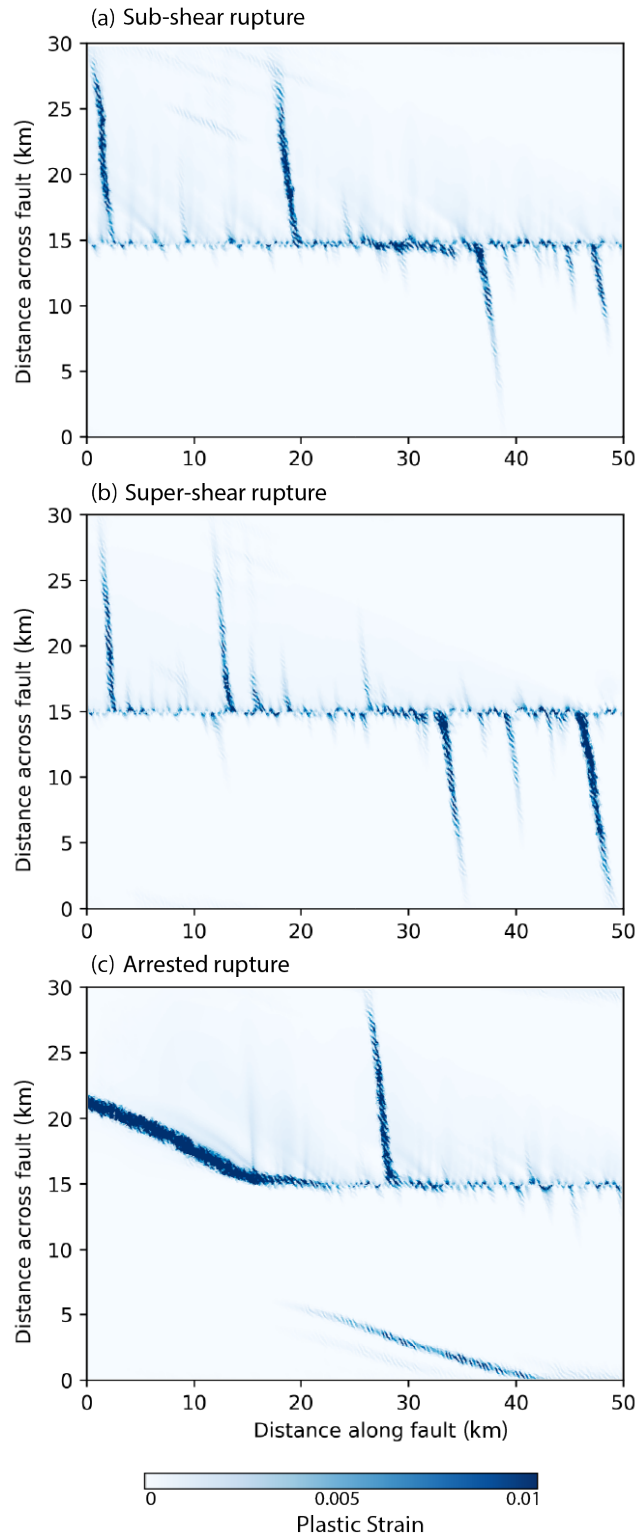
Fig. 32: Accumulated plastic strain (second invariant of plastic strain tensor) at the modeling subdomain region (25 to 75 km along fault distance and 15 to 45 across fault distance) at time 200 years after the earthquake. (a) The case of sub-shear rupture, (b) the case of super-shear rupture, (c) the case of arrested rupture. We have taken this sub-domain to provide results that does not involve any boundary effects.

111
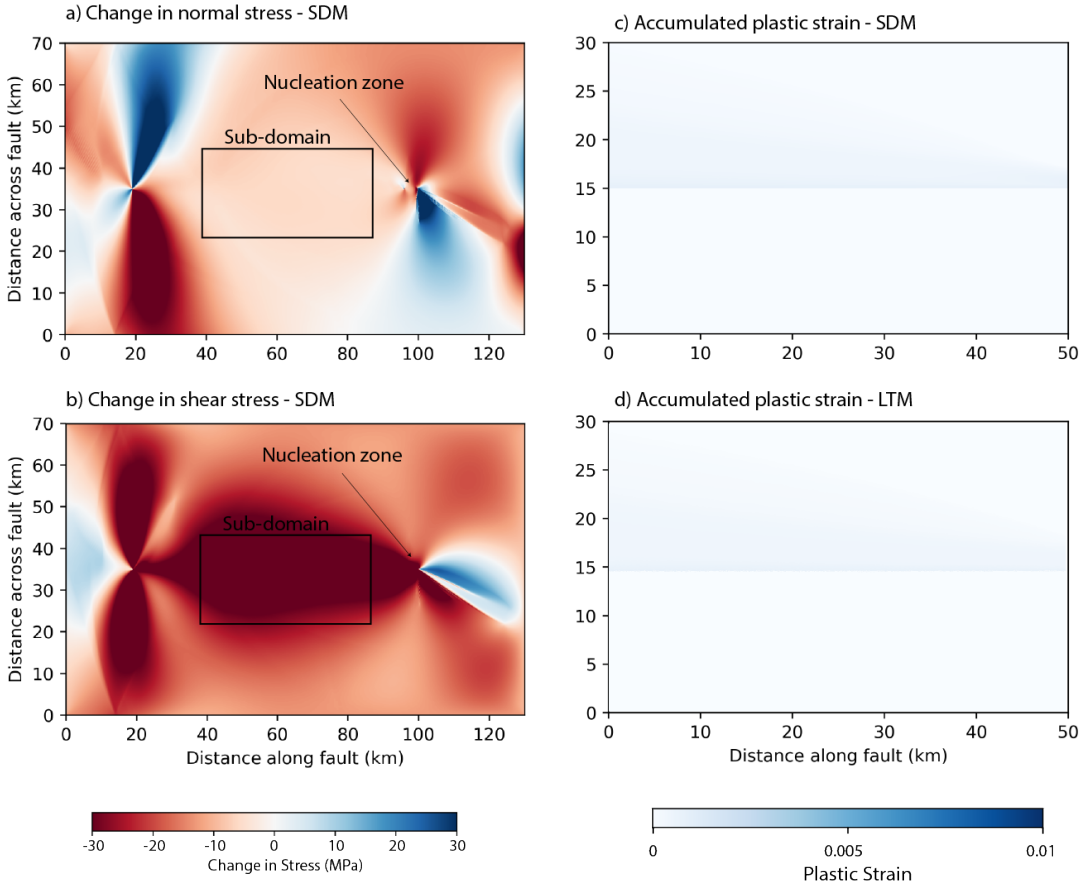
Fig. 33: The case of coupling on a flat fault. Figures (a) and (b) show the change in stresses (normal and shear stress respectively) from the modeling sub-domain (25 to 75 km along fault distance and 15 to 45 across fault distance) at a time ~ 48 sec after the start of simulation. The change in stress in the whole modeling domain domain is shown in the inset of (a) and (b). The rectangles at the inset figures in both 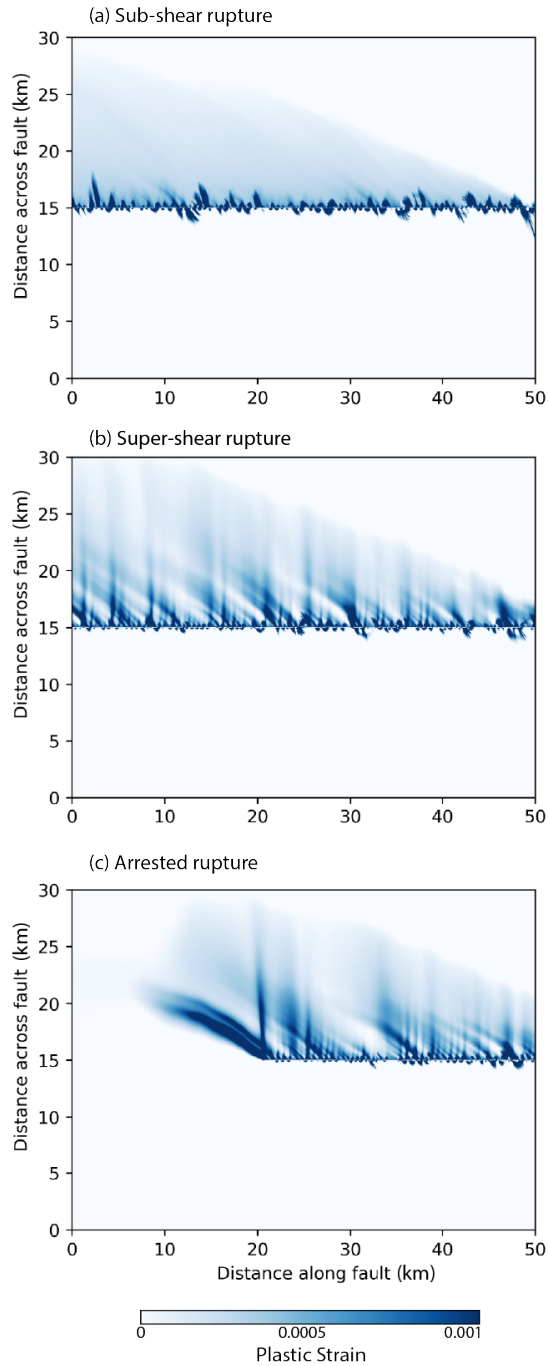(a) and (b) shows the extent of figure (a) and (b) respectively. (c) Accumulated plastic strain (second invariant of plastic strain tensor) at the central part of the domain (25 to 75 km along fault distance and 15 to 45 across fault distance) at time ~ 48 sec after the start of rupture simulation. (d) Accumulated plastic strain (second invariant of plastic strain tensor) at the modeling subdomain region (25 to 75 km along fault distance and 15 to 45 across fault distance) at time 200 years after the earthquake.

inter-seismic phase. We observe deformation on both sides of the fault during the inter-seismic phase, not just on the extensional side of the fault. This explains us that it is not necessary to have bi-lateral ruptures or the multiple ruptures with different rupture propagation directions to develop a fault zone on each side, but rather damage can occur on both sides of the fault during inter-seismic deformation if the fault is geometrically complex.

To observe how damage evolves during inter-seismic phase for a rupture that occurred on a flat fault rather having complex geometry, we run a dynamic earthquake rupture simulation with similar initial setup (i.e. initial conditions and domain setup). The only difference is that the fault is flat. Figures 33(a) and 33(b) show the shear and normal stress changes as a result of rupture propagation on the flat fault for the sub-domain shown in inset of Fig. 33(a) and Fig. 33(b). As expected, we do not observe any complex static stress change pattern in the case of flat fault and most of the stresses follow a homogeneous pattern. This behavior is similar to what is observed for distances farther from the RAFR region during rupture on complex fault. Figure 33(c) shows the plastic strain accumulation as a result of the rupture on the fault. As the strain accumulates on the extensional side of the fault, no localized features of strain accumulation develop. This is because there are no local fault bends in the geometry of the fault profile to concentrate stresses. When we run an LTM model for the inter-seismic phase for the flat fault, we do not observe any localized shear zones developing and growing in the fault damage zone, as was the case of rough fault, but all the damage occurs on the right and left boundary of the fault. This is shown in Fig. 33(d) where no differences can be observed between 33(c) and 33(d). Based on our comparison of Fig. 33 and Fig. 32 , We suggest that the fault surface roughness is one of the important factor driving the spatial development of the complex damage pattern observed in the fault damage zones.

Discussion

In this study, we perform coupling of SDM-LTM models to capture the physics of the earthquake cycle when the rupture occurs on a complex fault. Our initial rupture simulations are performed on complex faults in 2D, incorporating off-fault plastic failure and deformation, and strong dynamic weakening on the fault governed by SWF law. Using the stress and deformation from our initial simulations, our final LTM model simulations are performed in 2D where the modeled is loaded with far-field plate motion and the off-fault material properties are governed through strain and state behavior. We explore the dynamics of off-fault plastic deformation and variability of the strain accumulation process over the entire seismic cycle. The main objective of this study is to capture the dynamics of near-fault regions during the inter-seismic phase in response to dynamic rupture on a complex fault. This evolution is not possible to capture when running a quasi-dynamic (Erickson et al., 2017; Allison & Dunham, 2018) or quasi-static (Smith & Dieterich, 2010; Powers & Jordan, 2010; Smith & Heaton, 2011)) model for earthquake cycle since a significant information of dynamic part is generally lost in those models. Our modeling approach combines two models with different strengths and resolutions while considering ruptures on rough faults, hence we suggest that this modeling approach tend to better capture the inter-seismic deformation of fault damage zone.

The SDM model shows heterogeneous stresses close to the fault with localized regions of high strain accumulations. The strain accumulates on the extensional side of the fault (Templeton & Rice, 2008; Ben-Zion & Shi, 2005; Andrews, 2005) and the accumulation of strain increases with the increase in distance of rupture propagation. We note a clear difference between the plastic strain fields for the sub-shear and super-shear ruptures. We observe patches of strong damage further from the fault for the super-shear case as compared with sub-shear rupture case. This difference is likely due to differences in the coherence of the shear waves (Bruhat et al., 2016; Shi & Day, 2013), which carry the dynamic stresses responsible for bringing a fault to the yield point. Since super-shear

114

produce more coherent waves farther from fault, this causes the damage to accumulate farther from the fault as compared to sub-shear rupture. Bouchon & Karabulut (2008) investigated the spatial distribution of aftershocks of many earthquakes which ruptured as a super-shear rupture. They found out that the aftershocks are distributed over a wide zone around segments that ruptured with super-shear speed. They concluded that the coherent waves from super-shear ruptures produce large stresses in a wider region surrounding a fault, which results in a wider aftershock zone. Since the co-seismic damage is observed farther from the fault in the case of super-shear rupture, we suggest (based on our results from chapter 3) that a wider region with optimal orientations results in a wider aftershock zone which is observed for natural super-shear ruptures (Bouchon & Karabulut, 2008).

Our comparison of coupled simulations performed on a rough fault and a flat fault suggests that, during the co-seismic phase, the stresses concentrate near the fault bends due to rough fault profile. These concentration of stresses form highly localized zones of plastic deformation (Dunham et al., 2011c; Johri et al., 2014; Aslam & Daub, 2019). During the inter-seismic phase, these localized zones of plastic deformation favor the development of shear-zones and their growth causing development of a complex fault zone. In the co-seismic phase of a flat flat, we do not observe any complex shear patterns which can cause the development of localized zones of high strain accumulation. Hence no further shear-zone formation is observed for the flat fault in the inter-seismic phase. This further suggests that the near-fault damage zones of mature fault should be significantly complex as compared to the damage zones of the immature faults. This is because those faults have hosted many events. In each successive event, the co-seismic slip results in development of new damage, which grows the damage zone as well as smooths out the geometry of damage zone. It has been observed in many fault zone studies that the damage zones of mature faults has a higher damage complexity with many localized shear zones, a variety of fracture types, and a number of fault orientations (Milliner et al., 2015). Furthermore, the locations of the localized shear bands formed during the co-seismic phase are important,

since these are the locations where the next earthquake is likely to nucleate due to the stress conditions (largest shear to normal stress values) combined with the plastic deformation leading to reduced cohesion. Although locations of each single localized shear band is difficult to determine, the arrested rupture clearly suggests that the location of major localized shear-band formation is the vicinity of the arrested crack tip.

Fault damage zones are observed in many observational studies (Faulkner et al., 2010, 2011; Myers & Aydin, 2004; Andrews, 2004, 2005; Rice et al., 2005; Chester & Logan, 1986; Chester et al., 1993, 2004; Biegel & Sammis, 2004; Caine et al., 1996). These zones are weaker than the country rock (Faulkner et al., 2003; Cochran et al., 2009; Hauksson, 2011, 2010; Armijo et al., 1996; Powell & Weldon, 1992; Şengör et al., 2005; Finzi et al., 2009) and can significantly affect seismic hazard (Hauksson, 2011, 2010). Our coupled earthquake cycle simulation is performed only considering a single earthquake cycle i.e. the damage observed in LTM is a result of a single earthquake only, but the real observed fault zones are result of damage of numerous earthquakes on the fault. It is not straightforward to compare our results with real damage zones, but our results can give insights into the processes happened during the observed fault zone formation. for example, from our model, we clearly observe that it is not necessary for a fault to have many multi-sided ruptures to have damage zone on both sides of the fault but rather a single uni-lateral ruptures can also form damage zone on both extensional and compressional sides during the loading phase of an earthquake. The material contrast on either side of the fault can influence the growth of the fault damage zone (Rubin & Gillard, 2000; Rubin & Ampuero, 2007), as was observed by Powers & Jordan (2010). We did not model any material contrasts in this study, so we are not able to address how material contrasts affect the growth of damage zone.

In our model, off-fault material healing is observed through the state behavior. The state of damage of the material recovers with time. The off-fault material damage healing has been studied in many different modeling contexts. We use a healing model simplified from Finzi et al. (2009) in this study, but more sophistic models of healing (e.g. (Finzi

et al., 2009; Lyakhovsky et al., 2005; Ben-Zion & Lyakhovsky, 2006)) can be used to observe how healing affects the dynamics of off-fault damage zone evolution. Furthermore, We model the strain dependence by strain softning, this model has been extensively used in the modeling studies (e.g. (Albert et al., 2000; Ahamed et al., 2018; Choi et al., 2013; Gerya & Yuen, 2007; Popov & Sobolev, 2008; Poliakov et al., 2002). This model is typically used in the studies that investigate shear zones. In our study, we only considered cohesion weakening but many studies have also used frictional weakening together with cohesion weakening to investigate shear zones.

Our modeling of a single earthquake cycle does not consider any feedback from LTM to SDM model. A more sophisticated earthquake cycle model should also consider feedback from LTM model (Jiang & Lapusta, 2016; Ahamed et al., 2018). Once the feedback is considered and the SDM model is run with pre-existing damage zone, then this may change the next rupture propagation on the same fault since the off-fault material is now much weaker than the previous rupture propagation. Furthermore, considering fault branches along with the main fault may also result in rupture jump from the main fault to one of its branching segments by completely changing its rupture propagation (Harris et al., 2018). Similarly, a propagating rupture, based on the orientation of the background stress field, may behave completely unexpectedly when it reaches a linked stepover (Lozos et al., 2011). Considering reverse feedback from LTM to SDM is important which allows us to run multiple earthquake cycle simulations with realistic initial conditions. Simulating multiple earthquake cycles on complex fault systems is a subject of future work.

Our simulations do not show any particular temporal character as we assume time-independent simple continuum plasticity to model the inter-seismic deformation. A similar depth-dependent model earthquake cycle model or a 3D model with appropriate rheologies for the lower crust and mantle (Allison & Dunham, 2018; Lippiello et al., 2015; Freed & Bürgmann, 2004), may able to retrieve some of the characteristics of observed post-seismic deformation (Barbot et al., 2009). Constructing a 2D depth dependent model

of the co-seismic and inter-seismic phase of a rough strike-slip fault to retrieve post-seismic deformation is a subject of future work.

Our coupled simulations are performed with some limitations. Due to computational efficiency, we run our model only in two dimensions instead of three dimensions. A wave propagation in 3D can be different from 2D in terms of geometric spreading and the length of time in which the disturbance is felt in off-fault medium (Dunham et al., 2011c). Similarly, considering fault roughness in the third dimension will tend to increase ground motion irregularities in the off-fault medium which may effect the stress distribution in the medium. Furthermore, we considered a relatively longer minimum fault roughness wavelength of 500 m in this study, while natural faults are rough over much smaller length scales that are not resolved in our simulations. Decreasing the wavelengths will add many more fault restraining and releasing bends which may cause changes in rupture propagation and increase of localized strain accumulation locations which may eventually alter the number of shear zones growing in the inter-seismic phase. We used a uniform initial background stress for our SDM model. A model run with feedback provided from LTM can be used to start SDM model with more realistic initial conditions that account for all previous deformation on that fault.

From our study, we conclude that the complex damage pattern of the fault damage zones exists and evolves throughout the earthquake cycle due to roughness of fault profile. The damage zone develops on both sides of the fault with different width on each side. The difference in width may be related to favored rupture propagation direction or material heterogeneity across fault. Our study provides a better understanding of damage zone evolution throughout the earthquake cycle. This understanding is necessary for forecasting hazard in a region, since the damage zone plays a role in controlling the decay of aftershocks with distance from fault, and may amplify ground motions of an earthquake (as was the case for Calaveras fault zone in central California) (Spudich & Olsen, 2001).

Table 6: List of parameter values for LTM simulations

	Parameter name	Symbol used	Value
Model Domain parameters			
	Domain length	X_{LTM}	60 km
	Domain Width	Y_{LTM}	40 km
Material properties parameters			
	Bulk Modulus	K	53.4 GPa
	Shear Modulus	G	32.04 GPa
Strain weakening properties			
	Initial plastic strain	Pls_o	0.01
	Final plastic strain	Pls_1	0.1
	Initial Cohesion	c_o	2.0 MPa
	Final Cohesion	c_1	0.2 MPa
Boundary condition parameters			
	Far-field velocity	v_{far}	1 cm/year

Chapter 5

Examining stress and ground motion patterns in numerical simulations of earthquake slip

Aslam, Khurram, Daub, Eric, Taborda, Ricardo, (in preparation, 2019), Examining stress and ground motion patterns in numerical simulations of earthquake slip, Journal of Geophysical Research.

Abstract

We present initial results from a set of three-dimensional (3D) deterministic earthquake ground motion simulations for the northern Canterbury plains, Christchurch and the Banks Peninsula region of New Zealand, which explicitly incorporate the effects of the surface topography. The simulations are done using Hercules, an octree-based finite-element parallel software for solving 3D seismic wave propagation problems in heterogeneous media under kinematic faulting. We couple Hercules with the South Island Velocity Model (SIVM), which includes changes to the SIVM code in order to allow for single repetitive queries and thus achieve a seamless final-element meshing process within the end-to-end approach adopted in Hercules. We present our selection of the region of interest, which corresponds to an area of 120 km x 120 km, with the 3D model reaching a depth of about 60 km. Our simulation parameters are set to a minimum shear wave velocity of 500 m/sec, and a maximum resolved frequency of 2.0 Hz. We use topographic data that has a resolution of 20 m. Our comparison of the ground motions between the topographic model and the flat model shows differences in ground motions for stations placed at higher elevations. These higher elevation stations have higher peak accelerations and longer duration of the signals when topography is considered, suggesting that the topography leads to stronger ground motions and additional resonance of seismic waves. The stations paced in the plain region do not show any major differences when comparing the flat and the topographic models. The spatial distribution of PGV values (at the surface), for simulations with a maximum frequency of 1 and 2 Hz, suggests that the amplifications are mostly present in the northwest part of our simulation domain. This part of the region has a relatively higher topographic variations as compared to other part of simulation domain. Based on our results, we suggest that topography of a region should be included in the hazard estimates of those regions, which have a higher topographic relief.

Introduction

The seismic energy radiated from an earthquake gets amplified or de-amplified by irregularities in the earth surface's. This occurs due to phenomenon like diffraction, scattering and focusing of seismic waves. Seismic wave amplification in areas of high topographic relief is considered one of the main reasons of concentrated destruction during numerous earthquakes (Geli et al., 1988; Paolucci, 2002). In the past, there have been many earthquakes during which damage due to high topographic relief is reported. These events include the 1909 Lambese earthquake (Levret et al., 1988), 1976 Fruili earthquake (Brambati et al., 1980), 1980 Irpinia earthquake (Siro, 1982), 1985 Chile earthquake (Celebi, 1987), 1986 Hualien earthquake (Chiu & Huang, 1992; Lee et al., 2009), the 1989 Loma Prieta earthquake (Hartzell et al., 1994) , 1994 Northridge earthquake (Spudich et al., 1996; Bouchon & Barker, 1996; Paolucci, 2002), 1999 Athens earthquake (Athanasopoulos et al., 2001; Paolucci, 2002), and the 1999 Chi-Chi earthquake (Huang, 2000).

Many studies have focused on understanding the effects of topography on ground motions. Some of them used analytical approaches (Geli et al., 1988; Sánchez-Sesma, 1985; Tsaur & Chang, 2009; Tsaur, 2011) and some (Restrepo et al., 2016; Komatitsch et al., 2004) used numerical modeling to understand the effects of topography. Although analytical studies done on this topic are limited to SH waves propagation with simple topographic geometries considered, they have been able to clarify the wave behavior in the presence of topographic profiles. Sánchez-Sesma (1985) analytically solved ground motions for a symmetric domain having shape of a wedge with incident shear (SH) waves. The difference between the incident wave amplitude and the amplitudes solved at the apex were very high. Tsaur & Chang (2009) presented analytical solution for a domain having circular-arc topography for a incident Ricker SH pulse with four different incidence angles. For an incidence angle of 0 degree, when the mountain height was increased, the amplification was also enhanced at the surface. The foot of the mountain observed the

largest amplification. When oblique incidence was considered, the amplification shifted from the base of the mountain towards the peak. Restrepo et al. (2016) used numerical simulations to study the topographic effects of the Colombian Andes by including heterogeneities in the topography of the Aburra Valley, Antioquia on surface ground motions. They ran four rupture scenarios of a magnitude 5 earthquake using three model scenarios (realistic 3D velocity structure with topography, 3D velocity structure without topography, and homogeneous half-space with realistic topography). They showed that at some locations there was topographic amplification as high as 500 percent while the locations within valley had a reduction in ground motions simulation about 150 percent. Komatitsch et al. (2004) used the spectral element approach to simulate ground motions in the Los Angeles Basin incorporating topography. Stupazzini et al. (2009) performed near-fault earthquake ground motion simulation in the Grenoble Valley, France using spectral element method. Their main emphasis was to study the effects of topographic variation of the area on the earthquake ground motions. Lee et al. (2009) performed ground motion simulations in the Yangminshan region of Taiwan using the spectral element method to study the topographic effects related to the area. They used a very high resolution digital elevation model (resolution $\sim$ 1m). Paolucci (2002) performed ground motion simulation of many areas in Italy, such as Castellaro, to observe the effect of topography.

The central Canterbury area of New Zealand shows significant variation in topography over small distances in the east-west direction. In the east of central Canterbury, the Banks Peninsula has variable elevation reaching $\sim$ 900 m. Moving east to west, this variable topography converts to the Canterbury plains, which further changes to mountainous terrain reaching an elevation of 1900 m in the west (Brown & Weeber, 1992; Forsyth et al., 2008). The total east-west relief of the region is about 2000 m. The Banks Peninsula on the east has mainly volcanic rocks of cenozoic to cretaceous age, the central plains has the youngest sediments while the western part mainly has sedimentary rocks of

early cretaceous to carboniferous age (Graham, 2008; Forsyth et al., 2008). The topographic relief as well as the geological structure is highly heterogeneous in the entral Canterbury area. These two factors are important in terms of earthquake ground motions in an area since they can significantly change the ground motions during an earthquake. They can either reduce seismic risk of an area by damping ground motions or significantly increase seismic risk of an area by amplifying ground motions of an earthquake (Geli et al., 1988).

The Canterbury area has hosted a sequence of earthquakes at the start of this decade known as the 2010-2011 Canterbury earthquake sequence. Some of the earthquakes in this sequence caused extensive structural and geo-technical destruction in the region (Lee et al., 2017; Kaiser et al., 2012; Bradley et al., 2014). Some previous studies (Bradley & Cubrinovski, 2011; Bradley, 2012)) have shown that one of the main factors enhancing the structural and/or geotechnical damage in the region was the effect of the three dimensional (3D) subsurface geologic structure of the area. This 3D subsurface geological structure introduced basin edge and waveguide effects that amplified the ground motions, causing significantly increased damage in the region. In addition to ground motion amplification due to subsurface geological structures, there may have been ground motion amplification due to wave-channeling and mountain edge effects associated with the significant variation of the topography in the region. Our study is mainly focused on investigating how the topographic variation of the central Canterbury region may affect the surface ground motion of a moderate magnitude earthquake in the same area.

We run earthquake ground motion simulations using a physics-based deterministic method with a point source and realistic 3D velocity structure of the the Canterbury region, New Zealand. Our simulation domain comprises a 120 km × 120 km × 60 km volume. We run our simulations with a maximum frequency of 2 Hz and minimum shear wave velocity of 500 m/sec. We use the finite element method code Hercules (Tu et al., 2006) with the topography implementation using a Virtual Topography scheme (Restrepo
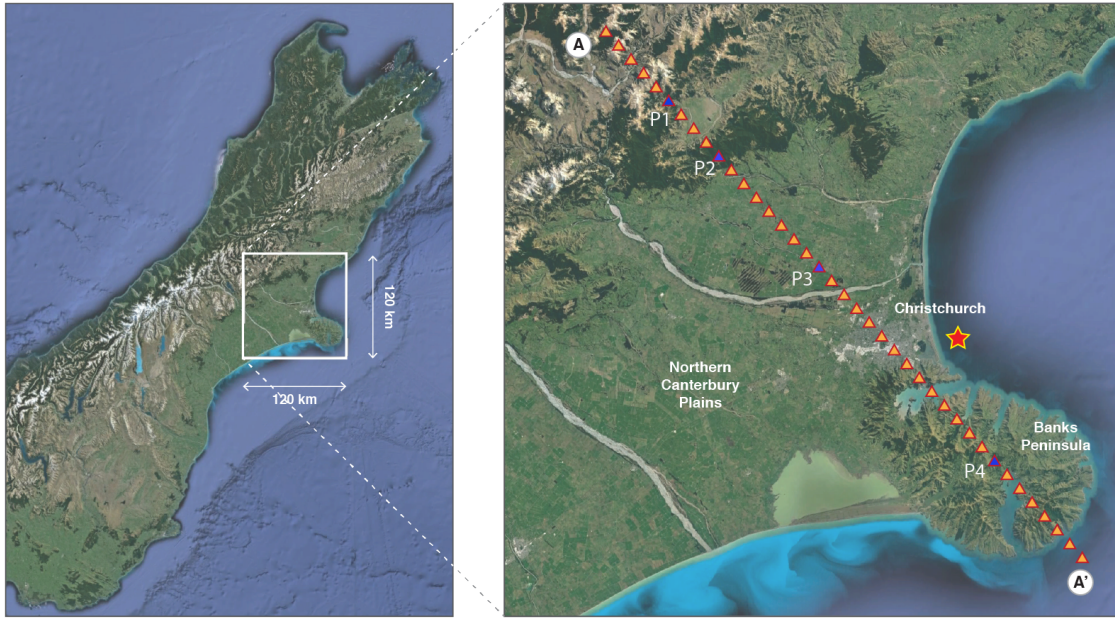
Fig. 34: Horizontal surface projection of the simulation domain in the South Island (left), and detailed inset of the simulation domain. The star indicates the epicenter location of the point source used in our simulations. It corresponds to an aftershock of the 2010-2011 Christchurch earthquake sequence, with a magnitude Mw 5.7. The triangles indicate the location of an artificial array of stations used for the analysis of results. Blue triangles on map show the locations of a few stations of interest (station P1-P4).

& Bielak, 2014). The topography resolution used in our study is $\sim$ 20 m. The objective of this study is to examine the main differences of ground motion between two models i.e. the flat model and the topographic model. We further observe the difference in ground motions in the same model by using two different attenuation assumptions i.e. elastic and inelastic. Our modeling study is performed to provide improved constraints on the effect of geomorphology of the Canterbury region on its seismic hazard.

Histotical and current seismicity of the Canterbury region

The area of Canterbury has hosted many damaging earthquakes in historical times. The 1869 earthquake of Magnitude 4.9 occurred near Christchurch City with an intensity measure of MM7 (Gledhill et al., 2011). The 1870 earthquake in the Selwyn District near Lake Ellesmere had an intensity measure of MM7 (Gledhill et al., 2011). The 1888 earthquake of M 7.0-7.3 occurred in Amuri District, North Canterbury had a reported intensity of MM9 near epicentre. This earthquake did significant damage to buildings and numerous landslides and rockfalls were reported as a result of this earthquake (Cowan, 1991). The 1901 earthquake with a magnitude of M 6.9 occurred in Cheviot, Hurunui District with a reported intensity of MM7. This earthquaked caused liquefaction at Kaiapoi (Pettinga et al., 2001). The 1922 earthquake of M 6.4 occured at Motunau, Hurunui District with an intenisty measure of MM7 Causing liquefaction in the areas of Pegasus Bay coast, Leithfield Beach and Waikuku (Pettinga et al., 2001). The 1929 earthquake of M 7.0 occurred in Arthur's Pass, Selwyn District (Doser et al., 1999), The 1946 earthquake of M 6.2 at Lake Coleridge, Selwyn District had a minor structural damage to buildings and the Lake Coleridge hydro-electric power station. Numerous landslides and aftershocks were reported due to this earthquake (Downes, 1995). The 1994 earthquake of Mw 6.7 Arthur's Pass, Selwyn District also did a considerable damage. Many landslides were mapped after this earthquake. A rock fall blocked one of the main state highways for almost a week. The Damage related to this earthquake was claimed to be more than US 3.2 million (Abercrombie et al., 2000). The 1995 earthquake of Mw 6.2

Cass, Selwyn District had an intensity measure of MM6 near epicenter. This earthquake was also a damaging earthquake (Gledhill et al., 2000).

The area of Christchurch gained serious attention after the 2010-2011 Canterbury earthquake sequence. The sequence started with September 2010 Darfield earthquake having a magnitude of 7.1 occurring about 40 km away from Christchurch. The main fault movement was strike-slip (Brackley, 2012). The earthquake was relatively shallow having a depth of 10.8 km. It occurred on a blind fault, the Greendale fault (Gledhill et al., 2011). The maximum horizontal displacement of Greendale fault was reported to be 5 m while the vertical displacement was reported 1.5 m. The surface rupture length was reported to be 30 km (Gledhill et al., 2011; Quigley et al., 2012; Potter et al., 2015). There was a significant aftershock sequence followed by the main event. Some strong aftershocks included the M 4.9 December 2010 earthquake, M 6.3 February 2011 earthquake, M 6.0 June 2011 earthquake and two earthquakes of Mw 5.8 and Mw 5.9 within the month of December 2011. The M 6.3 February event occurred beneath the Canterbury Plains having a very shallow depth (approximately 5 km). This event also occured on a blind fault with accelerations reaching 2.2 g in some areas (Kaiser et al., 2012). Similar accelerations were recorded (close to 2 g) for the June 2011 earthquake at some stations. The Canterbury plains and especially Christchurch city, is highly vulnerable to liquefaction. This is because Canterbury plains are built as a result of sedimentation from rivers that flowed from the southern Alps and deposited post-glacial alluvial gravels (Forsyth et al., 2008). This is what occurred during the 2010-2011 Canterbury earthquake sequence and many liquefaction sites were reported during this sequence which caused interruptions to the recovery effort.
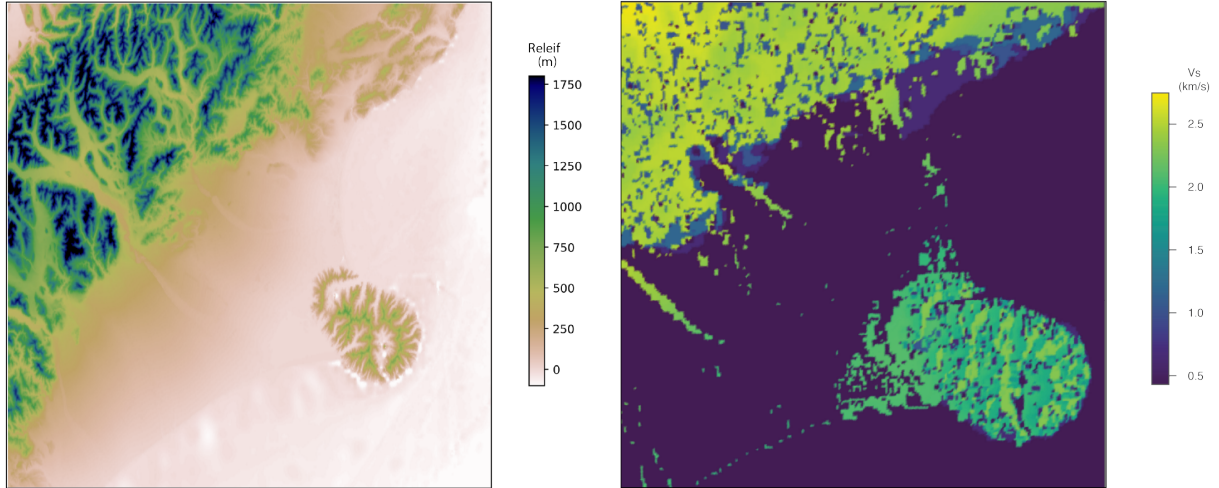
Fig. 35: Surface topography and bathymetry of the region of interest (left), and surface shear wave velocity (Vs) for the same region, as obtained from the South Island Velocity Model (SIVM). The range of the relief in the region covered by the simulation domain is 2,194 m, with a maximum elevation of 1,877 m and a maximum depth at sea of 317 m. In the simulations we consider minimum Vs values of 1,000 m/s for initial test runs, and 500 m/s for the final results.

Computational method of ground motion simulations

Models for the prediction of earthquake ground motions are constructed using two different approaches. One approach is mathematical where a model is based on physical principles and the second approach is empirical where more emphasis is given to fit the model with experimental data rather focusing on the physical insight of the model (Ólafsson et al., 2001; Douglas & Aochi, 2008). The methods using mathematical approach are mostly called physics- based methods. Some of the commonly used physics-based methods including finite difference, finite element and spectral element methods are deterministic methods. This current study utilizes Hercules, a finite element method (FEM) simulation software for anelastic wave propogation developed by the Quake Group at Carnegie Mellon University (Tu et al., 2006; Taborda et al., 2010) to simulate the ground motions of Christchurch area.

FEM methodology

The deterministic physics based methods of ground motion simulation are based on solving the momentum equation that is given as:

$$\rho \ddot{u}_i = \sigma_{ij,j} + f_i \tag{5.1}$$

Here, double-dot above u denotes the second partial derivative with respect to time. The equation is written in Cartesian coordinates where u_i and f_i represent the displacement and the body forces in the i direction. The Cauchy stress tensor is given by σ_{ij} while $\sigma_{ij,j}$ is the space derivative of Cauchy stress tensor w.r.t to j direction and ρ is mass density. This stress tensor is related to the strain tensor ϵ_{pq} through a fourth order tensor as

$$\sigma_{ij} = C_{ijpq}\epsilon_{pq} \tag{5.2}$$

Using symmetry of the stress and strain tensors, and assuming isotropy within the rock, the Cauchy stress tensor can be written in terms of displacements and Lame parameters (λ and μ) as shown in (4)

$$C_{ijpq} = \lambda \delta_{ij}\delta_{pq} + \mu(\delta_{ip}\delta_{jq} + \delta_{iq}\delta_{jp}) \tag{5.3}$$

$$\sigma_{ij} = \lambda \delta_{ij}u_{k,k} + \mu(u_{i,j} + u_{j,i}) \tag{5.4}$$

As described earlier, all the FEM methods including Hercules are based on solving equation (1) with Cauchy stress tensor given by (4). The final momentum equation is converted into weak form using standard Gelerkin method and then problem is discretized in space. This procedure converts the momentum equation into a matrix form as

$$M\ddot{u} + Ku = f \tag{5.5}$$

Here M is the mass matrix and K is the stiffness matrix, the term f on right hand side is the assembled vector of body forces. A detailed description of FEM method with forms of the matrices is provided by Taborda & Roten (2015).

Topographic implementation

FEM schemes have the ability to easily handle sharp interfaces, complex geometries and free-surface boundary conditions as compared to finite difference (FDM) schemes, though the method still requires significant computational resources. For this reason, large-scale ground motion simulation studies typically do not include surface topography but rather perform their simulations by making the free surface flat. This flat free surface is achieved by making the velocity model "squashed" or "bulldozed". For the squashed velocity model case, the topography above a certain elevation (usually sea level) is squeezed into top layer of the velocity model (Quinay et al., 2012). For the bulldozed velocity model case, the topography above a certain elevation is stripped away, and if there are any voids then those are filled with top layer properties (Aagaard et al., 2008). It is important to mention that there is no physical basis for any of these methods.

Recent advancement in computational resources has enabled the ground motions simulation community to incorporate topography into their models. The topographic implementation in Hercules is done using the Virtual Topography approach (Restrepo & Bielak, 2014). This approach consists of two steps. During the first step, the topography above a flat surface is accommodated using an unstructured mesh (cubic elements). In the second step, the cubic elements are subdivided into five tetrahedral elements and then the stiffness matrix of each of the tetrahedral element is scaled using the topographic volume present in this tetrahedron. One advantage of this topographic implementation is that it does not affect the time stepping or the efficiency of the numerical approach. A detailed description of virtual topographic implementation with benchmark problems is provided in Restrepo & Bielak (2014).

Model for simulations

The column labelled 'original running workflow' in Fig. 36 (i.e. original workflow) shows a typical workflow performed during ground motion simulation modeling. A domain size is selected before running a simulation and then simulation parameters are decided. Similarly, a source model, material model and topographic model are selected a *priori* to run a ground motion simulation. The details of each of these is provided below.

Domain size and simulation parameters

One of the important considerations in ground motion simulations is the selection of the dimensions of simulation domain. This dimension is a main factor controlling the size of the problem that is solved during a simulation. Once the dimensions are selected, the next part is to select a source and material model (Taborda & Roten, 2015). We select a domain having a size of 120 km east-west, 120 km north-south, and 60 km in the depth direction for all of our simulations. We select this region so that we can cover the main topographic regions of the central Canterbury region i.e. Peninsula region, plain region and high topographic region. Figure 34 shows the horizontal surface projection of the simulation domain within the South Island (left), and detailed inset of the simulation domain (right). The star indicates the epicenter location of the point source used in our simulations. We select a shear wave velocity of 500 m/sec and a maximum wave frequency of 2 Hz in order to ensure a resonable computational expense for performing the simulation. The outputs of the code are ground displacements, velocity, and accelerations at the provided coordinates of earth surface at any desired sampling frequency. We run our 3D ground motion simulations using elastic material properties and anelastic material properties. The anelastic model uses rayleigh damping to simulate the effects of anelasticity.

Source model

Hercules has the capacity to handle both point as well as extended fault source models. We perform our simulations with a point source approximation. To estimate the source time function, we use a similar formulations to that used in Taborda et al. (2016),

Typical consumption as a percent of total running time

Original Running Workflow

Modified Running Workflow

Simulation Parameters

SIVM Models
– Global Velocity Model
– Tomography Data
– Basin Data
– Surface Data

Material Model Database   Simulation Parameters

Load SIVM data in memory

1 to 2 %   Mesh Generation through iterative querying to a single model database   Mesh Generation

Loop over all the elements at each refinement cycle, and at each coordinate point (x,y,z)

1. Transform coordinates to lat, long, depth
2. Find the sub-model containing the point
3. Compute properties
4. Return properties

Unload SIVM data from memory

1 to 9 %   Source Generation   Source Generation

90 to 98 %   Solving   Solving

3D+T Wavefield
2D+T Planes
1D+T Stations

3D+T Wavefield
2D+T Planes
1D+T Stations

Fig. 36: Simulation stages in Hercules. Left: typical running time-share for the three major computing operations. Center: original running workflow in which Hercules reads information from a single model database on disk during the meshing process. Right: modified running workflow coupling Hercules with the South Island Velocity Model.

which was adapted based on the work by Tinti, Fukuyama, Piatanesi & Cocco (2005). The source slip rate function is expressed as the convolution of triangular function and Yofee function:

$$\dot{s}(t) = D \times (T(t) * Y(t)) \tag{5.6}$$

Here $Y(t)$ is the Yofee function, $T(t)$ is the triangular function and D is the total slip. The symbol '$*$' shows the convolution operator. The slip 'D' is calculated using the moment magnitude relationship $(M/\mu A)$ where the source dimensions are calculated using standard earthquake scaling relations (Wells & Coppersmith, 1994). The rise time associated with $Y(t)$ is estimated using:

$$t_r = \frac{16 l_s c^{0.5}}{7 V_s \pi^{1.5}}. \tag{5.7}$$

Here c is a shape factor equal to the ratio w_s/l_s, where w_s is the width of rupture and l_s is the length of the rupture (both calculated using scaling relationships). It is important to note that above equation is based on a circular source dimension with homogeneous material properties around the source.

The epicenter location of the point source has a latitude 43.50° S and a longitude of 172.80° E. The star in Fig. 34 indicates the epicenter location of the point source used in our simulations. It corresponds to an aftershock of the 2010-2011 Christchurch earthquake sequence, with a magnitude M_w 5.4. The triangles indicate the location of an artificial array of stations used for the analysis of results.

Material model

The Canterbury subsurface geological structure has significantly influenced the surface ground motions in numerous past earthquakes. The sedimentary basins in the region (e.g. Rakaia basin) and subsurface volcanic edifice are among the most dominant features affecting the wave propagation and surface ground motions in the area (Bradley,

2012; Browne et al., 2012). Since an important consideration in running a ground motion simulation is the selection of a realistic material model (Taborda & Roten, 2015), we consider finding a best possible velocity model of the region. There have been many studies (Hicks, 1989; Jongens, 2011; Ghisetti & Sibson, 2012) to investigate the subsurface geological structure of this area which helps in defining a reasonable subsurface approximation of geological structure. A recent study by Lee et al. (2017) combines the above mentioned studies with other data sets from different resources to construct a 3D velocity model of the region. This study was able to reach a very high resolution (~ 10 m) in some areas due to its use of direct field measurement data like seismic reflection data, well log data (from petroleum and water wells), and cone penetration test data. This study provides a detailed velocity model of the region from the basement rock to all the geological rock surfaces overlying it in the region. We use the velocity model of Lee et al. (2017) to define a crustal material model in this study. We define the material model below Moho using different tomographic studies of the region. Our implementation of the material model into Hercules is given in Fig. 36. We modify the original workflow of Hercules to perform a point base query at a given position into the material model of Canterbury as can be seen in the second column of Fig. 36. The shear wave velocity at the surface of our modeling domain can be seen in Fig. 35(b).

Topographic model

The topographic model of the current modeling domain is constructed by combining the New Zealand nationwide digital elevation model and the New Zealand bathymetry contour data using ArcGIS. Our current resolution of the topographic model is 20 m. Figure 35(a) shows the relief of the modeling domain. The total relief of the modeling domain is ~ 3400 m. The north western part of the modeling domain exhibits mostly higher elevations with maximum elevations reaching about 1900 m. The central part of the domain does not show any topography as this is plain region. The south eastern part has

some topography at the Banks Peninsula region where it reaches an elevation of about 900 m.

Results and Discussion

Figure 37 shows the ground motion response for the flat model along the artificial array of stations A-A' (shown in Fig. 34). The ground motions are a result of simulation runs with a maximum frequency of 1 Hz and a minimum velocity of 500 m/sec, and presents only the vertical component of velocity. The seismograms along the stations A-A' in the flat model represents the propagation of the different seismic phases through different sub-surface geological structures of the simulation region with no effect of topography. As expected, the direct P waves arrive first at the station closest from the epicenter (location marked with the star) and then it reaches to other station with some delay based on its epicentral distance (Fig. 37(a)). The wavefield is significantly amplified for the stations present in the middle of the array which can also be seen at seismograms at the middle of Fig. 37(a). This amplification is expected based on the material model of the region as these stations are mainly from the 'plain region', a region dominated by unconsolidated sedimentary rocks and low velocity sediments. The material properties of the region have caused a significant amplification in the velocity response at those stations. Furthermore, the region of low velocity sedimentary cover has also caused resonance in the seismic signal. This resonance can be observed in the signal as a longer duration of signal for stations in the middle of array as compared to the stations present at the region of high elevation (at the left of array AA') or the stations present at the Banks Peninsula which are on the right side of array AA'. Fig. 37(b) shows the peak vertical velocity in the simulation with a flat model. The peak ground velocities are relatively lower in the mountain side and Banks Peninsula while a high value of the seismic velocities is observed in the plain region having sedimentary cover. The region of high amplification is marked in Fig. 37(b) with an arrow and specifies the existence of low velocity sedimentary cover of the region.

Figure 38(a) shows the perturbation seismograms corresponding to the difference

135
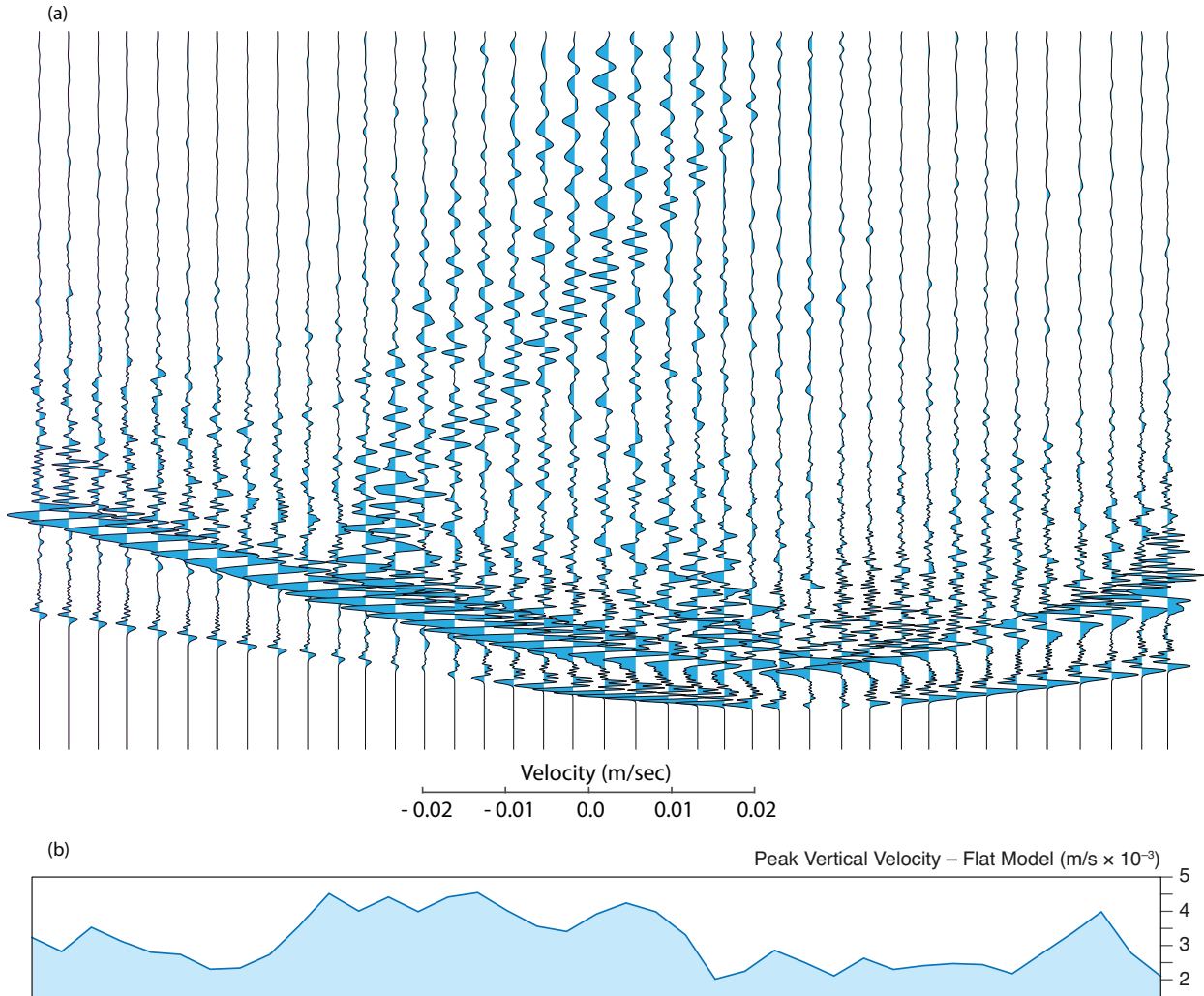
Fig. 37: Peak ground response along the artificial array of stations A-A' shown in Fig. 1 for the flat model. The maximum frequency of simulation is 1 Hz and the minimum shear wave velocity is 1,000 m/s. (a) Vertical velocity seismograms for the flat model. The first seismogram corresponds to the north western station of profile AA' while the last seismogram corresponds to the south eastern station of profile AA'. The seismograms in the middle correspond to the plain area of Canterbury region. (b) Peak vertical velocity in the simulation with a flat model. The peak velocities are relatively high for the stations in the plain region (middle portion). The subsurface geological structure causes an amplification to the wavefield which can be observed by the high values of peak vertical velocity for the middle stations.

between velocity signals of the topography model simulation and those of the flat model simulation along the same profile A-A' shown in Fig. 34. Figure 38(b) shows the peak vertical perturbation velocities and Fig. 38(c) presents the elevation above sea level of the stations along profile A-A'. The amplitudes of perturbation seismograms are visible along the whole profile showing that the topography of a region perturbs the ground motions. This suggests the need to add topography in ground motion simulation models for regions that have diverse topography. Figure 38(b) shows that the region of highest difference between the flat model and the topographic model is at the left and right portion of the profile A-A'. The plain region (center) does not show any significant effect of topography. Based on comparison of Fig. 38(b) and Fig. 38(c), we can clearly observe that the stations that are showing the highest perturbation between the flat model and the topographic model are those which have a higher elevation than the surroundings. This means that Fig. 38(b) and Fig. 38(c) are well correlated suggesting that the location present at higher elevations have a tendency to receive more ground shaking and hence a higher seismic hazard as compared to a location with similar material properties but at zero elevation for a similar magnitude earthquake that occurred at similar distance.

To observe in detail how the seismic signal changes in each region (i.e. the topographic part in the west, the plain part in the center and the Banks Peninsula part in the east) due to topography, we pick four different stations with contrasting topographic locations. The locations of these four stations are marked in Fig. 35(a). Stations P1 and P2 are from the western mountain side, station P3 is from the central plain region and station P4 is from the Banks Peninsula region. The acceleration seismograms at each of these stations are plotted in Fig. 39. These acceleration seismograms are from a run performed with a maximum frequency of 2 Hz and minimum shear wave velocity of 500 m/s. Signals in red correspond to the flat model, whereas the blue signals are from the topography model. All signal are for the NS component of motion. As can be seen, station P1 and P2 accelerograms are different for the topographic model and the flat model. The
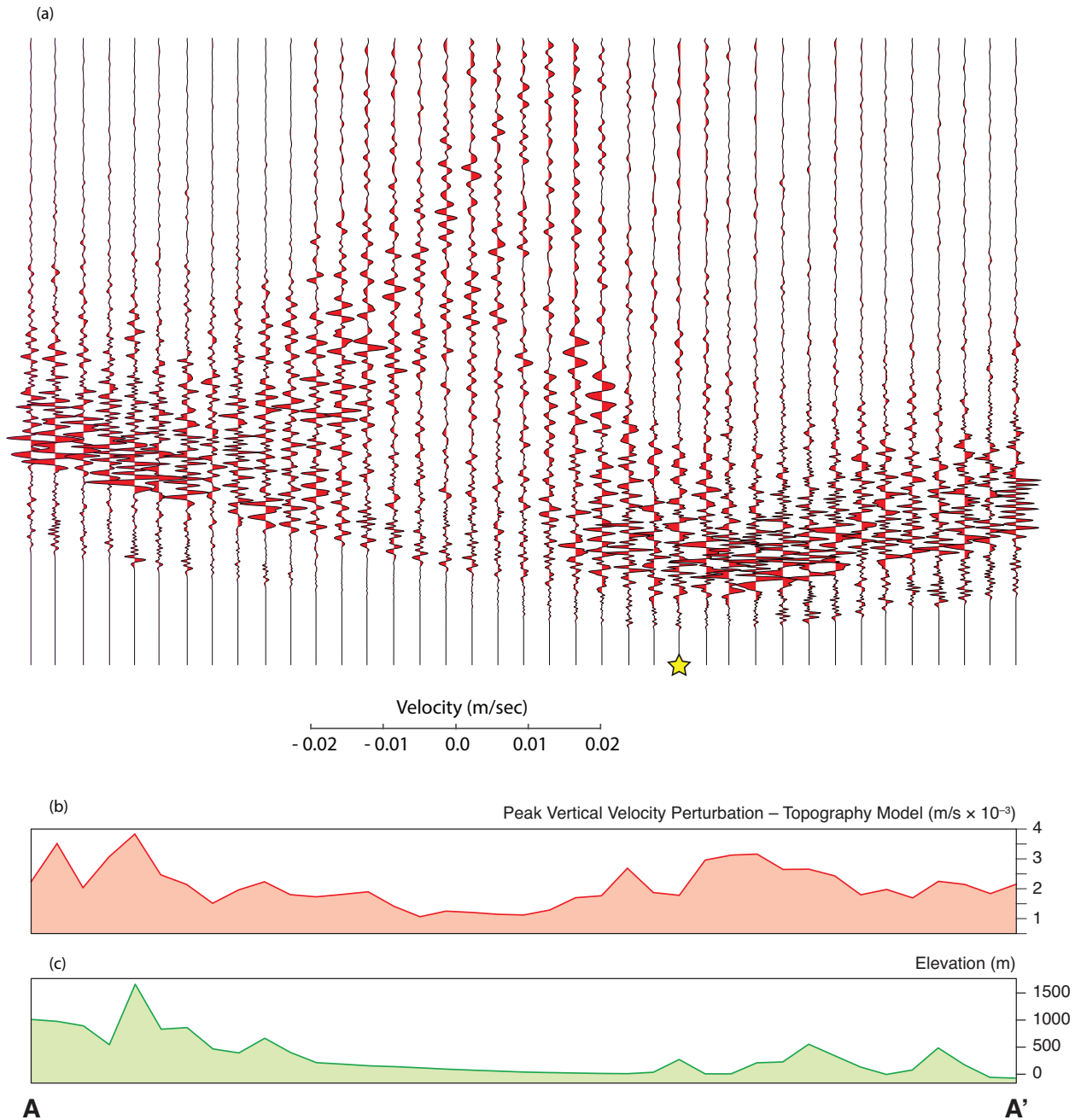
Fig. 38: (a) Perturbation seismograms corresponding to the difference between velocity signals of the topography model simulation and those of the flat model simulation (i.e. Fig. 4). (b) Peak vertical perturbation velocities calculated from (a). The region of highest difference between the flat model and the topographic model is the left and right portion of the profile A-A'. The middle portion (plain region) does not show any significant effect of topography. (c) Elevation above sea level of profile AA'. Based on comparison between (b) and (c), we can observe that the stations that are showing the highest perturbation between the flat model and the topographic model are those which have a higher elevation than the surroundings.

topography has caused an amplification of the ground motion at all of these stations. Similarly, the length of the later part of the signal has also been increased which shows effects of the reverberations and reflections solely due to presence of topography. Station P3 is placed in the region of Central Canterbury plain which does not show any signs of amplification nor any increase in the length of signal. Station P4 also shows some difference between accelerogram of flat and topographic model as the Banks Peninsula region has considerable variation in its topography.

To learn how the amplitude response spectrum compares within both models (i.e. the flat model and the topographic model) for a station placed on a topographic location, we plot the amplitude spectrum for station P1 for both the flat model and the model with topography (shown in Fig. 40). The spectrum for the flat model shows a uni-modal standard form, where the spectrum is flat at lower frequencies and decays at higher frequencies. The spectrum for the case of topographic model is different from that of the flat model. This spectrum is bi-modal, showing peaks at two different frequencies. This implies that there is a higher probability of resonance and seismic hazard for the areas present at topographic relief and hence more consideration should be given to include the topography in ground motion simulations. Furthermore, the flat model spectrum has smaller peak spectrum values as compared to the spectrum of the seismogram of the topographic model.

Figure 41 shows the peak horizontal velocity at the earth surface as a result of simulations performed with a maximum frequency of 1 Hz and a minimum shear velocity of 1000 m/sec. The extent of the figure is the same as our simulation domain. The top figures correspond to peak horizontal velocity at the earth surface for flat model for elastic properties and anelastic properties while the bottom figures show the same but for the case of topographic model. Figure 41(a) shows the case of elastic properties, with no topography, Fig. 41(b) shows the anelastic case with no topography. Figure 41(c) shows the elastic case with topography and Fig. 41(d) shows the anelastic case with topography.
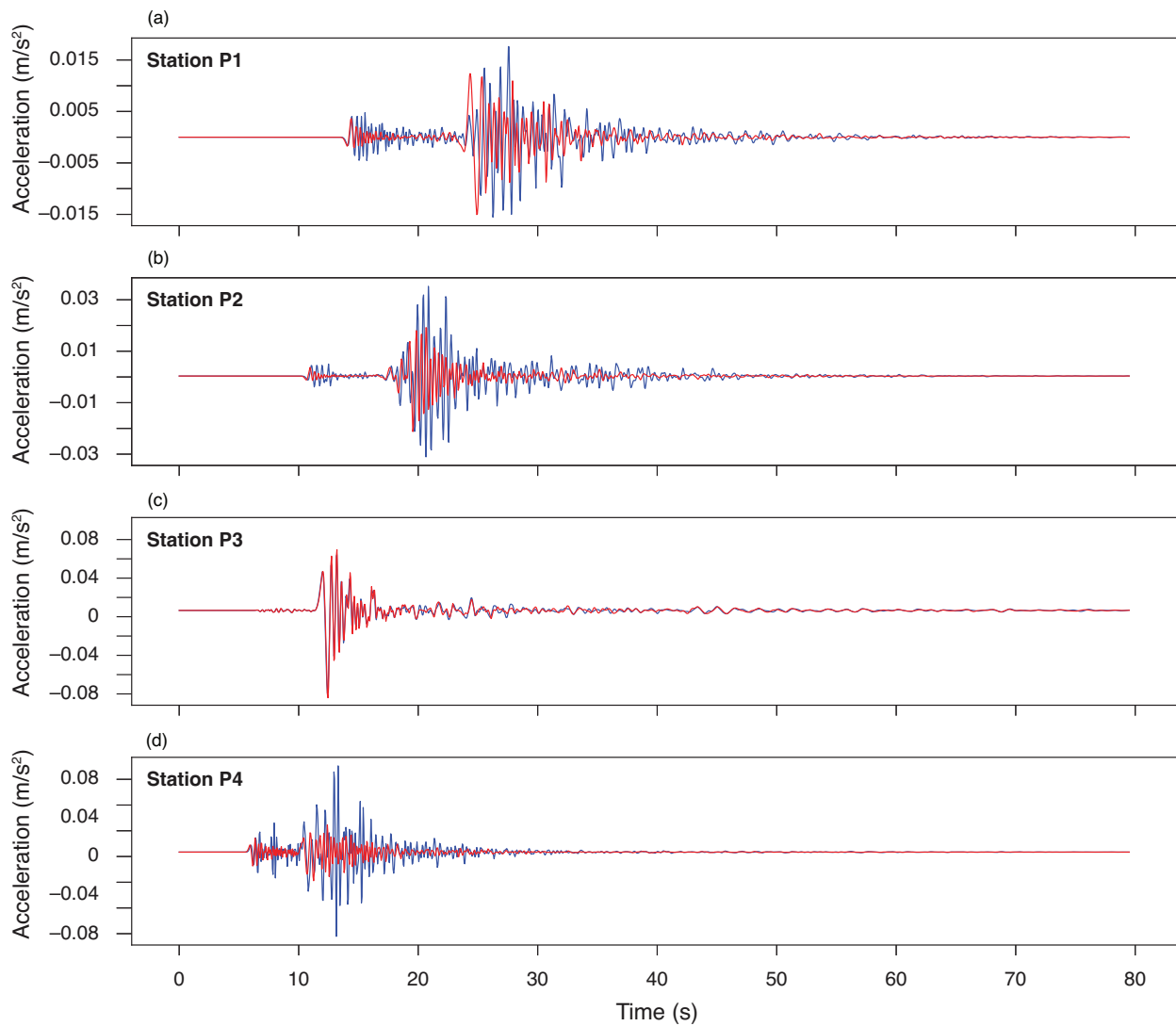
Fig. 39: Acceleration seismograms from the 2 Hz and 500 m/s simulation at the location of the artificial stations P1 through P4 shown in Fig. 2. Signals in red correspond to the flat model, whereas the blue signals are from the topography model. (a) Accelerogram from station P1, (b) accelerogram from station P2, (c) accelerogram from station P3, and (d) accelerogram from station P4.
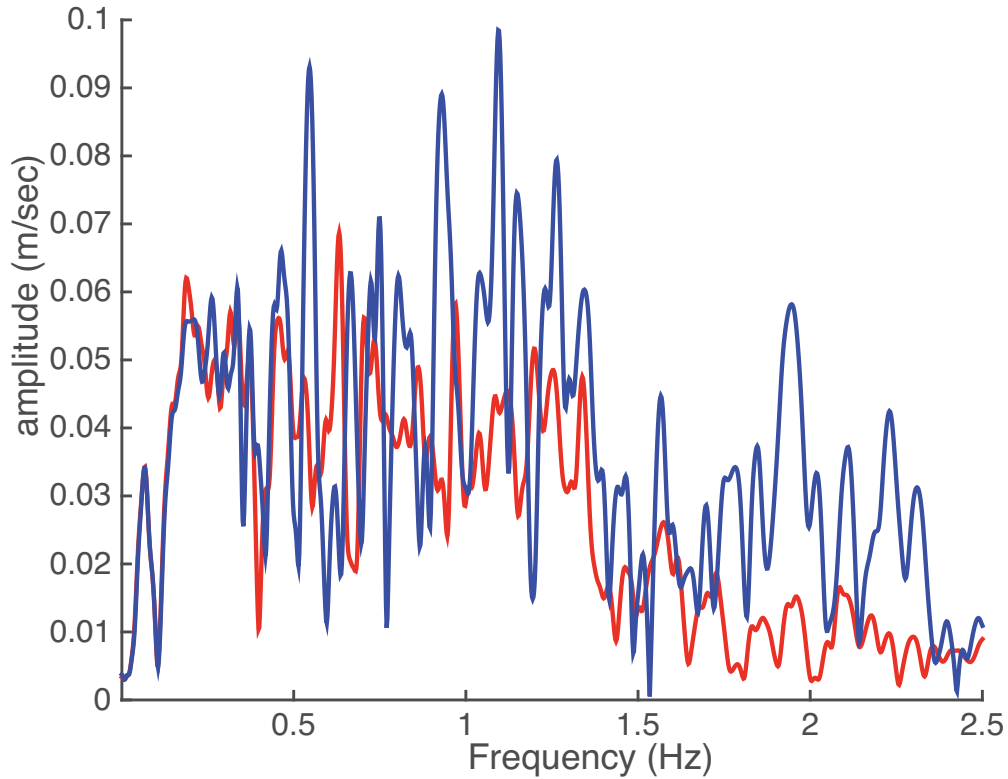
Fig. 40: Velocity spectra for the seismogram shown in Fig. 6(a). The red color spectrum is for the flat model and the blue color spectrum is for the topographic model. The flat model spectrum has lower peak values while the blue color spectrum has higher peak values. The spectrum for the case of flat model shows a uni-modal standard form, where the spectrum is flat at lower frequencies and has a decaying part at relatively higher frequencies. The spectrum for the case of topographic model is different from that of a flat model. This spectrum is bi-modal, showing two different peaks at different respective frequencies. This implies that there is a relatively higher probability of resonance and seismic hazard for the areas present at topographic relief.

Comparing Fig. 41(a) with 41(c), we can clearly observe that the inclusion of the topography causes the amplification of the ground velocities as shown by red and darker colors in the northwest part of the figure where the area is mostly covered by mountainous terrain. This is not obvious when comparing (b) with (d), since the anelastic response has reduced those motion. Comparing 41(a) with 41(b) or 41(c) with 41(d), we can clearly see that the elastic response causes ground motions to be reduced. The region north of the Peninsula has the highest ground motions mainly related to the sedimentary structure lying under that region. We can also observe some reduced ground motions at the south of Peninsula in the case of topographic model as compared to the flat model. The topographic relief causes an increase in ground motions in the northwestern part of the simulation domain (marked in Fig. 41) while a decrease in the ground motions occurs in the southeastern part of simulation domain (marked in Fig. 41). Figure 42 shows the comparison of the anelastic model for a flat model and a topographic model at a maximum frequency of 2 Hz and a minimum shear wave velocity of 500 m/sec. The anomalous region of peak velocity is again prominent in simulations performed with a higher frequency. The ground motions may also have differences in frequency content and duration of the signal when the two simulations (at 1 Hz and 2 Hz) are compared. We suggest that a further study could be done that performs these simulations at higher frequencies ($\sim 5 - 10$ Hz) and then focuses on a detailed comparison of PGV, PGA, frequency content and the duration of ground motion at different frequencies.
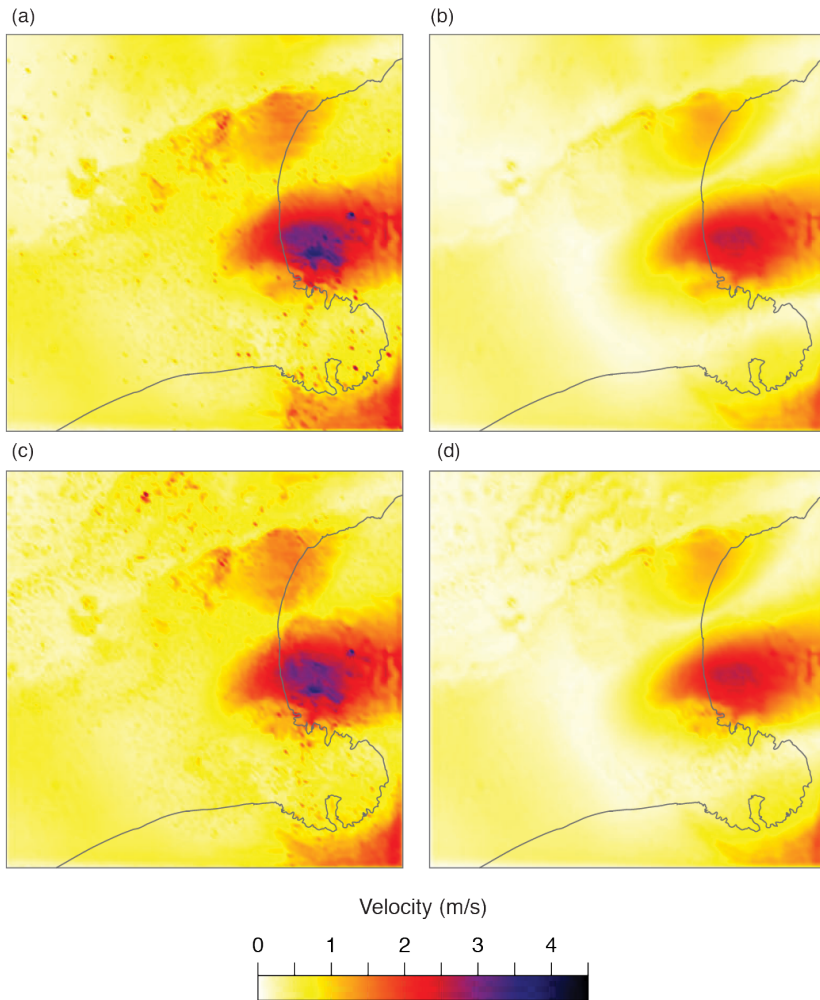
Fig. 41: Results for simulations using different model for a maximum frequency of 1 Hz and minimum shear wave velocity of 1000 m/sec. The color bar shows peak horizontal velocity. The models include with and without topography, and with and without attenuation. (a) Elastic, without topography. (b) Anelastic, without topography. (c) Elastic, with topography. (d) Anelastic, with topography. We can clearly see that the inclusion of the topography causes the amplification of the ground velocities as shown by red and darker colors in the north-west part of the figure where the area is mostly covered by mountainous terrain. This is not that obvious when comparing (b) with (d), since the anelastic response may have reduced those motion. The region north of the Peninsula also has high ground motions mainly related to the sedimentary structure lying under that region. Furthermore, we can observe some reduced ground motions at the south of Peninsula in the case of topographic model as compared to the flat model.
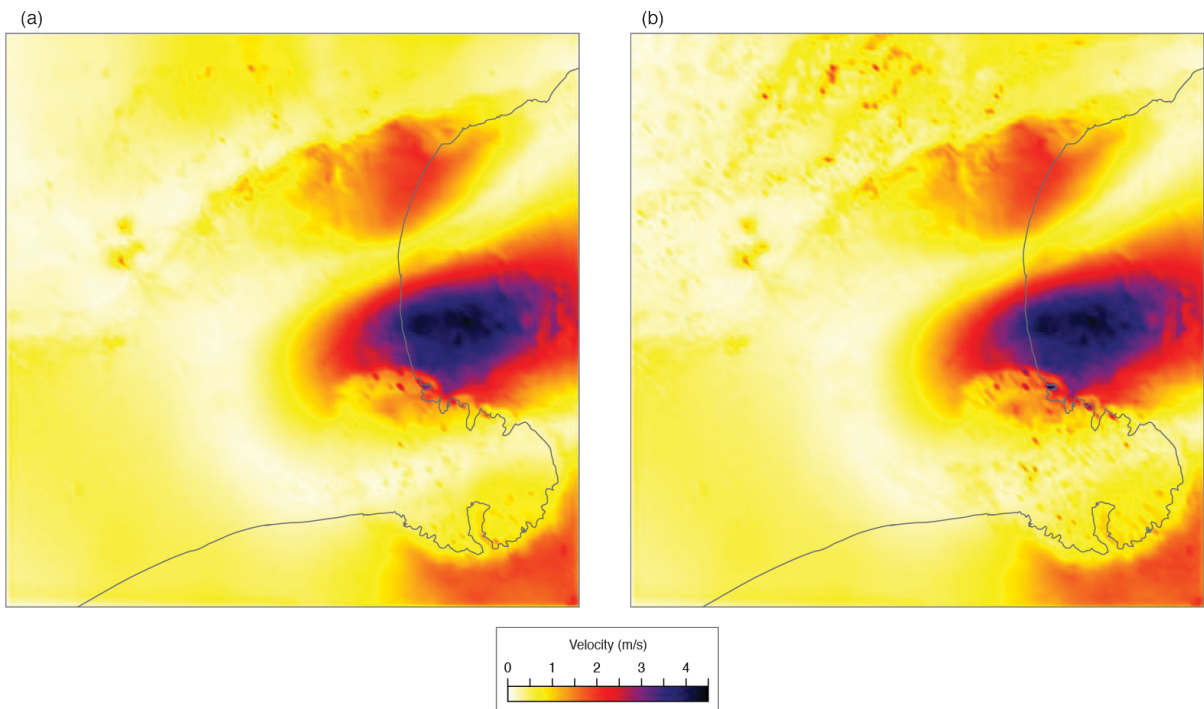
Fig. 42: Peak horizontal velocity for a set of two simulations at a maximum frequency of 2 Hz and a minimum shear wave velocity of 500 m/s, both considering attenuation. (a) Flat model, (b) topography model. The anomalous region of peak velocity is again dominant similar to Fig. 41. The ground motions may also have differences in frequency content and duration of the signal when the two simulations (at 1 Hz and 2 Hz) are compared.

144

Conclusion

We present initial results from an effort to generate earthquake ground motion synthetics for the Canterbury region using 3D simulation techniques considering the effects of the surface topography. We successfully coupled the QuakeCoRE South Island Velocity Model with Hercules and performed a set of simulations with increasing resolution in the maximum frequency and minimum shear wave velocity. Our comparisons of simulation results at maximum frequency of both 1 and 2 Hz reveals that the effects of topography are prominent in the region of topographic variation. This suggests the need to include topography, when the synthetic ground motion simulations are performed. To quantitatively describe the effects of topography on ground motions, we will run similar simulations with an increased maximum frequency (i.e. 4 Hz) and reduced minimum shear wave velocity (i.e. 350 m/s).

Our results show a comparison between flat model and topographic model, as well as a comparison between the elastic model and the anelastic model. The comparisons have given us insights into how the earth surface in Christchurch area may respond to intermediate magnitude earthquakes under the given subsurface geological structure and current surface topography. While all these models have differences in their physics and hence have differences in their output, all of our models suggest that topography is essential to consider into ground motion prediction equations and ground motion simulations of Canterbury region in order to get better estimates of seismic hazard of the area. Future work will make quantitative comparison of the output of each model with seismic observations to examine if these effects can be seen in real data.

Chapter 6

Conclusions

Synopsis

Aftershocks pose hazards to humans due to their tendency to produce strong ground motions. The static stress change mechanism can not explain the triggering of aftershocks in the stress shadows. In this work, we investigate the occurrence of aftershocks, which nucleate in the stress shadows through calculation of CFF zones. We perform simulations of earthquake rupture on rough faults with complex stress distribution in the near-fault region. The earthquake rupture propagation on a rough fault results in heterogeneous slip distribution on the fault. Our CFF calculation shows many small positive CFF zones are present within negative CFF zones in the near-fault region. We suggest that these are the potential locations of those aftershocks, which are observed in stress shadows. The areas where they appear would be seen as stress shadows in typical static stress change calculations due to insufficient resolution of the fault slip. Our results show that the pattern of static stress change is highly complex in the near-fault region. The width of the region of complex stresses depends on the maturity of the fault surface. A more mature fault (with a smaller value of RMS roughness) shows a smaller zone of stress complexity while a young immature fault shows a wider zone of stress complexity. Additionally, our calculations suggest that the PDF of the CFF distribution follows a pattern where a large spread of the CFF values in the near-fault region collapses to a narrow CFF spread at intermediate and far-fault distances.

Our investigation of CFF values from dynamic earthquake rupture simulations on rough faults considering elastic off-fault material properties are based on parallel (to the main fault) receiver fault orientations. Our calculations find, on average, a total number of 15 positive CFF zones in the near-fault region when a 40 km long rupture is considered. These positive CFF zones have at least a diameter of 500 m. This average value (of total positive CFF zones) is many times higher than the positive CFF zones found from the

usual static stress calculations in the near-fault region. The total number of positive zones increase as the distance from main fault decreases. We calculate the areas of the rupture of these positive CFF zones. Our results show that there is a higher probability of occurrence of smaller zones than the probability of occurrence of larger zones in the near-fault region. We compare spatial characteristics of aftershock and preshock data from relocated earthquake of Northern and Southern California. Based on the similarities of behavior of both data sets, we believe that the stress heterogeneities driving their occurrence are similar. This further implies that the stresses in the near-fault region are always heterogeneous irrespective of the phase of an earthquake cycle. Based on our modeling results, we suggest that the locations of small ruptures (either as preshocks or aftershocks) are independent of their timing relative to an earthquake in the near-fault region and are predominately controlled by the stress heterogeneities imposed by fault surface complexity.

We also investigate the CFF values from dynamic earthquake rupture simulations on rough faults considering plastic off-fault material properties. We calculate the CFF values at variable receiver fault orientations determined using the angle at which plastic shear strain is maximum. We observe many more ($\sim$ twice) positive CFF zones in the near-fault region when the off-fault damage is considered. Our comparison of CFF amplitudes as a function of rupture areas suggests that the spatial aftershock distribution surrounding a fault is controlled by both stress heterogeneity as well as the co-seismic damage zone complexity. Based on this, we conclude that the damage zone cannot be neglected when estimating the future hazard and risk estimates of a particular region. Our results suggest that a modification to the classical Coulomb failure function, which considers the damage state of the near-fault region, may provide a better fit to spatial aftershock distribution observed for large earthquakes as compared to classical static stress calculations.

We model the inter-seismic phase of an earthquake on complex fault. Our results show that the heterogeneous stresses and strain introduced in the near-fault region during the co-seismic phase are necessary for the localized shear zones to develop and grow during

147

the inter-seismic phase. A rupture on a flat fault with homogeneous off-fault stress and strain conditions introduced during co-seismic phase does not promote the development and propagation of localized shear zones during inter-seismic phase.

We perform kinematic rupture model simulations of a M_w 5.4 earthquake of Christchurch area, New Zealand. We incorporate surface topography and subsurface geological structure of the region into our model to examine their effects on the surface ground motions within the region. Our results show that the surface ground motions get amplified in the northwestern part of Christchurch, where topographic variations are significant. The duration of the ground shaking also increases in the northwestern part of the region as the topography causes numerous reflections and reverberations of waves. Our results suggest that topography is essential to consider into ground motion prediction equations and ground motion simulations of Christchurch in order to get better estimates of seismic hazard of the region.

Future work

Based on the results of our study, we now have a better understanding of spatial aftershocks distributions and inter-seismic off-fault strain accumulation. Our work opens doors for many future directions that can help scientists better understand the physics of earthquakes. All of our results are based on simulations performed in 2D. For example, future work, which considers 3D earthquake rupture simulations can explore the depth dependence of our model, something that is not currently accounted for in our modeling. The results of these simulations can be compared with observational data to constrain depths of aftershocks observed in the near-fault region. Similarly, those simulations will quantify the effects of fault roughness on aftershock distribution, both along and across the direction of the fault slip. Furthermore, performing simulations in 3D may quantify relationship between the percentage of SSD and the broadening of near-fault aftershock zone for large earthquakes.

We performed all of our simulations with a certain minimum wavelength (~ 100 m)

of the fault profile. A future work with a considerably smaller wavelength can give more interesting insights into the static stress changes in the near-fault region, since the amplitudes of stress perturbations and the resistance to slip will be larger at those shorter wavelengths. Furthermore, we have performed all of our simulations with fractal fault geometry. Additional sources of complexity of fault geometry such as fault bends, kinks, and step-overs etc., also have strong implications for off-fault inelastic deformation (Milliner et al., 2015) as well as rupture propagation (Harris et al., 2018; Lozos et al., 2011). A study similar to ours, considering non-fractal complexity of fault geometry in addition to fractal fault geometry can quantify the effects of large-scale fault geometrical complexity (fault bends, kinks, and step-overs) on spatial aftershock distributions. Similarly, our results of CFF change are based on stress changes that are averaged along strike and over many ruptures. Further work can also be done to assess the comparison of similarities of the predictions for individual events. This work can quantify the level of variability of the stress changes along strike for each individual rupture.

Our coupled simulations of earthquake cycle did not show any particular temporal character (i.e. post-seismic characteristics). We believe that capturing the complex temporal characteristics requires a depth dependent model with appropriate rheologies. A depth-dependent earthquake cycle simulation on rough fault can be performed to delineate the post-seismic characteristics of earthquakes. The results from those simulations can be directly compared with GPS and InSAR measurements of surface displacements from large earthquakes. Furthermore, our coupled model only accounts for a single earthquake cycle (i.e. co-seismic and inter-seismic phase of one earthquake). We do not consider any feedback from quasi-static model (i.e. the inter-seismic phase) into the dynamic rupture model to perform multi-cycle simulations. A study which performs multi-cycle simulations on rough faults can investigate the evolution of near-fault stress complexity over multiple earthquake cycles. This multi-cycle earthquake model will also be able to investigate the changes in the average stress level at which the fault will be capable of hosting big ruptures.

All of the future work mentioned above can further improve our understanding of aftershocks distributions as well as near-fault inelastic deformation. The knowledge of both of these subjects is important in improving hazard estimates of a region. Since numerical modeling has capability to perform simulations with many different initial setups, we hope that this future work may help improve forecasting of off-fault seismicity and improve estimates of seismic hazard in a variety of different tectonic contexts.

REFERENCES

Aagaard, B. T., Brocher, T. M., Dolenc, D., Dreger, D., Graves, R. W., Harmsen, S., Hartzell, S., Larsen, S., McCandless, K., Nilsson, S. et al. (2008), 'Ground-motion modeling of the 1906 San Francisco earthquake, part ii: Ground-motion estimates for the 1906 earthquake and scenario events', *Bulletin of the Seismological Society of America* **98**(2), 1012–1046.

Abercrombie, R. E., Webb, T., Robinson, R., McGinty, P., Mori, J. & Beavan, R. (2000), 'The enigma of the Arthur's Pass, New Zealand, earthquake: 1. reconciling a variety of data for an unusual earthquake sequence', *Journal of Geophysical Research: Solid Earth* **105**(B7), 16119–16137.

Ahamed, S. (2018), Computational Journey Across Multiphysics and Multitemporal Scales: From Slow Tectonic Movement to Fast Earthquake Slip, PhD thesis, The University of Memphis.

Ahamed, S., Daub, E. & Choi, E. (2018), 'Coupling tectonics (submitted)', *Journal of Geophysical Research: Solid Earth* .

Aki, K. (1972), 'Earthquake mechanism', *Tectonophysics* **13**(1-4), 423–446.

Albert, R. A., Phillips, R. J., Dombard, A. J. & Brown, C. D. (2000), 'A test of the validity of yield strength envelopes with an elastoviscoplastic finite element model', *Geophysical Journal International* **140**(2), 399–409.

Allen, C. R., St. Amand, P., Richter, C. & Nordquist, J. (1965), 'Relationship between seismicity and geologic structure in the Southern California region', *Bulletin of the Seismological Society of America* **55**(4), 753–797.

Allison, K. L. & Dunham, E. M. (2018), 'Earthquake cycle simulations with rate-and-state friction and power-law viscoelasticity', *Tectonophysics* **733**, 232–256.

Allmann, B. P. & Shearer, P. M. (2009), 'Global variations of stress drop for moderate to large earthquakes', *Journal of Geophysical Research: Solid Earth* **114**(B1).

Andrews, D. (1976), 'Rupture propagation with finite stress in antiplane strain', *Journal of Geophysical Research* **81**(20), 3575–3582.

Andrews, D. (1985), 'Dynamic plane-strain shear rupture with a slip-weakening friction law calculated by a boundary integral method', *Bulletin of the Seismological Society of America* **75**(1), 1–21.

Andrews, D. (2002), 'A fault constitutive relation accounting for thermal pressurization of pore fluid', *Journal of Geophysical Research: Solid Earth* **107**(B12), ESE–15.

Andrews, D. (2004), 'Rupture models with dynamically determined breakdown displacement', *Bulletin of the Seismological Society of America* **94**(3), 769–775.

Andrews, D. (2005), 'Rupture dynamics with energy loss outside the slip zone', *Journal of Geophysical Research: Solid Earth* **110**(B1).

Andrews, D. & Barall, M. (2011), 'Specifying initial stress for dynamic heterogeneous earthquake source models', *Bulletin of the Seismological Society of America* **101**(5), 2408–2417.

Aochi, H., Fukuyama, E. & Matsu'ura, M. (2000), 'Selectivity of spontaneous rupture propagation on a branched fault', *Geophysical Research Letters* **27**(22), 3635–3638.

Armijo, R., Meyer, B., King, G., Rigo, A. & Papanastassiou, D. (1996), 'Quaternary evolution of the corinth rift and its implications for the late cenozoic evolution of the aegean', *Geophysical Journal International* **126**(1), 11–53.

Aslam, K. S. & Daub, E. G. (2018), 'Effect of fault roughness on aftershock distribution: Elastic off-fault material properties', *Journal of Geophysical Research: Solid Earth*

123(11), 9689–9711.

URL: *https://doi.org/10.1029/2018JB016214*

Aslam, K. S. & Daub, E. G. (2019), 'Effect of fault roughness on aftershock distribution: Plastic off-fault material properties', *Journal of Geophysical Research: Solid Earth* **124**.

URL: *https://doi.org/10.1029/2019JB017392*

Athanasopoulos, G., Pelekis, P. & Xenaki, V. (2001), 'Topography effects in the Athens 1999 earthquake: the case of hotel Dekelia'.

Aviles, C., Scholz, C. & Boatwright, J. (1987), 'Fractal analysis applied to characteristic segments of the San Andreas fault', *Journal of Geophysical Research: Solid Earth* **92**(B1), 331–344.

Bailey, I. & Ben-Zion, Y. (2009), 'Statistics of earthquake stress drops on a heterogeneous fault in an elastic half-space', *Bulletin of the Seismological Society of America* **99**(3), 1786–1800.

Bailey, I. W., Ben-Zion, Y., Becker, T. W. & Holschneider, M. (2010), 'Quantifying focal mechanism heterogeneity for fault zones in Central and Southern California', *Geophysical Journal International* **183**(1), 433–450.

Barber, C. B., Dobkin, D. P. & Huhdanpaa, H. (1996), 'The quickhull algorithm for convex hulls', *ACM Transactions on Mathematical Software (TOMS)* **22**(4), 469–483.

Barbot, S., Fialko, Y. & Bock, Y. (2009), 'Postseismic deformation due to the Mw 6.0 2004 Parkfield earthquake: Stress-driven creep on a fault with spatially variable rate-and-state friction parameters', *Journal of Geophysical Research: Solid Earth* **114**(B7).

Bartholomew, M., Gathright, T. & Henika, W. (1981), 'A tectonic model for the Blue Ridge in central Virginia', *American Journal of Science* **281**(9), 1164–1183.

Bartholomew, M. J. (1987), 'Structural evolution of the Pulaski thrust system, southwestern Virginia', *Geological Society of America Bulletin* **99**(4), 491–510.

Bartholomew, M. J., Whitaker, A. E., Tollo, R., Hibbard, J. & Karabinos, P. (2010), 'The Alleghanian deformational sequence at the foreland junction of the Central and Southern Appalachians', *From Rodinia to Pangea: The Lithotectonic Record of the Appalachian Region: Geological Society of America, Memoir* **206**, 431–454.

Beeler, N., Tullis, T. & Goldsby, D. (2008), 'Constitutive relationships and physical basis of fault strength due to flash heating', *Journal of Geophysical Research: Solid Earth* **113**(B1).

Ben-Zion, Y. & Lyakhovsky, V. (2006), 'Analysis of aftershocks in a lithospheric model with seismogenic zone governed by damage rheology', *Geophysical Journal International* **165**(1), 197–210.

Ben-Zion, Y., Peng, Z., Okaya, D., Seeber, L., Armbruster, J. G., Ozer, N., Michael, A. J., Baris, S. & Aktar, M. (2003), 'A shallow fault-zone structure illuminated by trapped waves in the Karadere–Duzce branch of the North Anatolian Fault, western Turkey', *Geophysical Journal International* **152**(3), 699–717.

Ben-Zion, Y. & Shi, Z. (2005), 'Dynamic rupture on a material interface with spontaneous generation of plastic strain in the bulk', *Earth and Planetary Science Letters* **236**(1-2), 486–496.

Beroza, G. C. & Spudich, P. (1988), 'Linearized inversion for fault rupture behavior: application to the 1984 Morgan Hill, California, earthquake', *Journal of Geophysical Research: Solid Earth* **93**(B6), 6275–6296.

Beroza, G. C. & Zoback, M. D. (1993), 'Mechanism diversity of the Loma Prieta aftershocks and the mechanics of mainshock-aftershock interaction', *Science* **259**(5092), 210–213.

Biegel, R. L. & Sammis, C. G. (2004), 'Relating fault mechanics to fault zone structure', *Adv. Geophys* **47**, 65–111.

Bizzarri, A. (2010), 'How to promote earthquake ruptures: Different nucleation strategies in a dynamic model with slip-weakening friction', *Bulletin of the Seismological Society of America* **100**(3), 923–940.

Bizzarri, A. (2011), 'Dynamic seismic ruptures on melting fault zones', *Journal of Geophysical Research: Solid Earth* **116**(B2).

Bizzarri, A. & Cocco, M. (2005), '3D dynamic simulations of spontaneous rupture propagation governed by different constitutive laws with rake rotation allowed', *Annals of Geophysics* **48**(2).

Bizzarri, A. & Cocco, M. (2006*a*), 'A thermal pressurization model for the spontaneous dynamic rupture propagation on a three-dimensional fault: 1. methodological approach', *Journal of Geophysical Research: Solid Earth* **111**(B5).

Bizzarri, A. & Cocco, M. (2006*b*), 'A thermal pressurization model for the spontaneous dynamic rupture propagation on a three-dimensional fault: 2. traction evolution and dynamic parameters', *Journal of Geophysical Research: Solid Earth* **111**(B5).

Bouchon, M. & Barker, J. S. (1996), 'Seismic response of a hill: the example of Tarzana, California', *Bulletin of the Seismological Society of America* **86**(1A), 66–72.

Bouchon, M. & Karabulut, H. (2008), 'The aftershock signature of supershear earthquakes', *science* **320**(5881), 1323–1325.

Brace, W., Paulding Jr, B. & Scholz, C. (1966), 'Dilatancy in the fracture of crystalline rocks', *Journal of Geophysical Research* **71**(16), 3939–3953.

Brackley, H. (2012), *Review of liquefaction hazard information in Eastern Canterbury,*

including Christchurch City and parts of Selwyn, Waimakariri and Hurunui Districts, Environment Canterbury Regional Council.

Bradley, B. (2012), 'Ground motions observed in the Darfield and Christchurch earthquakes and the importance of local site response effects', *New Zealand journal of geology and geophysics* **55**(3), 279–286.

Bradley, B. A. & Cubrinovski, M. (2011), 'Near-source strong ground motions observed in the 22 February 2011 Christchurch earthquake', *Seismological Research Letters* **82**(6), 853–865.

Bradley, B. A., Quigley, M. C., Van Dissen, R. J. & Litchfield, N. J. (2014), 'Ground motion and seismic source aspects of the Canterbury earthquake sequence', *Earthquake Spectra* **30**(1), 1–15.

Brambati, A., Faccioli, E., Carulli, G., Cucchi, F., Onofri, R., Stefanini, S. & Ulcigrai, F. (1980), 'Studio di microzonazione sismica dellarea di Tarcento (Friuli)', *CLUET, Trieste* .

Brodsky, E. E., Gilchrist, J. J., Sagy, A. & Collettini, C. (2011), 'Faults smooth gradually as a function of slip', *Earth and Planetary Science Letters* **302**(1), 185–193.

Brown, L. J. & Weeber, J. H. (1992), *Geology of the Christchurch urban area: Scale 1: 25,000*, Institute of Geological & Nuclear Sciences.

Brown, S. R. & Scholz, C. H. (1985), 'Broad bandwidth study of the topography of natural rock surfaces', *J. Geophys. Res* **90**(B14), 12575–82.

Browne, G., Field, B., Barrell, D., Jongens, R., Bassett, K. & Wood, R. (2012), 'The geological setting of the Darfield and Christchurch earthquakes', *New Zealand Journal of Geology and Geophysics* **55**(3), 193–197.

Bruhat, L., Fang, Z. & Dunham, E. M. (2016), 'Rupture complexity and the supershear

transition on rough faults', *Journal of Geophysical Research: Solid Earth*
121(1), 210–224.

Bruhn, R. L. (1990), 'The mechanics of earthquakes and faulting', *Science*
250(4988), 1758–1760.

Caine, J. S., Evans, J. P. & Forster, C. B. (1996), 'Fault zone architecture and permeability
structure', *Geology* **24**(11), 1025–1028.

Candela, T., Renard, F., Bouchon, M., Brouste, A., Marsan, D., Schmittbuhl, J. & Voisin,
C. (2009), Characterization of fault roughness at various scales: Implications of
three-dimensional high resolution topography measurements, *in* 'Mechanics, Structure
and Evolution of Fault Zones', Springer, pp. 1817–1851.

Candela, T., Renard, F., Bouchon, M., Schmittbuhl, J. & Brodsky, E. E. (2011), 'Stress
drop during earthquakes: effect of fault roughness scaling', *Bulletin of the Seismological
Society of America* **101**(5), 2369–2387.

Candela, T., Renard, F., Klinger, Y., Mair, K., Schmittbuhl, J. & Brodsky, E. E. (2012),
'Roughness of fault surfaces over nine decades of length scales', *Journal of Geophysical
Research: Solid Earth* **117**(B8).

Celebi, M. (1987), 'Topographical and geological amplifications determined from
strong-motion and aftershock records of the 3 March 1985 Chile earthquake', *Bulletin of
the Seismological Society of America* **77**(4), 1147–1167.

Chen, X., Shearer, P. & Abercrombie, R. (2012), 'Spatial migration of earthquakes within
seismic clusters in Southern California: Evidence for fluid diffusion', *Journal of
Geophysical Research: Solid Earth* **117**(B4).

Chester, F., Chester, J., Kirschner, D., Schulz, S. & Evans, J. (2004), 'Structure of

large-displacement, strike-slip fault zones in the brittle continental crust', *Rheology and Deformation in the Lithosphere at Continental Margins* **1**, 223–260.

Chester, F. & Logan, J. M. (1986), 'Implications for mechanical properties of brittle faults from observations of the Punchbowl fault zone, California', *Pure and Applied Geophysics* **124**(1-2), 79–106.

Chester, F. M. & Chester, J. S. (2000), 'Stress and deformation along wavy frictional faults', *Journal of Geophysical Research: Solid Earth* **105**(B10), 23421–23430.

Chester, F. M., Evans, J. P. & Biegel, R. L. (1993), 'Internal structure and weakening mechanisms of the San Andreas fault', *Journal of Geophysical Research: Solid Earth* **98**(B1), 771–786.

Chiu, H.-C. & Huang, H.-C. (1992), 'Effects of the canyon topography on ground motions at the Feitsui damsite', *Bulletin of the Seismological Society of America* **82**(4), 1646–1660.

Choi, E., Tan, E., Lavier, L. & Calo, V. M. (2013), 'Dynearthsol2d: An efficient unstructured finite element method to study long-term tectonic deformation', *Journal of Geophysical Research: solid earth* **118**(5), 2429–2444.

Cocco, M. & Rice, J. R. (2002), 'Pore pressure and poroelasticity effects in Coulomb stress analysis of earthquake interactions', *Journal of Geophysical Research: Solid Earth* **107**(B2).

Cochran, E. S., Li, Y.-G., Shearer, P. M., Barbot, S., Fialko, Y. & Vidale, J. E. (2009), 'Seismic and geodetic evidence for extensive, long-lived fault damage zones', *Geology* **37**(4), 315–318.

Cowan, H. (1991), 'The north Canterbury earthquake of September 1, 1888', *Journal of the Royal Society of New Zealand* **21**(1), 1–12.

Dalguer, L., Irikura, K. & Riera, J. (2003), 'Simulation of tensile crack generation by three-dimensional dynamic shear rupture propagation during an earthquake', *Journal of Geophysical Research: Solid Earth* **108**(B3).

Daub, E. G. & Carlson, J. M. (2008), 'A constitutive model for fault gouge deformation in dynamic rupture simulations', *Journal of Geophysical Research: Solid Earth* **113**(B12).

Daub, E. G. & Carlson, J. M. (2010), 'Friction, fracture, and earthquakes', *Annu. Rev. Condens. Matter Phys.* **1**(1), 397–418.

Daub, E. G., Manning, M. L. & Carlson, J. M. (2010), 'Pulse-like, crack-like, and supershear earthquake ruptures with shear strain localization', *Journal of Geophysical Research: Solid Earth* **115**(B5).

Day, S. M. (1982), 'Three-dimensional finite difference simulation of fault dynamics: rectangular faults with fixed rupture velocity', *Bulletin of the Seismological Society of America* **72**(3), 705–727.

Di Toro, G., Goldsby, D. L. & Tullis, T. E. (2004), 'Friction falls towards zero in quartz rock as slip velocity approaches seismic rates', *Nature* **427**(6973), 436.

Di Toro, G., Han, R., Hirose, T., De Paola, N., Nielsen, S., Mizoguchi, K., Ferri, F., Cocco, M. & Shimamoto, T. (2011), 'Fault lubrication during earthquakes', *Nature* **471**(7339), 494–498.

Dieterich, J. (1994), 'A constitutive law for rate of earthquake production and its application to earthquake clustering', *Journal of Geophysical Research: Solid Earth* **99**(B2), 2601–2618.

Dieterich, J. H. (1979), 'Modeling of rock friction: 1. experimental results and constitutive equations', *Journal of Geophysical Research: Solid Earth* **84**(B5), 2161–2168.

Dieterich, J. H. (1992), 'Earthquake nucleation on faults with rate-and state-dependent strength', *Tectonophysics* **211**(1-4), 115–134.

Dieterich, J. H. & Smith, D. E. (2009), 'Nonplanar faults: Mechanics of slip and off-fault damage', *Pure and Applied Geophysics* **166**(10-11), 1799–1815.

Doser, D. I., Webb, T. H. & Maunder, D. E. (1999), 'Source parameters of large historical (1918–1962) earthquakes, South Island, New Zealand', *Geophysical Journal International* **139**(3), 769–794.

Douglas, J. & Aochi, H. (2008), 'A survey of techniques for predicting earthquake ground motions for engineering purposes', *Surveys in geophysics* **29**(3), 187–220.

Downes, G. L. (1995), *Atlas of isoseismal maps of New Zealand earthquakes*, Vol. 11, Institute of Geological & Nuclear Sciences Limited.

Duan, B. (2008), 'Effects of low-velocity fault zones on dynamic ruptures with nonelastic off-fault response', *Geophysical Research Letters* **35**(4).

Duan, B. & Oglesby, D. D. (2005*a*), 'The dynamics of thrust and normal faults over multiple earthquake cycles: Effects of dipping fault geometry', *Bulletin of the Seismological Society of America* **95**(5), 1623–1636.

Duan, B. & Oglesby, D. D. (2005*b*), 'Multicycle dynamics of nonplanar strike-slip faults', *Journal of Geophysical Research: Solid Earth* **110**(B3).

Dunham, E. M. & Archuleta, R. J. (2005), 'Near-source ground motion from steady state dynamic rupture pulses', *Geophysical Research Letters* **32**(3).

Dunham, E. M., Belanger, D., Cong, L. & Kozdon, J. E. (2011*a*), 'Earthquake ruptures with strongly rate-weakening friction and off-fault plasticity, part 1: Planar faults', *Bulletin of the Seismological Society of America* **101**(5), 2296–2307.

Dunham, E. M., Belanger, D., Cong, L. & Kozdon, J. E. (2011*b*), 'Earthquake ruptures with strongly rate-weakening friction and off-fault plasticity, part 1: Planar faults', *Bulletin of the Seismological Society of America* **101**(5), 2296–2307.

Dunham, E. M., Belanger, D., Cong, L. & Kozdon, J. E. (2011*c*), 'Earthquake ruptures with strongly rate-weakening friction and off-fault plasticity, part 2: Nonplanar faults', *Bulletin of the Seismological Society of America* **101**(5), 2308–2322.

Dunham, E. M., Belanger, D., Cong, L. & Kozdon, J. E. (2011*d*), 'Earthquake ruptures with strongly rate-weakening friction and off-fault plasticity, part 2: Nonplanar faults', *Bulletin of the Seismological Society of America* **101**(5), 2308–2322.

Ekström, G., Nettles, M. & Dziewoński, A. (2012), 'The global CMT project 2004–2010: Centroid-moment tensors for 13,017 earthquakes', *Physics of the Earth and Planetary Interiors* **200**, 1–9.

El Hariri, M., Abercrombie, R. E., Rowe, C. A. & Do Nascimento, A. F. (2010), 'The role of fluids in triggering earthquakes: observations from reservoir induced seismicity in Brazil', *Geophysical Journal International* **181**(3), 1566–1574.

Erickson, B. A., Dunham, E. M. & Khosravifar, A. (2017), 'A finite difference method for off-fault plasticity throughout the earthquake cycle', *Journal of the Mechanics and Physics of Solids* **109**, 50–77.

Erlingsson, S. & Einarsson, P. (1989), 'Distance changes in the south Iceland seismic zone 1977-1984', *Jökull* (39), 32–40.

Eshelby, J. D. (1957), 'The determination of the elastic field of an ellipsoidal inclusion, and related problems', *Proc. R. Soc. Lond. A* **241**(1226), 376–396.

Fang, Z. & Dunham, E. M. (2013), 'Additional shear resistance from fault roughness and

stress levels on geometrically complex faults', *Journal of Geophysical Research: Solid Earth* **118**(7), 3642–3654.

Faulkner, D., Jackson, C., Lunn, R., Schlische, R., Shipton, Z., Wibberley, C. & Withjack, M. (2010), 'A review of recent developments concerning the structure, mechanics and fluid flow properties of fault zones', *Journal of Structural Geology* **32**(11), 1557–1575.

Faulkner, D., Lewis, A. & Rutter, E. (2003), 'On the internal structure and mechanics of large strike-slip fault zones: field observations of the Carboneras fault in Southeastern Spain', *Tectonophysics* **367**(3-4), 235–251.

Faulkner, D., Mitchell, T., Jensen, E. & Cembrano, J. (2011), 'Scaling of fault damage zones with displacement and the implications for fault growth processes', *Journal of Geophysical Research: Solid Earth* **116**(B5).

Felzer, K. R. & Brodsky, E. E. (2006), 'Decay of aftershock density with distance indicates triggering by dynamic stress', *Nature* **441**(7094), 735.

Fialko, Y. (2004), 'Probing the mechanical properties of seismically active crust with space geodesy: Study of the coseismic deformation due to the 1992 Mw 7. 3 Landers (southern California) earthquake', *Journal of Geophysical Research: Solid Earth* **109**(B3).

Finzi, Y., Hearn, E. H., Ben-Zion, Y. & Lyakhovsky, V. (2009), 'Structural properties and deformation patterns of evolving strike-slip faults: Numerical simulations incorporating damage rheology', *Pure and Applied Geophysics* **166**(10-11), 1537–1573.

Forsyth, P., Barrell, D. & Jongens, R. (2008), 'Geology of the Christchurch Area, Institute of Geological & Nuclear Sciences 1: 250000 geological map 16', *Lower Hutt, New Zealand* .

Freed, A. M. (2005), 'Earthquake triggering by static, dynamic, and postseismic stress transfer', *Annu. Rev. Earth Planet. Sci.* **33**, 335–367.

Freed, A. M. & Bürgmann, R. (2004), 'Evidence of power-law flow in the mojave desert mantle', *Nature* **430**(6999), 548.

Gabriel, A.-A., Ampuero, J.-P., Dalguer, L. & Mai, P. M. (2013), 'Source properties of dynamic rupture pulses with off-fault plasticity', *Journal of Geophysical Research: Solid Earth* **118**(8), 4117–4126.

Gardner, J. & Knopoff, L. (1974), 'Is the sequence of earthquakes in Southern California, with aftershocks removed, Poissonian?', *Bulletin of the Seismological Society of America* **64**(5), 1363–1367.

Geli, L., Bard, P.-Y. & Jullien, B. (1988), 'The effect of topography on earthquake ground motion: a review and new results', *Bulletin of the Seismological Society of America* **78**(1), 42–63.

Gerya, T. V. & Yuen, D. A. (2007), 'Robust characteristics method for modelling multiphase visco-elasto-plastic thermo-mechanical problems', *Physics of the Earth and Planetary Interiors* **163**(1), 83–105.

Ghisetti, F. & Sibson, R. (2012), 'Compressional reactivation of E–W inherited normal faults in the area of the 2010–2011 Canterbury earthquake sequence', *New Zealand Journal of Geology and Geophysics* **55**(3), 177–184.

Gledhill, K., Ristau, J., Reyners, M., Fry, B. & Holden, C. (2011), 'The Darfield (Canterbury, New Zealand) Mw 7.1 earthquake of September 2010: A preliminary seismological report', *Seismological Research Letters* **82**(3), 378–386.

Gledhill, K., Robinson, R., Webb, T., Abercrombie, R., Beavan, J., Cousins, J. & Eberhart-Phillips, D. (2000), 'The MW 6.2 Cass, New Zealand, earthquake of 24 November 1995: Reverse faulting in a strike-slip region', *New Zealand Journal of Geology and Geophysics* **43**(2), 255–269.

Goldsby, D. L. & Tullis, T. E. (2002), 'Low frictional strength of quartz rocks at subseismic slip rates', *Geophysical Research Letters* **29**(17).

Goldsby, D. L. & Tullis, T. E. (2011), 'Flash heating leads to low frictional strength of crustal rocks at earthquake slip rates', *Science* **334**(6053), 216–218.

Gomberg, J., Bodin, P. & Reasenberg, P. A. (2003), 'Observing earthquakes triggered in the near field by dynamic deformations', *Bulletin of the Seismological Society of America* **93**(1), 118–138.

Gonzalez-Ortega, A., Fialko, Y., Sandwell, D., Nava-Pichardo, F. A., Fletcher, J., Gonzalez-Garcia, J., Lipovsky, B., Floyd, M. & Funning, G. (2014), 'El Mayor-Cucapah (Mw 7.2) earthquake: Early near-field postseismic deformation from InSAR and GPS observations', *Journal of Geophysical Research: Solid Earth* **119**(2), 1482–1497.

Graham, I. J. (2008), *A continent on the move: New Zealand geoscience into the 21st century*, Geological Society of New Zealand.

Gray, D. R. (1981), 'Compound tectonic fabrics in singly folded rocks from Southwest Virginia USA', *Tectonophysics* **78**(1-4), 229–248.

Gupta, H. K. (2002), 'A review of recent studies of triggered earthquakes by artificial water reservoirs with special emphasis on earthquakes in Koyna, India', *Earth-Science Reviews* **58**(3-4), 279–310.

Gutenberg, B. & Richter, C. F. (1944), 'Frequency of earthquakes in California', *Bulletin of the Seismological Society of America* **34**(4), 185–188.

Hainzl, S. (2004), 'Seismicity patterns of earthquake swarms due to fluid intrusion and stress triggering', *Geophysical Journal International* **159**(3), 1090–1096.

Hainzl, S., Zoeller, G. & Wang, R. (2010), 'Impact of the receiver fault distribution on aftershock activity', *Journal of Geophysical Research: Solid Earth* **115**(B5).

Hamiel, Y. & Fialko, Y. (2007), 'Structure and mechanical properties of faults in the North Anatolian Fault system from InSAR observations of coseismic deformation due to the 1999 Izmit (Turkey) earthquake', *Journal of Geophysical Research: Solid Earth* **112**(B7).

Han, R., Shimamoto, T., Hirose, T., Ree, J.-H. & Ando, J.-i. (2007), 'Ultralow friction of carbonate faults caused by thermal decomposition', *Science* **316**(5826), 878–881.

Hanks, T. C. (1977), Earthquake stress drops, ambient tectonic stresses and stresses that drive plate motions, *in* 'Stress in the Earth', Springer, pp. 441–458.

Hanks, T. C. (1992), 'Small earthquakes, tectonic forces', *Science* **256**(5062), 1430–1432.

Hanks, T. C. & Bakun, W. H. (2002), 'A bilinear source-scaling model for M-log A observations of continental earthquakes', *Bulletin of the Seismological Society of America* **92**(5), 1841–1846.

Hanks, T. C. & Bakun, W. H. (2008), 'M-log A observations for recent large earthquakes', *Bulletin of the Seismological Society of America* **98**(1), 490–494.

Hardebeck, J. (2010), 'Aftershocks are well aligned with the background stress field, contradicting the hypothesis of highly heterogeneous crustal stress', *Journal of Geophysical Research: Solid Earth* **115**(B12).

Hardebeck, J. L. (2015), 'Comment on models of stochastic, spatially varying stress in the crust compatible with focal-mechanism data, and how stress inversions can be biased toward the stress rate by Deborah Elaine Smith and Thomas H. Heaton', *Bulletin of the Seismological Society of America* **105**(1), 447–451.

Hardebeck, J. L., Nazareth, J. J. & Hauksson, E. (1998), 'The static stress change triggering model: Constraints from two Southern California aftershock sequences', *Journal of Geophysical Research: Solid Earth* **103**(B10), 24427–24437.

Hardebeck, J. L. & Shearer, P. M. (2002), 'A new method for determining first-motion focal mechanisms', *Bulletin of the Seismological Society of America* **92**(6), 2264–2276.

Harris, R. A. (2004), Numerical simulations of large earthquakes: Dynamic rupture propagation on heterogeneous faults, *in* 'Computational Earthquake Science Part II', Springer, pp. 2171–2181.

Harris, R. A. & Day, S. M. (1997), 'Effects of a low-velocity zone on a dynamic rupture', *Bulletin of the Seismological Society of America* **87**(5), 1267–1280.

Harris, R. A. & Simpson, R. W. (1992), 'Changes in static stress on Southern California faults after the 1992 Landers earthquake', *Nature* **360**(6401), 251.

Harris, R., Barall, M., Archuleta, R., Dunham, E., Aagaard, B., Ampuero, J., Bhat, H., Cruz-Atienza, V., Dalguer, L., Dawson, P. et al. (2009), 'The SCEC/USGS dynamic earthquake rupture code verification exercise', *Seismological Research Letters* **80**(1), 119–126.

Harris, R., Barall, M., Archuleta, R., Dunham, E., Aagaard, B., Ampuero, J., Bhat, H., Cruz-Atienza, V., Dalguer, L., Dawson, P. et al. (2018), 'A suite of exercises for verifying dynamic earthquake rupture codes', *Seismological Research Letters* **89**(3), 1146–1162.
URL: *https://doi.org/10.1785/0220170222*

Hartzell, S. H., Carver, D. L. & King, K. W. (1994), 'Initial investigation of site and topographic effects at Robinwood Ridge, California', *Bulletin of the Seismological Society of America* **84**(5), 1336–1349.

Hartzell, S., Liu, P. & Mendoza, C. (1996), 'The 1994 Northridge, California, earthquake: Investigation of rupture velocity, risetime, and high-frequency radiation', *Journal of Geophysical Research: Solid Earth* **101**(B9), 20091–20108.

Hauksson, E. (2010), Spatial separation of large earthquakes, aftershocks, and background seismicity: Analysis of interseismic and coseismic seismicity patterns in southern California, *in* 'Seismogenesis and Earthquake Forecasting: The Frank Evison Volume II', Springer, pp. 125–143.

Hauksson, E. (2011), 'Crustal geophysics and seismicity in southern California', *Geophysical Journal International* **186**(1), 82–98.

Helmstetter, A., Kagan, Y. Y. & Jackson, D. D. (2005), 'Importance of small earthquakes for stress transfers and earthquake triggering', *Journal of Geophysical Research: Solid Earth* **110**(B5).

Hicks, S. (1989), *Structure of the Canterbury Plains, New Zealand, from gravity modelling*, Geophysics Division, Department of Scientific and Industrial Research.

Hill, D. P., Pollitz, F. & Newhall, C. (2002), 'Earthquake-volcano interactions', *Physics Today* **55**(11), 41–47.

Hill, D., Reasenberg, P., Michael, A., Arabaz, W., Beroza, G., Brumbaugh, D., Brune, J., Castro, R., Davis, S., Ellsworth, W. et al. (1993), 'Seismicity remotely triggered by the magnitude 7.3 Landers, California, earthquake', *Science* **260**(5114), 1617–1623.

Hirose, T. & Bystricky, M. (2007), 'Extreme dynamic weakening of faults during dehydration by coseismic shear heating', *Geophysical Research Letters* **34**(14).

Hirose, T. & Shimamoto, T. (2005), 'Growth of molten zone as a mechanism of slip weakening of simulated faults in gabbro during frictional melting', *Journal of Geophysical Research: Solid Earth* **110**(B5).

Hirth, G. & Tullis, J. (1992), 'Dislocation creep regimes in quartz aggregates', *Journal of Structural Geology* **14**(2), 145–159.

Hobbs, B. E., Regenauer-Lieb, K. & Ord, A. (2009), 'Folding with thermal-mechanical feedback: A reply', *Journal of structural geology* **31**(7), 752–755.

Hobbs, B., Regenauer-Lieb, K. & Ord, A. (2008), 'Folding with thermal–mechanical feedback', *Journal of Structural Geology* **30**(12), 1572–1592.

Huang, B.-S. (2000), 'Two-dimensional reconstruction of the surface ground motions of an earthquake: The September 21, 1999, Chi-Chi, Taiwan earthquake', *Geophysical research letters* **27**(18), 3025–3028.

Ida, Y. (1972), 'Cohesive force across the tip of a longitudinal-shear crack and Griffith's specific surface energy', *Journal of Geophysical Research* **77**(20), 3796–3805.

Ionescu, I. R. & Campillo, M. (1999), 'Influence of the shape of the friction law and fault finiteness on the duration of initiation', *Journal of Geophysical Research: Solid Earth* **104**(B2), 3013–3024.

Jaeger, J. C., Cook, N. G. & Zimmerman, R. (2009), *Fundamentals of rock mechanics*, John Wiley & Sons.

Jiang, J. & Lapusta, N. (2016), 'Deeper penetration of large earthquakes on seismically quiescent faults', *Science* **352**(6291), 1293–1297.

Johri, M., Dunham, E. M., Zoback, M. D. & Fang, Z. (2014), 'Predicting fault damage zones by modeling dynamic rupture propagation and comparison with field observations', *Journal of Geophysical Research: Solid Earth* **119**(2), 1251–1272.

Jongens, R. (2011), 'Contours for the base of Quaternary sediments under the Canterbury Plains between the Ashley and Rakaia rivers', *GNS Science Consultancy Report* **132**, 17.

Kagan, Y. Y. (1994), 'Distribution of incremental static stress caused by earthquakes', *Nonlinear Processes in Geophysics* **1**(2/3), 172–181.

Kaiser, A., Holden, C., Beavan, J., Beetham, D., Benites, R., Celentano, A., Collett, D., Cousins, J., Cubrinovski, M., Dellow, G. et al. (2012), 'The Mw 6.2 Christchurch earthquake of February 2011: preliminary report', *New Zealand journal of geology and geophysics* **55**(1), 67–90.

Kaneko, Y. & Fialko, Y. (2011), 'Shallow slip deficit due to large strike-slip earthquakes in dynamic rupture simulations with elasto-plastic off-fault response', *Geophysical Journal International* **186**(3), 1389–1403.

Kato, N. & Seno, T. (2003), 'Hypocenter depths of large interplate earthquakes and their relation to seismic coupling', *Earth and Planetary Science Letters* **210**(1), 53–63.

Kilb, D., Ellis, M., Gomberg, J. & Davis, S. (1997), 'On the origin of diverse aftershock mechanisms following the 1989 Loma Prieta earthquake', *Geophysical Journal International* **128**(3), 557–570.

King, G. C., Hubert-Ferrari, A., Nalbant, S. S., Meyer, B., Armijo, R. & Bowman, D. (2001), 'Coulomb interactions and the 17 August 1999 Izmit, Turkey earthquake', *Comptes Rendus de l'Académie des Sciences-Series IIA-Earth and Planetary Science* **333**(9), 557–569.

King, G. C., Stein, R. S. & Lin, J. (1994), 'Static stress changes and the triggering of earthquakes', *Bulletin of the Seismological Society of America* **84**(3), 935–953.

Komatitsch, D., Liu, Q., Tromp, J., Suss, P., Stidham, C. & Shaw, J. H. (2004), 'Simulations of ground motion in the Los Angeles basin based upon the spectral-element method', *Bulletin of the Seismological Society of America* **94**(1), 187–206.

Kozdon, J. E., Dunham, E. M. & Nordström, J. (2012), 'Interaction of waves with frictional interfaces using summation-by-parts difference operators: Weak enforcement of nonlinear boundary conditions', *Journal of Scientific Computing* **50**(2), 341–367.

Kozdon, J. E., Dunham, E. M. & Nordström, J. (2013), 'Simulation of dynamic earthquake ruptures in complex geometries using high-order finite difference methods', *Journal of Scientific Computing* **55**(1), 92–124.

Kyriakopoulos, C., Oglesby, D., Rockwell, T., Meltzner, A., Barall, M., Fletcher, J. & Tulanowski, D. (2019), 'Dynamic rupture scenarios in the Brawley Seismic Zone, Salton Trough, Southern California', *Journal of Geophysical Research: Solid Earth* .

Lapusta, N. & Rice, J. R. (2003), 'Nucleation and early seismic propagation of small and large events in a crustal earthquake model', *Journal of Geophysical Research: Solid Earth* **108**(B4).

Lapusta, N., Rice, J. R., Ben-Zion, Y. & Zheng, G. (2000), 'Elastodynamic analysis for slow tectonic loading with spontaneous rupture episodes on faults with rate-and state-dependent friction', *Journal of Geophysical Research: Solid Earth* **105**(B10), 23765–23789.

Lee, J.-J. & Bruhn, R. L. (1996), 'Structural anisotropy of normal fault surfaces', *Journal of Structural Geology* **18**(8), 1043–1059.

Lee, R. L., Bradley, B. A., Ghisetti, F. C. & Thomson, E. M. (2017), 'Development of a 3D Velocity Model of the Canterbury, New Zealand, Region for Broadband Ground-Motion Simulation', *Bulletin of the Seismological Society of America* **107**(5), 2131–2150.

Lee, S.-J., Chan, Y.-C., Komatitsch, D., Huang, B.-S. & Tromp, J. (2009), 'Effects of realistic surface topography on seismic ground motion in the Yangminshan region of Taiwan based upon the spectral-element method and LiDAR DTM', *Bulletin of the Seismological Society of America* **99**(2A), 681–693.

Levret, A., Loup, C. & Goula, X. (1988), 'The provence earthquake of 11th June 1909 (France). a new assessment of near field effects', *Modern Approaches in Geophysics* pp. 383–399.

Lin, J. & Stein, R. S. (2004), 'Stress triggering in thrust and subduction earthquakes and stress interaction between the Southern San Andreas and nearby thrust and strike-slip faults', *Journal of Geophysical Research: Solid Earth* **109**(B2).

Lippiello, E., Giacco, F., Marzocchi, W., Godano, C. & De Arcangelis, L. (2015), 'Mechanical origin of aftershocks', *Scientific reports* **5**, 15560.

Liseikin, V. D. (2009), *Grid generation methods*, Springer Science & Business Media.

Liu, J., Sieh, K. & Hauksson, E. (2003), 'A structural interpretation of the aftershock cloud of the 1992 Mw 7.3 Landers earthquake', *Bulletin of the Seismological Society of America* **93**(3), 1333–1344.

Lohman, R. B. & McGuire, J. J. (2007), 'Earthquake swarms driven by aseismic creep in the Salton Trough, California', *Journal of Geophysical Research: Solid Earth* **112**(B4).

Lozos, J. C., Oglesby, D. D., Duan, B. & Wesnousky, S. G. (2011), 'The effects of double fault bends on rupture propagation: A geometrical parameter study', *Bulletin of the Seismological Society of America* **101**(1), 385–398.

Lyakhovsky, V., Ben-Zion, Y. & Agnon, A. (2005), 'A viscoelastic damage rheology and rate-and state-dependent friction', *Geophysical Journal International* **161**(1), 179–190.

Ma, S. & Andrews, D. (2010), 'Inelastic off-fault response and three-dimensional dynamics of earthquake rupture on a strike-slip fault', *Journal of Geophysical Research: Solid Earth* **115**(B4).

Ma, S. & Beroza, G. C. (2008), 'Rupture dynamics on a bimaterial interface for dipping faults', *Bulletin of the Seismological Society of America* **98**(4), 1642–1658.

Mai, P. M., Spudich, P. & Boatwright, J. (2005), 'Hypocenter locations in finite-source rupture models', *Bulletin of the Seismological Society of America* **95**(3), 965–980.

Mai, P. M. & Thingbaijam, K. (2014), 'Srcmod: An online database of finite-fault rupture models', *Seismological Research Letters* **85**(6), 1348–1357.

Mallman, E. P. & Parsons, T. (2008), 'A global search for stress shadows', *Journal of Geophysical Research: Solid Earth* **113**(B12).

Marsan, D. (2005), 'The role of small earthquakes in redistributing crustal elastic stress', *Geophysical Journal International* **163**(1), 141–151.

Meier, M.-A., Werner, M., Woessner, J. & Wiemer, S. (2014), 'A search for evidence of secondary static stress triggering during the 1992 Mw7. 3 Landers, California, earthquake sequence', *Journal of Geophysical Research: Solid Earth* **119**(4), 3354–3370.

Michele, M., Di Stefano, R., Chiaraluce, L., Cattaneo, M., De Gori, P., Monachesi, G., Latorre, D., Marzorati, S., Valoroso, L., Ladina, C. et al. (2016), 'The Amatrice 2016 seismic sequence: a preliminary look at the mainshock and aftershocks distribution', *Annals of Geophysics* **59**.

Milliner, C. W., Dolan, J. F., Hollingsworth, J., Leprince, S., Ayoub, F. & Sammis, C. G. (2015), 'Quantifying near-field and off-fault deformation patterns of the 1992 Mw 7.3 Landers earthquake', *Geochemistry, Geophysics, Geosystems* **16**(5), 1577–1598.

Mogi, K. (1971), 'Fracture and flow of rocks under high triaxial compression', *Journal of Geophysical Research* **76**(5), 1255–1269.

Mogi, K. (1972), Fracture and flow of rocks, *in* 'Developments in Geotectonics', Vol. 4, Elsevier, pp. 541–568.

Mogi, K. (1974), 'On the pressure dependence of strength of rocks and the Coulomb fracture criterion', *Tectonophysics* **21**(3), 273–285.

Myers, R. & Aydin, A. (2004), 'The evolution of faults formed by shearing across joint zones in sandstone', *Journal of Structural Geology* **26**(5), 947–966.

Nandan, S., Ouillon, G., Woessner, J., Sornette, D. & Wiemer, S. (2016), 'Systematic assessment of the static stress triggering hypothesis using interearthquake time statistics', *Journal of Geophysical Research: Solid Earth* **121**(3), 1890–1909.

Nielsen, S. B. & Knopoff, L. (1998), 'The equivalent strength of geometrical barriers to earthquakes', *Journal of Geophysical Research: Solid Earth* **103**(B5), 9953–9965.

Noda, H., Dunham, E. M. & Rice, J. R. (2009), 'Earthquake ruptures with thermal weakening and the operation of major faults at low overall stress levels', *Journal of Geophysical Research: Solid Earth* **114**(B7).

Nur, A. & Booker, J. R. (1972), 'Aftershocks caused by pore fluid flow?', *Science* **175**(4024), 885–887.

Oglesby, D. D. & Mai, P. M. (2012), 'Fault geometry, rupture dynamics and ground motion from potential earthquakes on the North Anatolian Fault under the Sea of Marmara', *Geophysical Journal International* **188**(3), 1071–1087.

Okubo, P. G. (1989), 'Dynamic rupture modeling with laboratory-derived constitutive relations', *Journal of Geophysical Research: Solid Earth* **94**(B9), 12321–12335.

Okubo, P. G. & Aki, K. (1987), 'Fractal geometry in the San Andreas fault system', *Journal of Geophysical Research: Solid Earth* **92**(B1), 345–355.

Ólafsson, S., Remseth, S. & Sigbjörnsson, R. (2001), 'Stochastic models for simulation of strong ground motion in Iceland', *Earthquake engineering & structural dynamics* **30**(9), 1305–1331.

Pankow, K. L., Arabasz, W. J., Pechmann, J. C. & Nava, S. J. (2004), 'Triggered seismicity in Utah from the 3 November 2002 Denali fault earthquake', *Bulletin of the Seismological Society of America* **94**(6B), S332–S347.

Paolucci, R. (2002), 'Amplification of earthquake ground motion by steep topographic irregularities', *Earthquake engineering & structural dynamics* **31**(10), 1831–1853.

Parsons, T., Stein, R. S., Simpson, R. W. & Reasenberg, P. A. (1999), 'Stress sensitivity of fault seismicity: A comparison between limited-offset oblique and major strike-slip faults', *Journal of Geophysical Research: Solid Earth* **104**(B9), 20183–20202.

Pedersen, R., Jónsson, S., Árnadóttir, T., Sigmundsson, F. & Feigl, K. L. (2003), 'Fault slip distribution of two June 2000 Mw 6. 5 earthquakes in South Iceland estimated from joint inversion of InSAR and GPS measurements', *Earth and Planetary Science Letters* **213**(3-4), 487–502.

Peng, Z., Ben-Zion, Y., Michael, A. J. & Zhu, L. (2003), 'Quantitative analysis of seismic fault zone waves in the rupture zone of the 1992 Landers, California, earthquake: evidence for a shallow trapping structure', *Geophysical Journal International* **155**(3), 1021–1041.

Perfettini, H. & Avouac, J.-P. (2004), 'Postseismic relaxation driven by brittle creep: A possible mechanism to reconcile geodetic measurements and the decay rate of aftershocks, application to the Chi-Chi earthquake, Taiwan', *Journal of Geophysical Research: Solid Earth* **109**(B2).

Pettinga, J. R., Yetton, M. D., Van Dissen, R. J. & Downes, G. (2001), 'Earthquake source identification and characterisation for the Canterbury region, South Island, New Zealand'.

Poliakov, A. N. & Buck, W. R. (1998), 'Mechanics of stretching elastic-plastic-viscous layers: Applications to slow-spreading mid-ocean ridges', *GEOPHYSICAL MONOGRAPH-AMERICAN GEOPHYSICAL UNION* **106**, 305–324.

Poliakov, A. N., Dmowska, R. & Rice, J. R. (2002), 'Dynamic shear rupture interactions

with fault bends and off-axis secondary faulting', *Journal of Geophysical Research: Solid Earth* **107**(B11).

Popov, A. & Sobolev, S. (2008), 'Slim3d: A tool for three-dimensional thermomechanical modeling of lithospheric deformation with elasto-visco-plastic rheology', *Physics of the Earth and Planetary Interiors* **171**(1), 55–75.

Potter, S., Becker, J., Johnston, D. & Rossiter, K. (2015), 'An overview of the impacts of the 2010-2011 canterbury earthquakes', *International Journal of Disaster Risk Reduction* **14**, 6–14.

Powell, R. E. & Weldon, R. J. (1992), 'Evolution of the San Andreas fault', *Annual Review of Earth and Planetary Sciences* **20**(1), 431–468.

Power, W. L., Tullis, T. E. & Weeks, J. D. (1988), 'Roughness and wear during brittle faulting', *Journal of Geophysical Research: Solid Earth* **93**(B12), 15268–15278.

Power, W. & Tullis, T. (1995), Review of the fractal character of natural fault surfaces with implications for friction and the evolution of fault zones, *in* 'Fractals in the Earth Sciences', Springer, pp. 89–105.

Power, W., Tullis, T., Brown, S., Boitnott, G. & Scholz, C. (1987), 'Roughness of natural fault surfaces', *Geophysical Research Letters* **14**(1), 29–32.

Powers, P. M. & Jordan, T. H. (2010), 'Distribution of seismicity across strike-slip faults in California', *Journal of Geophysical Research: Solid Earth* **115**(B5).

Quigley, M., Van Dissen, R., Litchfield, N., Villamor, P., Duffy, B., Barrell, D., Furlong, K., Stahl, T., Bilderback, E. & Noble, D. (2012), 'Surface rupture during the 2010 Mw 7.1 Darfield (Canterbury) earthquake: Implications for fault rupture dynamics and seismic-hazard analysis', *Geology* **40**(1), 55–58.

Quinay, P. E. B., Ichimura, T. & Hori, M. (2012), 'Waveform inversion for modeling three-dimensional crust structure with topographic effects', *Bulletin of the Seismological Society of America* **102**(3), 1018–1029.

Regenauer-Lieb, K. & Yuen, D. (2003), 'Modeling shear zones in geological and planetary sciences: solid-and fluid-thermal–mechanical approaches', *Earth-Science Reviews* **63**(3-4), 295–349.

Renard, F., Voisin, C., Marsan, D. & Schmittbuhl, J. (2006), 'High resolution three dimensional laser scanner measurements of a strike-slip fault quantify its morphological anisotropy at all scales', *Geophysical Research Letters* **33**(4).

Restrepo, D. & Bielak, J. (2014), 'Virtual topography: A fictitious domain approach for analyzing free-surface irregularities in large-scale earthquake ground motion simulation', *International Journal for Numerical Methods in Engineering* **100**(7), 504–533.

Restrepo, D., Bielak, J., Serrano, R., Gómez, J. & Jaramillo, J. (2016), 'Effects of realistic topography on the ground motion of the Colombian Andes–A case study at the Aburrá Valley, Antioquia', *Geophysical Journal International* **204**(3), 1801–1816.

Rice, J. R. (1993), 'Spatio-temporal complexity of slip on a fault', *Journal of Geophysical Research: Solid Earth* **98**(B6), 9885–9907.

Rice, J. R. (2006), 'Heating and weakening of faults during earthquake slip', *Journal of Geophysical Research: Solid Earth* **111**(B5).

Rice, J. R., Sammis, C. G. & Parsons, R. (2005), 'Off-fault secondary failure induced by a dynamic slip pulse', *Bulletin of the Seismological Society of America* **95**(1), 109–134.

Roten, D., Olsen, K. & Day, S. (2017), 'Off-fault deformations and shallow slip deficit from dynamic rupture simulations with fault zone plasticity', *Geophysical Research Letters* **44**(15), 7733–7742.

Rubin, A. M. & Ampuero, J.-P. (2007), 'Aftershock asymmetry on a bimaterial interface', *Journal of Geophysical Research: Solid Earth* **112**(B5).

Rubin, A. M. & Gillard, D. (2000), 'Aftershock asymmetry/rupture directivity among Central San Andreas fault microearthquakes', *Journal of Geophysical Research: Solid Earth* **105**(B8), 19095–19109.

Rudnicki, J. W. & Rice, J. (1975), 'Conditions for the localization of deformation in pressure-sensitive dilatant materials', *Journal of the Mechanics and Physics of Solids* **23**(6), 371–394.

Ruina, A. (1983), 'Slip instability and state variable friction laws', *Journal of Geophysical Research: Solid Earth* **88**(B12), 10359–10370.

Russ, J. C. (1994), *Fractal Surfaces.*, Plenum, New York.

Sagy, A., Brodsky, E. E. & Axen, G. J. (2007), 'Evolution of fault-surface roughness with slip', *Geology* **35**(3), 283–286.

Salichon, J., Lundgren, P., Delouis, B. & Giardini, D. (2004), 'Slip history of the 16 October 1999 Mw 7.1 Hector Mine earthquake (California) from the inversion of InSAR, GPS, and teleseismic data', *Bulletin of the Seismological Society of America* **94**(6), 2015–2027.

Sánchez-Sesma, F. J. (1985), 'Diffraction of elastic SH waves by wedges', *Bulletin of the seismological society of America* **75**(5), 1435–1446.

Schmedes, J., Archuleta, R. J. & Lavallée, D. (2010), 'Correlation of earthquake source parameters inferred from dynamic rupture simulations', *Journal of Geophysical Research: Solid Earth* **115**(B3).

Schmitt, S. V., Segall, P. & Dunham, E. M. (2015), 'Nucleation and dynamic rupture on

weakly stressed faults sustained by thermal pressurization', *Journal of Geophysical Research: Solid Earth* **120**(11), 7606–7640.

Scholz, C. H. (1982), 'Scaling laws for large earthquakes: consequences for physical models', *Bulletin of the Seismological Society of America* **72**(1), 1–14.

Scholz, C. H. (2002), *The mechanics of earthquakes and faulting*, Cambridge University Press.

Schultz, A. & Bartholomew, M. (2009), 'Geologic map of the Staffordsville Quadrangle, Virginia', *Virginia Department of Mines, Minerals, and Energy, Division of Geology and Mineral Resources, Open-File Report 09-02, scale 1* .

Schultz, A. P. (1988), *Horses in fensters of the Pulaski thrust sheet, southwestern Virginia: structure, kinematics, and implications for hydrocarbon potential of the Eastern Overthrust Belt*, US Government Printing Office.

Segou, M. & Parsons, T. (2014), 'The stress shadow problem in physics-based aftershock forecasting: Does incorporation of secondary stress changes help?', *Geophysical Research Letters* **41**(11), 3810–3817.

Şengör, A., Tüysüz, O., Imren, C., Sakınç, M., Eyidoğan, H., Görür, N., Le Pichon, X. & Rangin, C. (2005), 'The North Anatolian fault: A new look', *Annu. Rev. Earth Planet. Sci.* **33**, 37–112.

Shaw, B. E., Richards-Dinger, K. & Dieterich, J. H. (2015), 'Deterministic model of earthquake clustering shows reduced stress drops for nearby aftershocks', *Geophysical Research Letters* **42**(21), 9231–9238.

Shearer, P., Hauksson, E. & Lin, G. (2005), 'Southern California hypocenter relocation with waveform cross-correlation, part 2: Results using source-specific station terms and cluster analysis', *Bulletin of the Seismological Society of America* **95**(3), 904–915.

Shi, Z. & Ben-Zion, Y. (2006), 'Dynamic rupture on a bimaterial interface governed by slip-weakening friction', *Geophysical Journal International* **165**(2), 469–484.

Shi, Z. & Day, S. M. (2013), 'Rupture dynamics and ground motion from three dimensional rough-fault simulations', *Journal of Geophysical Research: Solid Earth* **118**(3), 1122–1141.

Simon, R. I. & Gray, D. R. (1982), 'Interrelations of mesoscopic structures and strain across a small regional fold, virginia appalachians', *Journal of Structural Geology* **4**(3), 271–289.

Simons, M., Fialko, Y. & Rivera, L. (2002), 'Coseismic deformation from the 1999 Mw 7.1 Hector Mine, California, earthquake as inferred from InSAR and GPS observations', *Bulletin of the Seismological Society of America* **92**(4), 1390–1402.

Siro, L. (1982), Southern Italy November 23, 1980 earthquake, *in* 'Proceedings of the seventh European conference on earthquake engineering, Athens, Greece', pp. 20–25.

Skempton, A. (1954), 'The pore-pressure coefficients a and b', *Geotechnique* **4**(4), 143–147.

Smith, D. E. & Dieterich, J. H. (2010), Aftershock sequences modeled with 3-D stress heterogeneity and rate-state seismicity equations: Implications for crustal stress estimation, *in* 'Seismogenesis and Earthquake Forecasting: The Frank Evison Volume II', Springer, pp. 213–231.

Smith, D. E. & Heaton, T. H. (2011), 'Models of stochastic, spatially varying stress in the crust compatible with focal-mechanism data, and how stress inversions can be biased toward the stress rate', *Bulletin of the Seismological Society of America* **101**(3), 1396–1421.

Spraggins, S. A. (1999), Deformation history of a foreland thrust belt in a recess: an example from the Roanoke recess, Appalachians, USA, PhD thesis, University of Tennessee, Knoxville.

Spudich, P., Hellweg, M. & Lee, W. (1996), 'Directional topographic site response at Tarzana observed in aftershocks of the 1994 Northridge, California, earthquake: implications for mainshock motions', *Bulletin of the Seismological Society of America* **86**(1B), S193–S208.

Spudich, P. & Olsen, K. (2001), 'Fault zone amplified waves as a possible seismic hazard along the Calaveras fault in central California', *Geophysical Research Letters* **28**(13), 2533–2536.

Steacy, S., Gomberg, J. & Cocco, M. (2005), 'Introduction to special section: Stress transfer, earthquake triggering, and time-dependent seismic hazard', *Journal of Geophysical Research: Solid Earth* **110**(B5).

Steacy, S., Marsan, D., Nalbant, S. S. & McCloskey, J. (2004), 'Sensitivity of static stress calculations to the earthquake slip distribution', *Journal of Geophysical Research: Solid Earth* **109**(B4).

Stein, R. S. (1999), 'The role of stress transfer in earthquake occurrence', *Nature* **402**(6762), 605.

Stein, R. S. (2003), 'Earthquake conversations', *Scientific American* **288**(1), 72–79.

Stein, R. S., King, G. C. & Lin, J. (1994), 'Stress triggering of the 1994 M= 6.7 Northridge, California, earthquake by its predecessors', *Science* **265**(5177), 1432–1435.

Stupazzini, M., Paolucci, R. & Igel, H. (2009), 'Near-fault earthquake ground-motion simulation in the Grenoble valley by a high-performance spectral element code', *Bulletin of the Seismological Society of America* **99**(1), 286–301.

Suzuki, T. & Yamashita, T. (2006), 'Nonlinear thermoporoelastic effects on dynamic earthquake rupture', *Journal of Geophysical Research: Solid Earth* **111**(B3).

Taborda, R., Azizzadeh-Roodpish, S., Khoshnevis, N. & Cheng, K. (2016), 'Evaluation of the Southern California seismic velocity models through simulation of recorded events', *Geophysical Journal International* **205**(3), 1342–1364.

Taborda, R., López, J., Karaoglu, H., Urbanic, J. & Bielak, J. (2010), 'Speeding up finite element wave propagation for large-scale earthquake simulations'.

Taborda, R. & Roten, D. (2015), 'Physics-based ground-motion simulation', *Encyclopedia of Earthquake Engineering, Springer, Berlin, Heidelberg* pp. 1–33.

Templeton, E. L. & Rice, J. R. (2008), 'Off-fault plasticity and earthquake rupture dynamics: 1. dry materials or neglect of fluid pressure changes', *Journal of Geophysical Research: Solid Earth* **113**(B9).

Tenthorey, E., Cox, S. F. & Todd, H. F. (2003), 'Evolution of strength recovery and permeability during fluid–rock reaction in experimental fault zones', *Earth and Planetary Science Letters* **206**(1-2), 161–172.

Thatcher, W. & Hanks, T. C. (1973), 'Source parameters of Southern California earthquakes', *Journal of Geophysical Research* **78**(35), 8547–8576.

Tinti, E., Bizzarri, A. & Cocco, M. (2005), 'Modeling the dynamic rupture propagation on heterogeneous faults with rate-and state-dependent friction', *Annals of Geophysics* **48**(2).

Tinti, E., Fukuyama, E., Piatanesi, A. & Cocco, M. (2005), 'A kinematic source-time function compatible with earthquake dynamics', *Bulletin of the Seismological Society of America* **95**(4), 1211–1223.

Toda, S., Lin, J., Meghraoui, M. & Stein, R. S. (2008), '12 May 2008 M= 7.9 Wenchuan, China, earthquake calculated to increase failure stress and seismicity rate on three major fault systems', *Geophysical Research Letters* **35**(17).

Toda, S., Stein, R. S., Beroza, G. C. & Marsan, D. (2012), 'Aftershocks halted by static stress shadows', *Nature Geoscience* **5**(6), 410.

Toda, S., Stein, R. S., Reasenberg, P. A., Dieterich, J. H. & Yoshida, A. (1998), 'Stress transferred by the 1995 Mw = 6.9 Kobe, Japan, shock: Effect on aftershocks and future earthquake probabilities', *Journal of Geophysical Research: Solid Earth* **103**(B10), 24543–24565.

Toda, S., Stein, R. S., Richards-Dinger, K. & Bozkurt, S. B. (2005), 'Forecasting the evolution of seismicity in Southern California: Animations built on earthquake stress transfer', *Journal of Geophysical Research: Solid Earth* **110**(B5).

Tsaur, D.-H. (2011), 'Scattering and focusing of SH waves by a lower semielliptic convex topography', *Bulletin of the Seismological Society of America* **101**(5), 2212–2219.

Tsaur, D.-H. & Chang, K.-H. (2009), 'Scattering and focusing of sh waves by a convex circular-arc topography', *Geophysical Journal International* **177**(1), 222–234.

Tse, S. T. & Rice, J. R. (1986), 'Crustal earthquake instability in relation to the depth variation of frictional slip properties', *Journal of Geophysical Research: Solid Earth* **91**(B9), 9452–9472.

Tsutsumi, A. & Shimamoto, T. (1997), 'High-velocity frictional properties of gabbro', *Geophysical Research Letters* **24**(6), 699–702.

Tu, T., Yu, H., Ramirez-Guzman, L., Bielak, J., Ghattas, O., Ma, K.-L. & O'hallaron, D. R. (2006), From mesh generation to scientific visualization: An end-to-end approach to parallel supercomputing, *in* 'Proceedings of the 2006 ACM/IEEE conference on Supercomputing', ACM, p. 91.

Ulrich, T., Gabriel, A.-A., Ampuero, J.-P. & Xu, W. (2019), 'Dynamic viability of the 2016

Mw 7.8 Kaikōura earthquake cascade on weak crustal faults', *Nature communications* **10**(1), 1213.

Vidale, J. E., Boyle, K. L. & Shearer, P. M. (2006), 'Crustal earthquake bursts in California and Japan: Their patterns and relation to volcanoes', *Geophysical research letters* **33**(20).

Vidale, J. E. & Shearer, P. M. (2006), 'A survey of 71 earthquake bursts across Southern California: Exploring the role of pore fluid pressure fluctuations and aseismic slip as drivers', *Journal of Geophysical Research: Solid Earth* **111**(B5).

Viesca, R. C., Templeton, E. L. & Rice, J. R. (2008), 'Off-fault plasticity and earthquake rupture dynamics: 2. effects of fluid saturation', *Journal of Geophysical Research: Solid Earth* **113**(B9).

Waite, G. P. & Smith, R. B. (2002), 'Seismic evidence for fluid migration accompanying subsidence of the Yellowstone caldera', *Journal of Geophysical Research: Solid Earth* **107**(B9).

Wald, D. J. & Heaton, T. H. (1994), 'Spatial and temporal distribution of slip for the 1992 Landers, California, earthquake', *Bulletin of the Seismological Society of America* **84**(3), 668–691.

Wald, D. J., Helmberger, D. V. & Heaton, T. H. (1991), 'Rupture model of the 1989 Loma Prieta earthquake from the inversion of strong-motion and broadband teleseismic data', *Bulletin of the Seismological Society of America* **81**(5), 1540–1572.

Waldhauser, F. & Schaff, D. P. (2008), 'Large-scale relocation of two decades of Northern California seismicity using cross-correlation and double-difference methods', *Journal of Geophysical Research: Solid Earth* **113**(B8).

Wells, D. L. & Coppersmith, K. J. (1994), 'New empirical relationships among magnitude,

rupture length, rupture width, rupture area, and surface displacement', *Bulletin of the seismological Society of America* **84**(4), 974–1002.

Wesnousky, S. G. (2008), 'Displacement and geometrical characteristics of earthquake surface ruptures: Issues and implications for seismic-hazard analysis and the process of earthquake rupture', *Bulletin of the Seismological Society of America* **98**(4), 1609–1632.

Whitaker, A. E. & Bartholomew, M. J. (1999), 'Layer parallel shortening; a mechanism for determining deformation timing at the junction of the Central and Southern Appalachians', *American Journal of Science* **299**(3), 238–254.

Wiemer, S. (2000), 'Introducing probabilistic aftershock hazard mapping', *Geophysical Research Letters* **27**(20), 3405–3408.

Zeng, Y. & Anderson, J. (2000), 'Evaluation of numerical procedures for simulating near-fault long-period ground motions using Zeng method, report 2000/01 to the PEER utilities program'.

Zhang, C., Oglesby, D. D. & Xu, G. (2004), 'Earthquake nucleation on dip-slip faults', *Journal of Geophysical Research: Solid Earth* **109**(B11).

Zhang, C., Oglesby, D. D. & Xu, G. (2006), 'Earthquake nucleation on dip-slip faults with depth-dependent frictional properties', *Journal of Geophysical Research: Solid Earth* **111**(B7).